



AFRL-OSR-VA-TR-2015-0025

**AIR FORCE CENTER OF EXCELLENCE ON BIO-NANO-ENABLED INORGANIC/ORGANIC
NANOSTRUCTU**

**Kenneth Sandhage
GEORGIA TECH RESEARCH CORPORATION**

**01/09/2015
Final Report**

DISTRIBUTION A: Distribution approved for public release.

**Air Force Research Laboratory
AF Office Of Scientific Research (AFOSR)/ RTD
Arlington, Virginia 22203
Air Force Materiel Command**

REPORT DOCUMENTATION PAGE				<i>Form Approved</i> OMB No. 0704-0188	
Public reporting burden for this collection of information is estimated to average 1 hour per response, including the time for reviewing instructions, searching existing data sources, gathering and maintaining the data needed, and completing and reviewing this collection of information. Send comments regarding this burden estimate or any other aspect of this collection of information, including suggestions for reducing this burden to Department of Defense, Washington Headquarters Services, Directorate for Information Operations and Reports (0704-0188), 1215 Jefferson Davis Highway, Suite 1204, Arlington, VA 22202-4302. Respondents should be aware that notwithstanding any other provision of law, no person shall be subject to any penalty for failing to comply with a collection of information if it does not display a currently valid OMB control number. PLEASE DO NOT RETURN YOUR FORM TO THE ABOVE ADDRESS.					
1. REPORT DATE (DD-MM-YYYY)		2. REPORT TYPE		3. DATES COVERED (From - To)	
4. TITLE AND SUBTITLE				5a. CONTRACT NUMBER	
				5b. GRANT NUMBER	
				5c. PROGRAM ELEMENT NUMBER	
6. AUTHOR(S)				5d. PROJECT NUMBER	
				5e. TASK NUMBER	
				5f. WORK UNIT NUMBER	
7. PERFORMING ORGANIZATION NAME(S) AND ADDRESS(ES)				8. PERFORMING ORGANIZATION REPORT NUMBER	
9. SPONSORING / MONITORING AGENCY NAME(S) AND ADDRESS(ES)				10. SPONSOR/MONITOR'S ACRONYM(S)	
				11. SPONSOR/MONITOR'S REPORT NUMBER(S)	
12. DISTRIBUTION / AVAILABILITY STATEMENT					
13. SUPPLEMENTARY NOTES					
14. ABSTRACT					
15. SUBJECT TERMS					
16. SECURITY CLASSIFICATION OF:			17. LIMITATION OF ABSTRACT	18. NUMBER OF PAGES	19a. NAME OF RESPONSIBLE PERSON
a. REPORT	b. ABSTRACT	c. THIS PAGE			19b. TELEPHONE NUMBER (include area code)

**Bio-nano-enabled Inorganic/Organic Nanocomposites and Improved Cognition
(BIONIC) Air Force Center of Excellence**

Project Reports for Interdisciplinary Research Groups #1, #2, and #3
(March 2009 to September 2014)

Kenneth H. Sandhage^{1,2}, Vladimir V. Tsukruk¹

¹School of Materials Science and Engineering

²School of Chemistry and Biochemistry

Georgia Institute of Technology

Atlanta, GA 30332

Summary of BIONIC Participants and Publications

Participating Faculty, Primary Appointment:

Total Supported Faculty Participants: 17

Georgia Institute of Technology:

- Oliver Brand, School of Electrical & Computer Engineering (Seed Grant, IRG #3)
- Mostafa A. El-Sayed, School of Chemistry & Biochemistry (IRG #2)
- Andrei Fedorov, School of Mechanical Engineering (IRG #2)
- Michael A. Filler, School of Chemical & Biomolecular Engineering (Seed Grant, IRG #1)
- Shella Keilholz, School of Biomedical Engineering (IRG #3)
- Bernard Kippelen, School of Electrical & Computer Engineering (IRG #1)
- Nils Kröger, School of Chemistry & Biochemistry (now at TU Dresden) (IRG #1)
- Michelle LaPlaca, School of Biomedical Engineering (IRG #3)
- Zhiqun Lin, School of Materials Science & Engineering (Seed Grant IRG #2)
- Seth R. Marder, School of Chemistry & Biochemistry (IRG #1)
- Valeria T. Milam, School of Materials Science & Engineering (Seed Grant, IRG #1)
- Joseph W. Perry, School of Chemistry & Biochemistry (Seed Grant, IRG #1)
- Kenneth H. Sandhage, School of Materials Science & Engineering (IRG #1)
- Eric H. Schumacher, School of Psychology (IRG #3)
- Vladimir V. Tsukruk, School of Materials Science & Engineering (IRG #2)

Emory University:

- Charles Epstein, Department of Neurology (Seed Grant, IRG #3)

The Ohio State University:

- Hamish Fraser, Department of Materials Science & Engineering (IRGs #1, #2)

Participating AFRL Researchers (partial list):

A = Thesis Advisor and/or Adjunct Professor

E = Executive Oversight Committee

R = Research Management Team

- Dr. Giorgio Bazzan (Materials and Manufacturing Directorate)
- Dr. Sushmita A. Biswas (Materials and Manufacturing Directorate)
- Dr. Timothy J. Bunning^{A,R} (Materials and Manufacturing Directorate,)
- Dr. Lynn Caldwell (Human Effectiveness Directorate)
- Dr. James Christensen (Human Effectiveness Directorate)
- Dr. Michael Clark (Materials and Manufacturing Directorate)
- James R. Deneault (Materials and Manufacturing Directorate)
- Dr. Patrick B. Dennis (Materials and Manufacturing Directorate)
- Dr. Matthew B. Dickerson (Materials and Manufacturing Directorate)
- Dr. Lawrence Drummy (Materials and Manufacturing Directorate)
- Dr. Michael F. Durstock^A (Materials and Manufacturing Directorate)
- Dr. Matthew Eby (Materials and Manufacturing Directorate)
- Dr. Barry Farmer^E (Materials and Manufacturing Directorate)

- Dr. Wendy Goodson (Materials and Manufacturing Directorate)
- Dr. Jacob Haag (Materials and Manufacturing Directorate)
- Dr. Josh Hagen (Human Effectiveness Directorate)
- Dr. Svetlana Harbaugh (Human Effectiveness Directorate)
- Dr. Chad Hunter (Materials and Manufacturing Directorate)
- Dr. Rachel Jakubiak (Materials and Manufacturing Directorate)
- Dr. Glenn Johnson^A (Materials and Manufacturing Directorate)
- Dr. Tae-Sik Kang (Materials and Manufacturing Directorate)
- Dr. Nancy Kelly-Loughnane^A (Human Effectiveness Directorate)
- Dr. Sang Kim (Materials and Manufacturing Directorate)
- Dr. Ryan Kramer (Human Effectiveness Directorate)
- Dr. Benjamin Leever (Materials and Manufacturing Directorate)
- Dr. Heather Luckarift (Materials and Manufacturing Directorate)
- Dr. Michael McConney (Materials and Manufacturing Directorate)
- Dr. R. Andrew McKinley^R (Human Effectiveness Directorate)
- Dr. Peter Mirau (Materials and Manufacturing Directorate)
- Dr. Rajesh R. Naik^{A,R} (Materials and Manufacturing Directorate)
- Dr. Dhriti Nepal (Materials and Manufacturing Directorate)
- Dr. Ruth Pachter (Materials and Manufacturing Directorate)
- Dr. Gyanaranjan Pattanaik (Materials and Manufacturing Directorate)
- Dr. Shawn Putnam (Materials and Manufacturing Directorate)
- Dr. Regina Schmidt (Human Effectiveness Directorate)
- Dr. Regina Shia^R (Human Effectiveness Directorate)
- Dr. Suzanne Smith (Human Effectiveness Directorate)
- Dr. Morley O. Stone^E (Human Effectiveness Directorate)
- Dr. Guin Strack (Materials and Manufacturing Directorate)
- Dr. Christopher Tabor (Materials and Manufacturing Directorate)
- Dr. Lloyd Tripp^R (Human Effectiveness Directorate)
- Dr. Augustine Urbas (Materials and Manufacturing Directorate)
- Dr. Richard Vaia (Materials and Manufacturing Directorate)
- Dr. Andrey Voevodin (Materials and Manufacturing Directorate)
- Dr. Timothy White (Materials and Manufacturing Directorate)

Supported Students (partially- or fully-supported):

Ph.D. Students Fully- or Partially-Supported: **50**

M.S. Students Fully- or Partially-Supported: **7**

Undergraduate Students: **2**

*One or more internship experiences (at Wright-Patterson or Tyndall AFB)

- *Kyle Anderson (Ph.D. student, School of Materials Science & Engineering, U.S. Citizen)
- *David Anderson (Ph.D. student, School of Mechanical Engineering, U.S. Citizen)
- Luke A. Beardslee (Ph.D. student, School of Electrical & Computer Engineering, U.S. Citizen)

- *J. Dan Berrigan (Ph.D. student, School of Materials Science & Engineering, U.S. Citizen); ***now working in the Durstock group at WPAFB***
- Jacob Billings (Ph.D. student, School of Neuroscience, U.S. Citizen)
- Michael Bonifacio (undergraduate student, School of Biomedical Engineering, U.S. Citizen)
- Justin Bordley (Ph.D. student, School of Chemistry & Biochemistry, U.S. Citizen)
- Christopher Carron (Ph.D. student, School of Electrical & Computer Engineering, U.S. Citizen)
- *Jessica Carter (M.S. Student, School of Materials Science & Engineering, U.S. Citizen)
- Zac Combs (NDSEG Fellow, Ph.D. student, School of Materials Science & Engineering, U.S. Citizen)
- Savannah Cookson (Ph.D. Student, School of Psychology, U.S. Citizen)
- *Ben deGlee (Ph.D. student, School of Materials Science & Engineering, U.S. Citizen)
- *Irina Drachuk (Ph.D. student, School of Materials Science & Engineering, U.S. Citizen), ***now working in the Kelley-Loughnane group at WPAFB***
- Alfred Ernst, III (Ph.D. student, School of Electrical & Computer Engineering, U.S. Citizen)
- *Ren Geryak (Ph.D. student, School of Materials Science & Engineering, U.S. Citizen)
- Patrick Getz (Ph.D. student, School of Electrical & Computer Engineering, U.S. Citizen)
- David Giles (Ph.D. student, School of Electrical & Computer Engineering, U.S. Citizen)
- Christine Godwin (Ph.D. student, School of Psychology, U.S. Citizen)
- Anise Grant (Ph.D. student, School of Materials Science & Engineering, U.S. Citizen),
- Josh Grooms (Ph.D. student, School of Biomedical Engineering, U.S. Citizen)
- *Maneesh Gupta (Ph.D. student, School of Materials Science & Engineering, U.S. Citizen)
- *Nicholas Haase (Ph.D. student, School of Chemistry & Biochemistry, U.S. Citizen)
- James Hsu (Ph.D. student, School of Electrical & Computer Engineering, Permanent Resident)
- James Iocozzia (Ph.D Student, Material Science & Engineering, U.S. Citizen)
- Fadi Jradi (Ph.D. student, School of Chemistry and Biochemistry, Lebanese National)
- Songkil Kim (PhD student, School of Mechanical Engineering)
- Philip Kwon (Ph.D. student, School of Mechanical Engineering, U.S. Citizen)
- Erin Lightman (Ph.D. student, School of Psychology, U.S. Citizen)
- Drew Loney (Ph.D. student, School of Mechanical Engineering, U.S. Citizen)
- *Matthew Magnuson (Ph.D. student, Biomedical Engineering, U.S. Citizen)
- Sidney Malak (Ph.D. student, School of Materials Science & Engineering, U.S. Citizen)
- *Kamil Marczewski (M.S. Student, School of Materials Science & Engineering, U.S. Citizen)
- *Mike McConney (Ph.D. student, School of Materials Science & Engineering, U.S. Citizen); ***now working as a staff researcher at WPAFB***

- *Taylor McLachlan (Ph.D. student, School of Materials Science & Engineering, U.S. Citizen)
- *Mac Merritt (Undergraduate, School of Biomedical Engineering, U.S. Citizen)
- Rebecca Mitchell (née Hill) (Ph.D. student, School of Chemistry and Biochemistry, U.S. Citizen)
- Ildar R. Musin (Ph.D. student, School of Chemical & Biomolecular Engineering, U.S. Citizen)
- *Rachel Near (Ph.D. student, School of Chemistry & Biochemistry, U.S. Citizen)
- Jessie Nock (M.S. student, School of Chemistry & Biochemistry, U.S. Citizen)
- Daniel Olivero ((Ph.D. student, Mechanical Engineering, U.S. Citizen)
- *Spyridon Pavlidis (Ph.D. student, School of Electrical & Computer Engineering, U.S. Citizen)
- Adam Poncheri (M.S. student, School of Chemistry & Biochemistry, U.S. Citizen),
- William J. Potscavage, Jr. (Ph.D. student, School of Electrical and Computer Engineering, U.S. Citizen)
- *Brian Roberts (Ph.D. student, School of Psychology, U.S. Citizen)
- *Marcel Said (Ph.D. student, School of Chemistry and Biochemistry, U.S. Citizen)
- Hillary Schwarb (Ph.D. student, School of Psychology, U.S. citizen)
- James Silva (Ph.D. student, School of Mechanical Engineering, U.S. Citizen)
- Saujan V. Sivaram (Ph.D. student, School of Chemical & Biomolecular Engineering, U.S. Citizen)
- Derek Smith (Ph.D. student, School of Psychology, U.S. Citizen),
- Jin-Jyh Su (Ph.D. student, School of Electrical & Computer Engineering, U.S. Citizen)
- *Rick Sullivan (Ph.D. student, School of Materials Science & Engineering, U.S. Citizen)
- Chris E. Tabor (Ph.D., School of Chemistry & Biochemistry, U.S. Citizen), ***now working as a staff researcher at WPAFB***
- *Maeling Tapp (Ph.D., School of Materials Science & Engineering, U.S. Citizen)
- Garth Thompson (Ph.D. student, Biomedical Engineering, U.S. Citizen)
- Helen Westbrook (M.S. student, School of Chemistry & Biochemistry, U.S. Citizen)
- Brock Wester (Ph.D. student, School of Biomedical Engineering, U.S. Citizen)
- Martha Willis (M.S. student, Bioengineering, U.S. Citizen)
- Jeannie Yom (M.S. student, School of Chemistry & Biochemistry, U.S. Citizen)
- Seth Young (Ph.D. student, School of Materials Science & Engineering, U.S. Citizen)

Publications:

Total Publications Accepted or In Print: **85**

- Y. Fang, Q. Wu, M. B. Dickerson, Y. Cai, S. Shian, J. D. Berrigan, N. Poulsen, N. Kröger, K. H. Sandhage, "Protein-Mediated Layer-by-Layer Syntheses of Free-standing Microscale Titania Structures with Biologically-assembled 3-D Morphologies," *Chem. Mater.*, **21** [24] 5704-5710 (2009).
- E. Kharlampieva, V. Kozlovskaya, J. Chan, J. F. Ankner, V. V. Tsukruk, "Spin-Assisted Layer-by-Layer Assembly: Variation of Stratification as Studied with Neutron Reflectivity," *Langmuir*, **25**, 14017-14024 (2009).

- M. E. McConney, K. D. Anderson, L. L. Brott, R. R. Naik, V. V. Tsukruk, "Bioinspired Material Approaches to Sensing," *Adv. Funct. Mater.*, **19**, 2527-2544 (2009).
- S. Shian, K. H. Sandhage, "A Gas-Tight, Cu K α X-ray Transparent Reaction Chamber for High Temperature X-ray Diffraction Analyses of Halide Gas/Solid Reactions," *Rev. Sci. Instr.*, **80**, 115108/1-115108/7 (2009).
- K. D. Anderson, M. Luo, R. Jakubiak, R. R. Naik, T. J. Bunning, V. V. Tsukruk, "Robust Plasma Polymerized-Titania/Silica Janus Microparticles," *Chem Mater.*, **22**, 3259-3264 (2010).
- K. D. Anderson, K. Marczewski, S. Singamaneni, J. M. Slocik, R. Jakubiak, R. R. Naik, T. J. Bunning, V. V. Tsukruk, "Plasma Amino Acid Coatings for a Conformal Growth of Titania Nanoparticles," *ACS Appl. Mater. Interfaces*, **2**, 2269-2281 (2010).
- H. Cheun, C. Fuentes-Hernandez, Y. Zhou, W. J. Potscavage, S.-J. Kim, J. Shim, A. Dindar, B. Kippelen, "Electrical and Optical Properties of ZnO Processed by Atomic Layer Deposition in Inverted Polymer Solar Cells," *J. Phys. Chem.*, **114**, 20713-20718 (2010).
- H. Cheun, J. B. Kim, Y. H. Zhou, Y. Fang, A. Dindar, C. Fuentes-Hernandez, J. Shim, K. H. Sandhage, B. Kippelen, "Inverted Polymer Solar Cells with Amorphous Indium Zinc Oxide as Electron Collecting Electrode," *Optics Express*, **18**, A506-A512 (2010).
- M. K. Gupta, S. Singamaneni, M. McConney, L. F. Drummy, R. R. Naik, V. V. Tsukruk, "A Facile Fabrication Strategy for Patterning Protein Chain Conformation in Silk Materials," *Adv. Mater.*, **22**, 115-119 (2010).
- E. Kharlampieva, C. M. Jung, V. Kozlovskaya, V. V. Tsukruk, "Secondary Structure of silaffin at interfaces and titania formation," *J. Mater. Chem.*, **20**, 5242-5250 (2010).
- E. Kharlampieva, V. Kozlovskaya, R. Gunawidjaja, V. V. Shevchenko, R. Vaia, R. R. Naik, D. L. Kaplan, V. V. Tsukruk, "Flexible Silk-Inorganic Nanocomposites With Transparent to Mirror-like Optical Properties," *Adv. Funct. Mater.*, **20**, 840-846 (2010).
- E. Kharlampieva, V. Kozlovskaya, O. Zavgorodnya, G. D. Lilly, N. A. Kotov, V. V. Tsukruk, "pH-Responsive Photoluminescent LbL Hydrogels with Confined Quantum Dots," *Soft Matter*, **6**, 800-807 (2010).
- E. Kharlampieva, V. Kozlovskaya, B. Wallet, V. V. Shevchenko, R. R. Naik, R. Vaia, D. L. Kaplan, V. V. Tsukruk, "Co-crosslinking silk matrices with silica nanostructures for robust ultrathin nanocomposites," *ACS Nano*, **4**, 7053-7063 (2010).
- M. E. McConney, S. Singamaneni, V. V. Tsukruk, "Probing Soft Matter with the Atomic Force Microscope: Force-spectroscopy and Beyond," *Polym. Rev.*, **50**, 235-286 (2010).
- K. H. Sandhage, "Materials 'Alchemy': Shape-preserving Chemical Transformation of Micro-to-Macroscopic 3-D Structures," *JOM*, **62** [6] 32-43 (2010).
- S. Shian, K. H. Sandhage, "Hexagonal and Cubic TiOF₂," *J. Appl. Crystall.*, **43** [4] 757-761 (2010).
- Stuart, M. C.; Huck, W.; Genzer, J.; Müller, M.; Ober, C.; Stamm, M.; Sukhorukov, G.; Szleifer, I.; Tsukruk, V. V.; Urban, M.; Winnik, F.; Zauscher, S.; Luzinov, I.; Minko, S. "Emerging Applications of Stimuli-responsive Polymer Materials." *Nat. Mater.*, **9**, 101-113 (2010).
- Y. Zhou, H. Cheun, S. Choi, W.J. Potscavage Jr., C. Fuentes-Hernandez, B. Kippelen, "Indium Tin Oxide-free and Metal-free Semitransparent Organic Solar Cells," *Appl. Phy. Lett.*, **97**, 153304/1-153304/3 (2010).

- Y. Zhou, H. Cheun, W. J. Potscavage Jr., C. Fuentes-Hernandez, S.-J. Kim, B. Kippelen, "Inverted Organic Solar Cells with ITO Electrodes Modified with an Ultrathin Al_2O_3 Buffer Layer Deposited by Atomic Layer Deposition," *J. Mater. Chem.*, **20**, 6189-6194 (2010).
- Z. Bao, M.-K. Song, S. Davis, Y. Cai, M. Liu, K. H. Sandhage, "Bio-enabled Syntheses of High Surface Area, Micro/mesoporous C Particles with Selectable 3-D Biogenic Morphologies for Tailored Catalysis, Filtration, or Adsorption," *Energy & Environ. Sci.*, **4** [10] 3980-3984 (2011).
- J. D. Berrigan, T. S. Kang, Y. Cai, J. R. Deneault, M. F. Durstock, K. H. Sandhage, "Protein-Enabled Layer-by-Layer Syntheses of Aligned, Porous-Wall, High-Aspect-Ratio TiO_2 Nanotube Arrays," *Adv. Funct. Mater.* **21**, 1693-1700 (2011).
- J. L. Carter, I. Drachuk, S. Harbaugh, N. Kelley-Loughnane, M. Stone, V. V. Tsukruk, "Truly Non-Ionic Polymer Shells for Encapsulation of Living Cells," *Macromol. Bioscience*, **11**, 1244-1253 (2011).
- H. Cheun, J. D. Berrigan, Y. Zhou, M. Fenoll, J. Shim, C. Fuentes-Hernandez, K. H. Sandhage, B. Kippelen, "Roles of Thermally-Induced Vertical Phase Segregation and Crystallization on the Photovoltaic Performance of Bulk Heterojunction Inverted Polymer Solar Cells," *Energy Environ. Sci.*, **4**, 3456-3460 (2011).
- Z. A. Combs, S. Chang, T. Clark, S. Singamaneni, K. D. Anderson, V. V. Tsukruk, "Label-free Raman mapping of surface distribution of protein A and IgG biomolecules," *Langmuir*, **27**, 3198-3205 (2011).
- M. K. Gupta, S. Chang, S. Singamaneni, L. F. Drummy, R. Gunawidjaja, R. R. Naik, V. V. Tsukruk, "pH Triggered SERS via Modulated Plasmonic Coupling in Individual Bimetallic Nanocobs," *Small*, **7**, 1192-1198 (2011).
- N. R. Haase, S. Shian, K. H. Sandhage, N. Kröger, "Biocatalytic Nanoscale Coatings Through Biomimetic Layer-by-layer Mineralization," *Adv. Funct. Mater.*, **21** (22) 4243-4251 (2011).
- C. Huang, S. Barlow, S. R. Marder, "Perylene-3,4,9,10-tetracarboxylic Acid Diimides: Synthesis, Physical Properties, and Use in Organic Electronics," *J. Org. Chem.*, **76**, 2386-2407 (2011).
- Kodiyath, R., Wang, J.; Combs, Z. A.; Chang, S.; Gupta, M. K.; Anderson, K. D.; Brown, R. J. C.; Tsukruk, V. V., "SERS Effects in Silver-decorated Cylindrical Nanopores," *Small*, **7**, 3452-3457 (2011).
- V. Kozlovskaya, S. Harbaugh, I. Drachuk, O. Shchepelina, N. Kelley-Loughnane, M. Stone, V. V. Tsukruk, "Hydrogen-bonded Shells for Living Cell Surface Engineering," *Soft Matter*, **7**, 2364-2372 (2011).
- Lisunova, M. O., Drachuk, I.; Shchepelina, O. A.; Anderson, K.; Tsukruk, V. V., "Direct probing of micromechanical properties of hydrogen-bonded LbL microcapsule shells with different chemical compositions," *Langmuir*, **2011**, **27**, 11157-11165 (2011).
- M. Planells, L. Pellejà, J. N. Clifford, M. Pastore, F. De Angelis, N. López, S. R. Marder, E. Palomares, "Energy levels, charge injection, charge recombination and dye regeneration dynamics for donor-acceptor π -conjugated organic dyes in mesoscopic TiO_2 sensitized solar cells," *Energy & Environ. Sci.*, **4**, 1820-1829 (2011).
- Shchepelina, O.; Drachuk, I.; Gupta, M. K.; Lin, J.; Tsukruk, V. V. "Silk-on-Silk LbL Microcapsules," *Adv. Mater.*, **23**, 4655-4660(2011).

- Y. Shi, R. B. M. Hill, J.-H. Yum, A. Dualeh, S. Barlow, M. Grätzel, S. R. Marder, M. K. Nazeeruddin, *Angew. Chem., Int. Ed.*, **50**, 6619-6621 (2011)
- C. Ye, O. Shchepelina, R. Calabrese, I. Drachuk, D. L. Kaplan, V. V. Tsukruk, "Robust and Responsive Silk Ionomer Microcapsules," *Biomacromolecules*, **12**, 4319-4325 (2011).
- Y. Zhou, H. S. Cheun, S. Choi, C. Fuentes-Hernandez, B. Kippelen, "Optimization of a Polymer Top Electrode for Inverted Semitransparent Organic Solar Cells," *Org. Electron.*, **12**, 827-831 (2011).
- Anderson, D. M.; Gupta, M. K.; Voevodin, A. A.; Hunter, C. N.; Tsukruk, V. V., Fedorov, A. A., "Using Amphiphilic Nanostructures to Enable Long-Range Ensemble Coalescence and Surface Rejuvenation in Dropwise Condensation," *ACS Nano*, **6**, 3262-3268 (2012).
- K. D. Anderson, R. B. Weber, M. E. McConney, H. Jiang, T. J. Bunning, V. V. Tsukruk, "Responsive Plasma Polymerized Ultrathin Nanocomposite Films," *Polymer*, **53**, 4686-4693 (2012).
- K. D. Anderson, S. L. Young, H. Jiang, R. Jakubiak, T. J. Bunning, R. R. Naik, V. V. Tsukruk, "Plasma Enhanced Co-Polymerization of Amino Acid and Synthetic Monomers," *Langmuir*, **28**, 1833-1845 (2012).
- H. Cheun, C. Fuentes-Hernandez, Y. Zhou, Y. Fang, Y. Cai, H. Li, A. Sigdel, J. Meyer, J. Maibach, A. Dindar, J. Shim, J. Berry, J.-L. Bredas, A. Kahn, K.H. Sandhage, B. Kippelen, "Oriented Growth of Al₂O₃:ZnO Nanolaminates for Use as Electron-Selective Electrodes in Inverted Polymer Solar Cells," *Adv. Funct. Mater.*, **22** [7] 1531-1538 (2012).
- Drachuk, I.; O. Shchepelina, M. Lisunova, S. Harbaugh, N. Kelley-Loughnane, M. Stone, V. V. Tsukruk, "pH-Responsive LbL Nanoshells for Direct Regulation of Cell Activity," *ACS Nano*, **6**, 4266-4278 (2012).
- Y. Fang, J. D. Berrigan, Y. Cai, S. R. Marder, K. H. Sandhage, "Syntheses of Nanostructured Cu- and Ni-based Micro-assemblies with Selectable 3-D Hierarchical Biogenic Morphologies," *J. Mater. Chem.*, **22** (4) 1305-1312 (2012). (Highlighted in Editors' Choice section of the Jan. 20, 2012 edition of Science)
- Y. Fang, V. W. Chen, Y. Cai, J. D. Berrigan, S. R. Marder, J. W. Perry, K. H. Sandhage, "Biologically-enabled Syntheses of Freestanding Metallic Structures Possessing Subwavelength Pore Arrays for Extraordinary (Plasmon-Mediated) Infrared Transmission," *Adv. Funct. Mater.*, **22** [12] 2550-2559 (2012). (Back Cover)
- R. A. Gittens, R. Olivares-Navarrete, T. McLachlan, Y. Cai, S. L. Hyzy, J. M. Schneider, Z. Schwartz, K. H. Sandhage, B. D. Boyan, "Differential Responses of Osteoblast Lineage Cells to Nanotopographically-Modified, Microroughened Titanium-Aluminum-Vanadium Alloy Surfaces," *Biomater.*, **33** (35) 8986-8994 (2012).
- Hildreth, O., Fedorov, A., Wong, C. P., "3-D spirals with controlled chirality fabricated using metal-assisted chemical etching of silicon," *ACS Nano*, **6** (11), 10004-10012 (2012).
- D. K. Hwang, C. Fuentes-Hernandez, J. D. Berrigan, Y. Fang, J. Kim, W. J. Potscavage, C. Hyeunseok, K. H. Sandhage, B. Kippelen, "Solvent and Polymer Matrix Effects on TIPS-Pentacene/Polymer Blend Organic Field-Effect Transistors," *J. Mater. Chem.*, **22**, 5531-5537 (2012).

- D. W. Lipke, Y. Zhang, Y. Cai, K. H. Sandhage, "Intergranular Tungsten/Zirconium Carbide Nanocomposites via a Selective Liquid/Solid Displacement Reaction," *J. Am. Ceram. Soc.*, **95** [9] 2769-2772 (2012).
- M. E. McConney, D. Kulkarni, H. Jiang, T. J. Bunning, V. V. Tsukruk, "A New Twist on Scanning Thermal Microscopy," *Nano Lett.*, **12**, 1218-1223 (2012).
- R. Musin, M. A. Filler, "Chemical Control of Semiconductor Nanowire Kinking and Superstructure," *Nano Lett.*, **12**, 3363 (2012).
- Near, R.; Hayden, S.; El-Sayed, M., "Extinction vs Absorption: Which is the Indicator of Plasmonic Field Strength for Silver Nanocubes?," *J. Phys. Chem C*, **116** (43), 23019-23026 (2012).
- Near, R.; Tabor, C.; Duan, J. S.; Pachter, R.; El-Sayed, M., "Pronounced Effects of anisotropy on Plasmonic Properties of Nanorings Fabricated by Electron Beam Lithography," *Nano Lett.*, **12**, 2158-2164 (2012)
- S. Pavlidis, J.-J. Su, L. A. Beardslee, P. Leclaire, J. Hagen, N. Kelley-Loughnane, O. Brand, "Pulsed Operation of InGaZnO TFTs for VOC Sensing Applications," in *2012 IEEE Sensors*, Taipei, Taiwan, 2012.
- N. Shin, M. A. Filler, "Controlling Silicon Nanowire Growth Direction Via Surface Chemistry," *Nano Lett.*, **12**, 2865 (2012).
- J. P. Vernon, N. Hobbs, A. Lethbridge, P. Vukusic, D. D. Deheyn, K. H. Sandhage, "3-D Photoluminescent Lanthanide-doped Barium Titanate Structures Synthesized by Coating and Shape-preserving Reaction of Complex-shaped Bioorganic Templates," *J. Mater. Chem.*, **22** (21) 10435-10437 (2012). (Inside Front Cover)
- B. Wallet, E. Kharlampieva, K. Campbell-Proszowska, V. Kozlovskaya, S. Malak, J. F. Ankner, D. L. Kaplan, V. V. Tsukruk, "Silk Layering as Studied with Neutron Reflectivity," *Langmuir*, **28**, 11481-11489 (2012).
- S. L. Young, M. Gupta, C. Hanske, A. Fery, T. Scheibel, V. V. Tsukruk, "Utilizing Conformational Changes for Patterning Thin Films of Recombinant Spider Silk Proteins," *Biomacromolecules*, **13**, 3189-3199 (2012).
- J. D. Berrigan, T. M. McLachlan, J. R. Denault, Y. Cai, T.-S. Kang, M. F. Durstock, K. H. Sandhage, "Conversion of Porous Anodic Al₂O₃ into Freestanding, Uniformly-aligned, Multi-wall TiO₂ Nanotube Arrays for Electrode Applications," *J. Mater. Chem. A*, **1** (1) 128-134 (2013).
- Z. A. Combs, S. T. Malak, T. König, M. A. Mahmoud, J. L. Chávez, M. A. El-Sayed, N. Kelley-Loughnane, V. V. Tsukruk, "Aptamer-Assisted Assembly of Gold Nanoframe Dimers," *Particle*, **30**, 1071-1078 (2013).
- S. C. Davis, V. C. Sheppard, G. Begum, Y. Cai, Y. Fang, J. D. Berrigan, N. Kröger, K. H. Sandhage, "Rapid Flow-through Biocatalysis with High Surface Area, Enzyme-loaded Carbon and Gold-bearing Diatom Frustule Replicas," *Adv. Funct. Mater.*, **23** [36] 4611-4620 (2013).
- J. H. Delcamp, Y. Shi, J.-H. Yum, T. Sajoto, E. Dell'Orto, S. Barlow, M. K. Nazeeruddin, S. R. Marder, M. Grätzel, "The Role of π -Bridges in High-Efficiency DSCs Based on Unsymmetrical Squaraines," *Chem. Eur. J.*, **19**, 1819-1827 (2013)
- I. Drachuk, M. K. Gupta, V. V. Tsukruk, "Biomimetic coatings to control cellular function through cell surface engineering," *Adv. Funct. Mater.*, **23**, 4437-4453 (2013).

- Drachuk, I., O. Shchepelina, S. Harbaugh, N. Kelley-Loughnane, M. Stone, V. V. Tsukruk, "Cell Surface Engineering with Edible Protein Nanoshells," *Small*, **9**, 3128-3137 (2013).
- R. A. Gittens, R. Olivares-Navarrete, A. Cheng, D. M. Anderson, T. McLachlan, I. Stephan, J. Geis-Gerstorfer, K. H. Sandhage, A. G. Fedorov, F. Rupp, B. D. Boyan, R. Tannenbaum, Z. Schwartz, "The Roles of Titanium Surface Micro/Nanotopography and Wettability on the Differential Response of Human Osteoblast Lineage Cells," *Acta Biomater.*, **9** (35) 6268-6277 (2013).
- M. K. Gupta, T. Konig, R. Near, D. Nepal, L. F. Drummy, S. Biswas, S. Naik, R. A. Vaia, M. A. El-Sayed, V. V. Tsukruk, "Surface Assembly and Plasmonic Properties in Strongly Coupled Segmented Gold Nanorods," *Small*, **9**, 2979-2990 (2013).
- M. K. Gupta, D. D. Kulkarni, R. Geryak, S. Naik, V. V. Tsukruk, "A robust and facile approach to assembling mobile and highly-open unfrustrated triangular lattices from ferromagnetic nanorods," *Nano Lett.*, **13**, 36-42 (2013).
- Hayden, SC; Austin, LA; Near, RD; Ozturk, R; El-Sayed, MA. "Plasmonic Enhancement of Photodynamic Cancer Therapy," *J. Photochem. Photobiol., A*, **269**, 34-41 (2013).
- Hildreth, O., Rykaczewski, K., Fedorov, A., Wong, C. P., "A DLVO model for catalyst motion in Metal-assisted Chemical Etching based upon controlled out-of-plane rotational etching and force-displacement measurements," *Nanoscale*, **5**, 961-970 (2013).
- Y. Kim, M. Kathaperumal, O. Smith, M.-J. Pan, Y. Cai, K. H. Sandhage, J. Perry, "High Energy Density Sol-Gel Thin Film based on Neat 2-Cyanoethyltrimethoxysilane," *ACS Appl. Mater. Interf.*, **5** (5) 1544-1547 (2013).
- R. Musin, D. S. Boyuk, M. A. Filler, "Surface Chemistry Controlled Diameter-Modulated Semiconductor Nanowire Superstructures," *J. Vac. Sci. Technol. B*, **31** 020603 (2013).
- Near, R; Hayden, SC; El-Sayed, MA. "Thin to Thick, Short to Long: Spectral Properties of Gold Nanorods by Theoretical Modeling," *J. Phys. Chem. C*, **117**, 18653-18656 (2013).
- Near, R; Hayden, SC; Hunter, RE; Thackston, D; El-Sayed, MA. "Rapid and Efficient Prediction of Optical Extinction Coefficients for Gold Nanospheres and Gold Nanorods," *J. Phys. Chem. C*, **117**, 23950-23955 (2013).
- G. Thompson, M. Magnuson, M. Merritt, H. Schwarb, A. McKinley, L. Tripp, W.-J. Pan, E. H. Schumacher, S. D. Keilholz, "Short Time Windows of Correlation between Large Scale Functional Brain Networks Predict Vigilance Intra-individually and Inter-individually," *Hum. Brain Mapp.*, **34** (12) 3280-98 (2013).
- M. C. Vasudev, K. D. Anderson, V. V. Tsukruk, T. J. Bunning, R. R. Naik, "Exploration of Plasma-Enhanced Chemical Vapor Deposition as a Method for Thin Film Fabrication with Biological Applications," *ACS Appl. Mater. Interfaces*, **5**, 3983-3994 (2013).
- Fedorov, A., Kim, S, Henry, M., Kulkarni, D., Tsukruk, V. V., "Focused electron beam induced processing (FEBIP) for emerging applications in carbon nanoelectronics," *Appl. Phys. A – Mat. Sci. & Proc.*, **117** (4), 1659-1674 (2014) **invited**.
- R. D. Geryak, V. V. Tsukruk, "Reconfigurable and Actuating Structures from Soft Materials," *Soft Matter*, **10**, 1246-1263 (2014).

- Hooshmand, N; Bordley, JA; El-Sayed, MA. "Are Hot Spots between Two Plasmonic Nanoparticles of Silver or Gold Formed between Adjacent Corners or Facets? A DDA Examination," *J. Phys. Chem. Lett.*, **5** (13), 2229-2234.(2014).
- J. Icozzia, H. Xu, X. Pang, H. Xia, T. Bunning, T. White*, Z. Lin*, "Star-like polymer click-functionalized with small capping molecules: an initial investigation into properties and improving solubility in liquid crystals," *RSC Advances*, **4**, 50212-50219 (2014).
- S. Kim, D. Kulkarni, R. Davis, S. Kim, A. Voevodin, S. Jang, V. V. Tsukruk, A. G. Fedorov, "Controlling Physicochemical State of Carbon on Graphene Using Focused Electron Beam Induced Deposition," *ACS Nano*, **8**, 6805-6813 (2014).
- P. A. Ledin, I. Tkachenko, W. Xu, I. Choi, V. Shevchenko, V. V. Tsukruk, "Star-Shaped Molecules with POSS Core and Azobenzene Dye Arms," *Langmuir*, **30**, 8856-8865 (2014).
- Makcey, MA; Ali, MRK; Austin, LA; Near, R; El-Sayed, MA, "The Most Effective Gold Nanorod Size for Plasmonic Photothermal Therapy: Theory and In Vitro Experiments," *J. Phys. Chem. B*, **118**, 1319-1326 (2014).
- Malak, ST; Koenig, T; Near, R; Combs, ZA; El-Sayed, MA; Tsukruk, VV, "Stacked Gold Nanorectangles with Higher Order Plasmonic Modes and Top-Down Plasmonic Coupling," *J. Phys. Chem. C*, **118**, 5453-5462 (2014).
- V. Singh, T. L. Bougher, A. Weathers, Y. Cai, K. Bi, M. T. Pettes, S. A. McMenamin, W. Lu, D. P. Resler, T. R. Gattuso, D. H. Altman, K. H. Sandhage, L. Shi, A. Henry, B. A. Cola, "High Thermal Conductivity of a Chain-Oriented Amorphous Polythiophene," *Nature Nanotechnol.*, **9** (5) 384-390 (2014).
- R. Suntivich, I. Drachuk, R. Calabrese, D. L. Kaplan, V. V. Tsukruk, "Inkjet printing of silk nest arrays for cell hosting," *Biomacromolecules*, **15**, 1428-1435 (2014).
- C. Ye, D. D. Kulkarni, H. Dai, V. V. Tsukruk, "Programmable Arrays of "Micro-bubble" Constructs via Self-Encapsulation," *Adv. Funct. Mater.*, **24**, 4364-4373 (2014).
- M. N. Tapp, R. Sullivan, P. Dennis, R. N. Naik, V. T. Milam, "Effects of nucleic acid additions on seed-mediated growth of gold nanoparticles," *J. Mater. Res.*, accepted, in press.
- C. Ye, V. V. Tsukruk, "Materials Springing into Three-dimensional Shape," *Science*, 2015, in press.

Interdisciplinary Research Group (IRG) #1: Functional Nanocomposites
IRG Leader: Kenneth H. Sandhage

Project IRG #1-1: Syntheses and Chemical Tailoring of Bio-Enabled Nanostructured Functional Materials

Georgia Tech Participants: Project PI: Prof. Kenneth H. Sandhage; Students: J. Dan Berrigan (now Dr. Berrigan), Taylor McLachlan, Ben deGlee; Post-docs/Research Scientists: Dr. Ye Cai, Dr. Yunnan Fang

University Collaborators: Prof. Nils Kröger, Prof. Bernard Kippelen

AFRL Collaborators: WPAFB: Dr. Michael F. Durstock, Dr. Rajesh R. Naik, James Deneault, Dr. Giorgio Bazzan, Dr. Matthew B. Dickerson, Dr. Lawrence Drummy, Dr. Jacob Haag, Dr. T.-S. Kang, Dr. Sang Kim, Dr. Ben Leever, Dr. Gyanaranjan Pattanaik; Tyndall AFB: Dr. Glenn Johnson, Dr. Heather Luckarift, Dr. Guin Strack

Research Goals:

- To understand how to utilize bio-enabled layer-by-layer deposition methods, synthetic layer-by-layer deposition methods and/or gas-solid reactive conversion methods to synthesize aligned, functional nanotube arrays.
- To learn how to tailor nanotube structures, by varying deposition and reaction conditions, for enhanced electrochemical performance.

Key Achievements:

- An automated aqueous protein-enabled layer-by-layer (LbL) deposition process has been used for the first time to synthesize aligned arrays of thin-walled (35 nm), high-aspect-ratio (tube height:wall thickness = 291:1), porous titania nanotubes. The interconnected pores in the tube walls allowed for enhanced molecular loading (e.g., of a ruthenium-based N719 dye), whereas the interconnected anatase nanocrystals allowed for effective electron conduction down the tube length. Dye sensitized solar cells constructed with such arrays possessed reproducible efficiencies of $5.2 \pm 0.4\%$.
- The kinetic behavior of layer-by-layer (LbL) polyamine-enabled titania deposition has been evaluated via *in situ* quartz crystal microbalance (QCM) and *ex situ* atomic force microscopic (AFM) analyses. For protamine-enabled deposition, the thickening of titania-bearing films initially occurred at an accelerating rate with the number of deposition cycles. For synthetic polyethyleneimine-enabled deposition, on the other hand, only a linear change in coating thickness with the number of deposition cycles was observed. Mechanistic models for such protein-enabled deposition have been developed.
- Aligned, multiwalled anatase titania nanotube arrays have been synthesized using a hybrid sol-gel/gas-solid displacement reaction method. Such arrays showed improved resistance to bundling/islanding, and exhibited a factor of 2.4 higher dye loading, than for sol-gel-derived single wall nanotube arrays. DSSCs constructed with the multi-walled nanotube arrays exhibited an average efficiency (5 devices) of 5.5% (6.5% maximum) compared to 3.0% for DSSCs with sol-gel-derived single-wall nanotubes.
- Porous anodic alumina membranes (PAAMs) have been reactively converted into TiO_2 membranes with aligned channels of ~ 175 nm diameter. DSSCs with such TiO_2 -converted membranes exhibited efficiencies of $4.5 \pm 0.3\%$. This reactive-conversion method has also been successfully applied to sulfuric-acid-derived PAAMs to yield TiO_2 membranes with ~ 20 nm dia. channels. Construction of DSSCs with such fine-channeled replicas is underway.

- The reactive conversion of porous anodic aluminum oxide (AAO) templates, with aligned channels possessing average diameters of about 20 nm, 70 nm, or 250 nm, has been examined. For each type of template, reaction conditions have been identified that led to titania-coated channels over the entire thickness (12-15 μm) of the AAO template. Refinement of reaction conditions, and the conditions for selective alumina dissolution, are underway to generate freestanding TiO_2 nanotube arrays of varied nanotube density for subsequent incorporation in, and testing of, dye sensitized solar cells with the Durstock group.
- Isothermal kinetic studies of the reactive conversion of planar Al_2O_3 templates (single crystal, polycrystal, or amorphous alumina) into TiOF_2 at temperatures in the range of 180-250°C for 2-24 h have been conducted via use of dynamic high temperature X-ray diffraction (HTXRD) and static high resolution transmission electron microscopic (HRTEM) analyses. Comparison of the kinetic data with models for various rate-limiting steps is underway.

Approaches and Results:

A Protamine-Enabled, Layer-by-Layer, Oxide Deposition Route to Aligned, Porous-Wall TiO_2 Nanotube Arrays (e.g., for dye-sensitized solar cell electrodes):

The evaluation and development of a protein-enabled layer-by-layer (LbL) deposition process for applying conformal oxide/protein or porous oxide (upon organic pyrolysis) coatings of tailorable thickness onto 1-D, 2-D, and 3-D inorganic templates has been a key thrust of project IRG #1-1. A variety of inorganic templates have been examined, including alumina (Al_2O_3), silica (SiO_2), and graphene (C).

This bio-enabled process has been examined, for example, as a means of generating

freestanding, aligned, porous-wall titania (TiO_2) nanotube arrays for use as electrodes in dye-sensitized solar cells (DSSCs). For these structures, porous anodic alumina membranes (PAAMs) were utilized as suitable templates for such coating due to the highly-aligned nanopore channel structure of the PAAMs. Anodization of aluminum foil, and then wet chemical etching of the residual aluminum backing, were used to generate through-hole PAAMs with typical thicknesses of $9.9 \mu\text{m} \pm 0.4 \mu\text{m}$ and

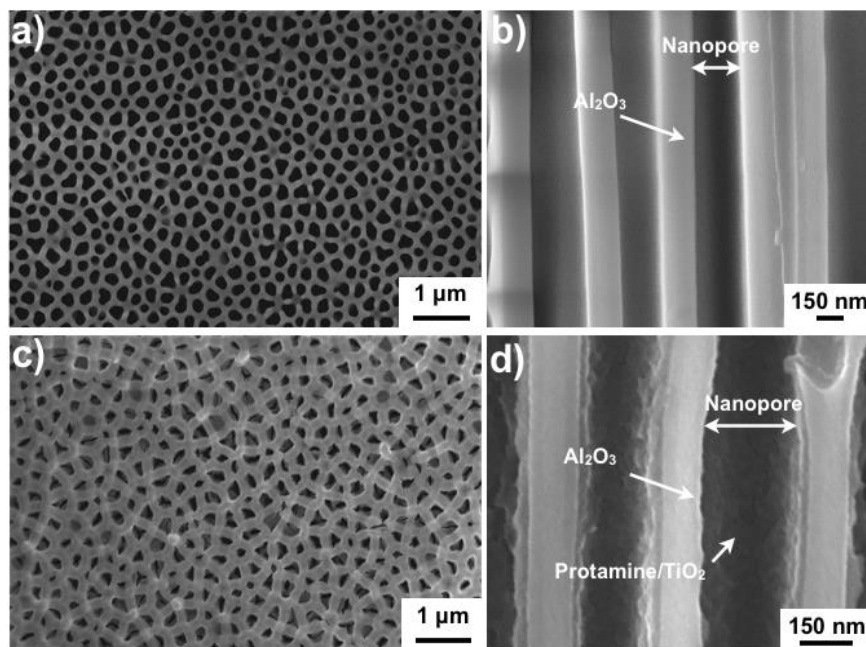


Figure #1-1.1. Secondary electron images of: **a)** the top and **b)** cross-section of an uncoated PAAM template, and **c)** the top and **d)** cross-section of such a template after coating with 8 protamine/ TiBALDH deposition cycles.

pore channel diameters of $284 \text{ nm} \pm 8.0 \text{ nm}$. Representative secondary electron images of such PAAM templates are shown in **Figures #1-1.1a and b**.

The bio-enabled LbL coating of the through-hole PAAMs with titania was conducted using the polycationic protein, protamine, as a multifunctional biomolecule capable of both binding to, and inducing the precipitation of, titania. This approach was derived from prior collaborative research between the Naik and Sandhage groups on the identification of peptide characteristics needed for such titania binding and precipitation. An automated pumping system developed by the Sandhage group has been used to alternately expose the PAAMs to aqueous protamine-bearing and titania precursor-bearing (titanium bis-ammoniumlactato-dihydroxide, TiBALDH) solutions to build up conformal and continuous protamine/titania composite layers. Zeta potential measurements obtained after alternating exposure of crushed PAAM membranes to protamine-bearing or TiBALDH-bearing solutions are shown in **Figure #1-1.2**. After incubation of the crushed PAAMs in buffer solution at pH 8.5, the PAAM templates exhibited a net negative zeta potential, which was consistent with literature reports for the isoelectric point of Al_2O_3 . Once exposed to a protamine solution at pH 8.5, electrostatic forces induced the polycationic protamine to bind to the negatively-charged alumina surface, which caused a change in the measured zeta potential to a net positive value. A regular oscillation in the measured zeta potential was observed after each alternating exposure to the buffered (pH 8.5) protamine and TiBALDH solutions, which was consistent with the presence of an external layer of positively-charged protamine molecules or of negatively-charged TiO-bearing layers, respectively.

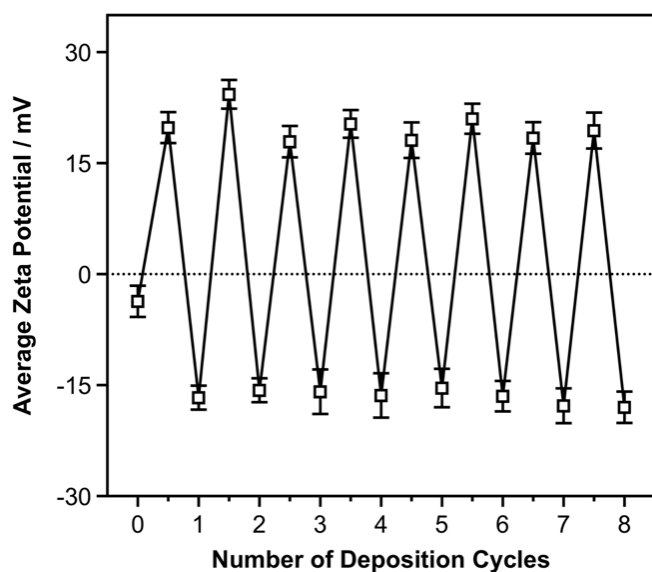


Figure #1-1.2. Zeta potential measurements obtained from crushed PAAM templates after various stages of alternating exposure to aqueous protamine-bearing (steps 0.5, 1.5, 2.5, 3.5, 4.5, 5.5, 6.5, and 7.5) and TiBALDH-bearing (steps 1, 2, 3, 4, 5, 6, 7, 8) solutions. The first measurement (0 cycles) was obtained from the starting crushed PAAM template. The error bars correspond to the complete range of measured values.

In-situ quartz-crystal microbalance (QCM) and *ex-situ* atomic force microscopy (AFM) and electron microscopy (SEM, TEM) indicated that the thickness of the protamine/titania coating applied to alumina increased monotonically with the number of protamine/TiBALDH deposition cycles. X-ray photoelectron spectroscopic (XPS) analyses of coated PAAM surfaces are shown in **Figure #1-1.3a**. The low- and high-resolution XPS spectra revealed peaks for Ti and O (consistent with titania), N and C

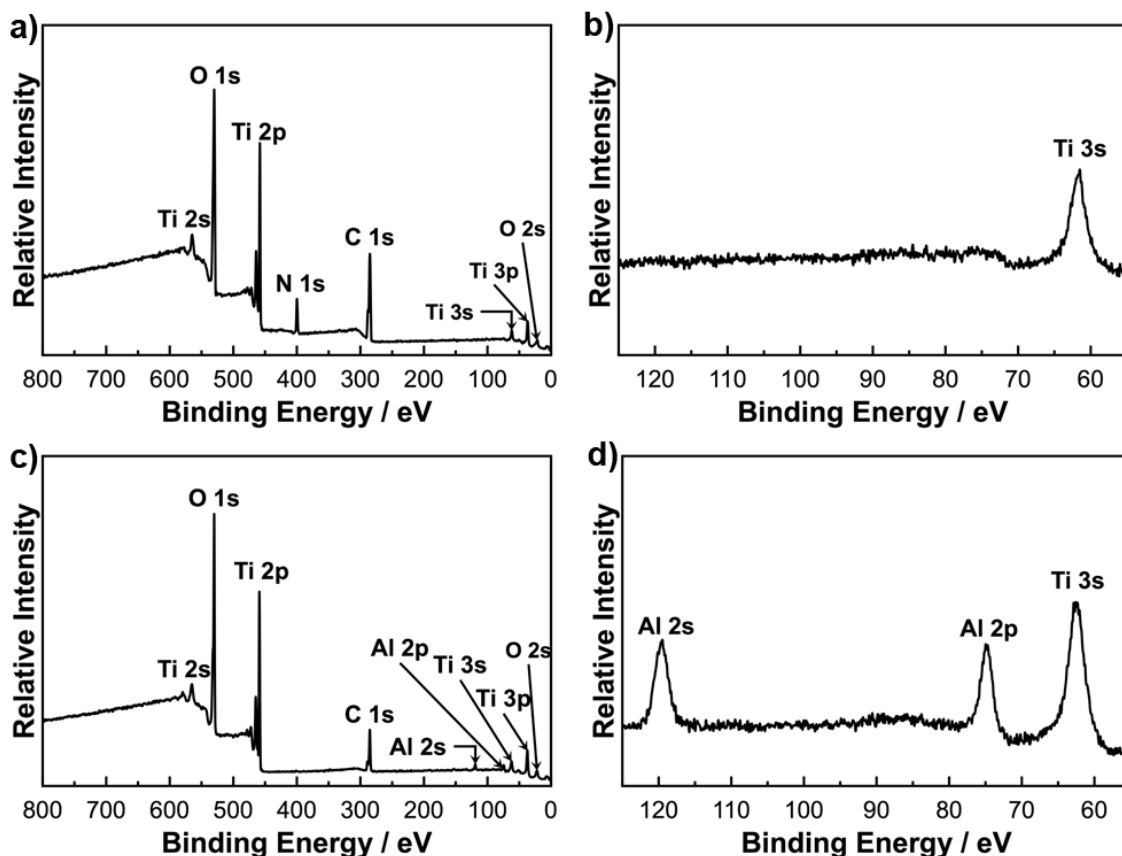


Figure #1-1.3. X-ray photoelectron spectroscopic analyses of: **a), b)** PAAM templates after exposure to 8 protamine/TiBALDH deposition cycles and **c), d)** after subsequent heat treatment at 650 °C for 3 h in air (c, d).

(consistent with protamine), but not for Al, which indicated that the protamine/TiO-bearing composite coating (generated with 8 protamine/TiBALDH deposition cycles) completely covered the TP-AAO template to a thickness of at least 10 nm (i.e., greater than the XPS information depth). Secondary electron images of PAAM templates after exposure to 8 protamine/TiBALDH deposition cycles are shown in **Figures #1-1.1c and d**. Such SEM analyses indicated that the conformal, LbL nature of the protamine-enabled process allowed the internal nanochannel surfaces of the PAAM templates to be continuously coated without plugging of the nanopore channels at the external top and bottom faces of the templates.

The protamine/Ti-O-coated PAAM templates were then heated at 5°C min⁻¹ to 650 °C in air and held at this temperature for 3 h to allow for water removal, organic pyrolysis, and titania crystallization. Thermogravimetric analysis (TGA), shown in **Figure #1-1.4**, revealed an initial reduction in weight upon heating through 100°C, which was consistent with the loss of water, followed by a second larger weight reduction (44 wt%) from about 200°C to 475 °C, which was attributed to protamine pyrolysis. The latter weight loss indicated that appreciable protamine was entrained along with titania in the deposited coating.

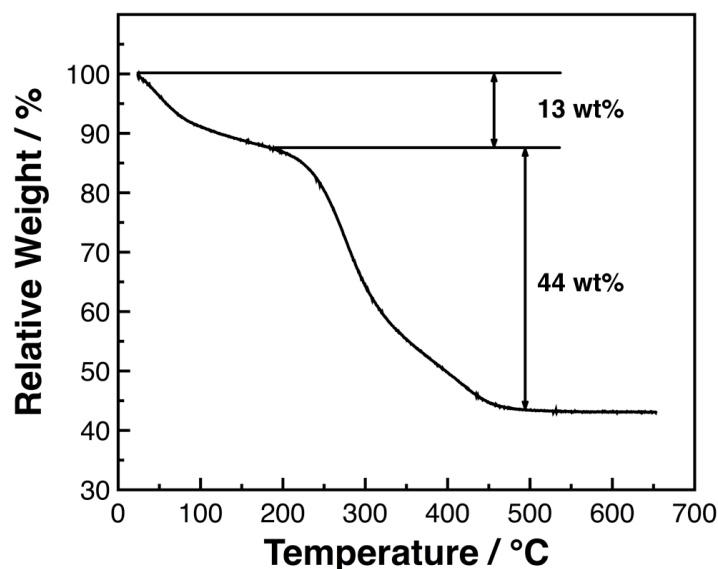


Figure #1-1.4. Thermogravimetric analysis of a protamine/Ti-O-coated PAAM template (after exposure to 8 protamine/TiBALDH deposition cycles) upon heating at $5^{\circ}\text{C min}^{-1}$ to 650°C in air.

The structural interconnectivity of the titania nanoparticle network in the fired coatings resulted in freestanding, high-aspect-ratio titania nanotube (e.g., a $9.9\text{ }\mu\text{m}$ length: 35 nm nanotube wall thickness yielded a 291:1 aspect ratio) arrays upon removal of the alumina template by selective dissolution. X-ray diffraction (XRD) analyses of freestanding tubes yielded peaks

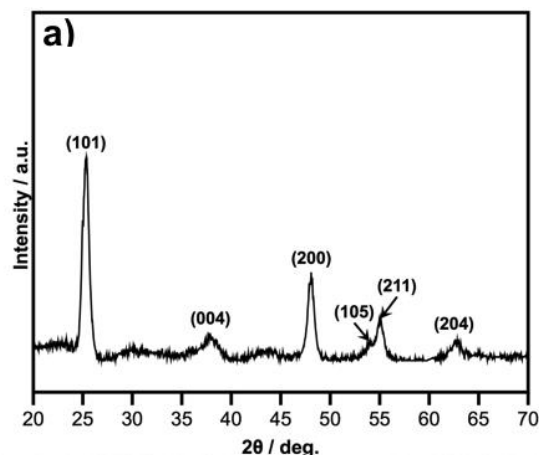
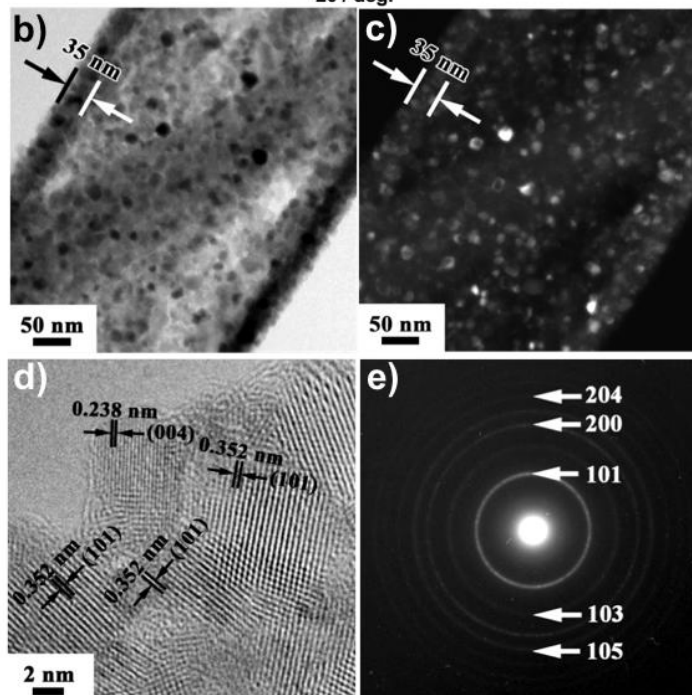
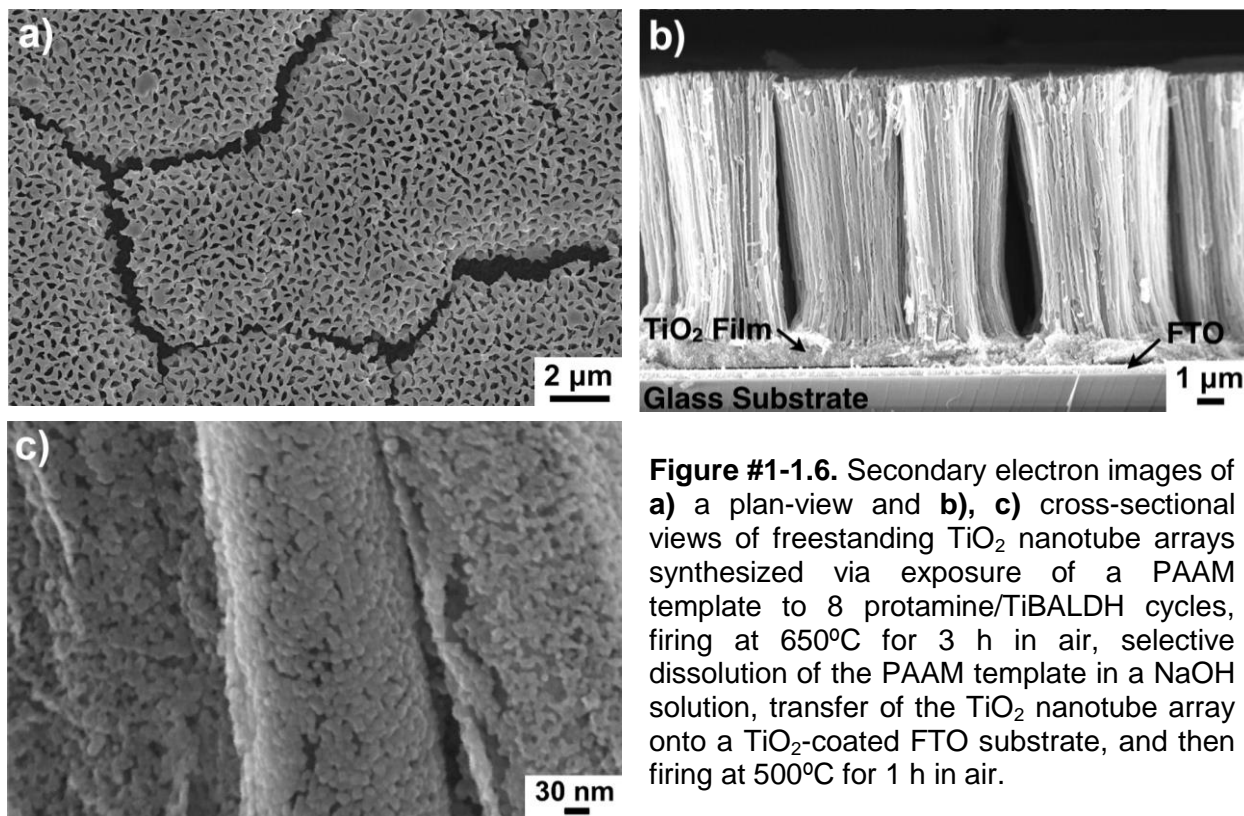


Figure #1-1.5. **a)** X-ray diffraction pattern obtained from a titania nanotube array synthesized via exposure to 8 protamine/TiBALDH cycles and then firing at 650°C for 3 h in air (hkl values are shown corresponding to diffraction peaks associated with anatase titania). **b)** Bright-field and **c)** and dark-field transmission electron images of a cross-section of a titania nanotube in such an array. **d)** High-resolution transmission electron image and **e)** selected area electron diffraction analysis of the titania nanotube shown in b) and c).



for anatase titania (**Figure #1-1.5a**). Scherrer analysis of the anatase diffraction peaks yielded an average crystallite size of 15 ± 3 nm. Transmission electron micrographs (**Figures #1-1.5b** and **c**) indicated that the freestanding titania nanotubes were comprised of a porous network of nanoparticles with sizes on the order of 10 to 20 nm (i.e., the titania crystals and titania particles seen in **Figures #1-1.5b** and **c** were comparable in size). In dark-field TEM analyses, the crystallites aligned with the zone axis displayed bright contrast, and a comparison between bright-field and dark-field images showed the nanotubes were comprised of randomly-oriented polycrystalline titania. High-resolution transmission electron microscopy images (**Figure #1-1.5d**) exhibited lattice fringes spaced 0.24 nm and 0.35 nm apart, which were consistent with the (004) and (101) inter-planar spacings of anatase titania, respectively. Selected area electron diffraction analyses (**Figure #1-1.5e**) also yielded ring patterns consistent with polycrystalline anatase titania.

The nanotube arrays were then transferred and attached to a transparent conducting oxide (fluorine-doped tin oxide, FTO) substrate with the aid of nanocrystalline titania paste. The transferred nanotube arrays maintained the geometry of the original template, with nanotube external diameters of $294 \text{ nm} \pm 13 \text{ nm}$, and lengths of $10.4 \mu\text{m} \pm 0.5 \mu\text{m}$ (**Figure #1-1.6**). Some agglomeration of the TiO_2 nanotubes occurred due to the attractive capillary forces upon drying in air, as evidenced by a change in the average pore-to-pore spacing from $400 \text{ nm} \pm 16 \text{ nm}$ (for the titania-PAAM samples) to $341 \text{ nm} \pm 15 \text{ nm}$ (for the transferred titania nanotube arrays).



Experiments were conducted to evaluate the extent of adsorption of a ruthenium-based dye onto the porous nanotube arrays. After rigidly attaching the nanotube arrays to an FTO-coated glass substrate as discussed above, N719 dye was adsorbed onto

the porous titania nanotubes for 24 h at room temperature. After dye absorption, the nanotube assembly was rinsed in dry acetonitrile and dried in air. The dye was then desorbed from the nanotubes by immersion in 0.1 M NaOH solution. The concentration of the dye in this solution was evaluated by measurement of the absorbance at 513 nm and compared to calibration solutions of known N719 concentration. The average specific N719 dye loading was found to be $1.63 \cdot 10^{-4} \pm 0.70 \cdot 10^{-4} \text{ mol g}^{-1}$ (normalized to the weight of titania in the nanotube assembly), which was more than twice the amount of such N719 dye adsorbed onto (less porous) titania nanotube arrays prepared via a sol-gel infiltration process ($7.42 \cdot 10^{-5} \text{ mol g}^{-1}$) developed by the Durstock group.

To demonstrate the feasibility of using such aligned, porous-wall, high-aspect-ratio nanotube arrays as working electrodes, the titania nanotube arrays were incorporated into DSSCs. After adsorption of the N719 dye onto the nanotubes and attachment of a platinized FTO-bearing electrode, a redox electrolyte solution (0.6 M 1-butyl-3-methyl imidazolium iodide, 0.1 M guanidinium thiocyanate, 0.03 M I_2 , and 0.5 M tert-butylpyridine in acetonitrile and valeronitrile) was vacuum infiltrated into the nanotube arrays. An optical image of such an assembled DSSC and a schematic illustration are shown in **Figure #1-1.7**.

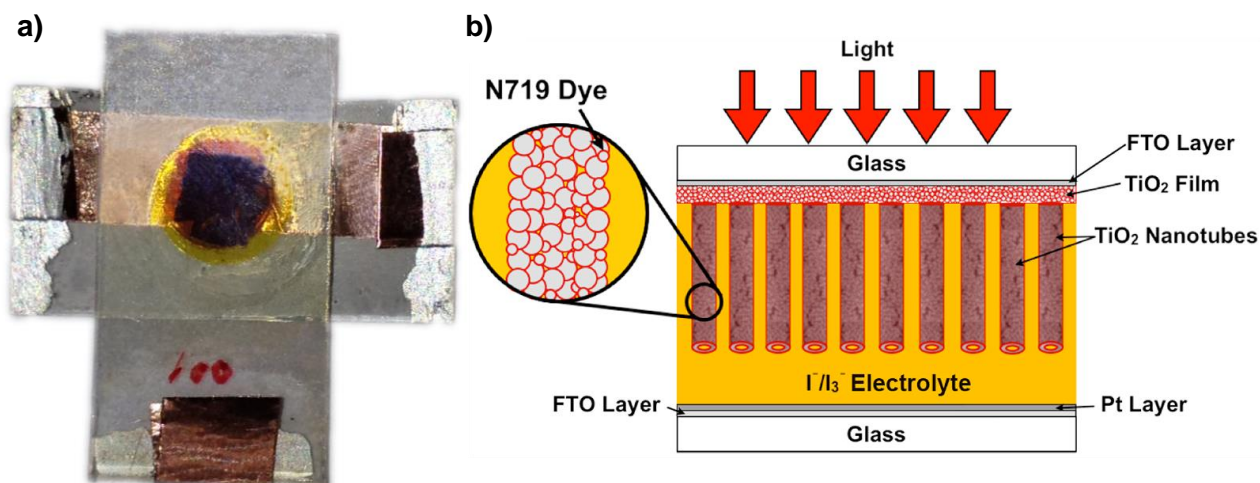


Figure #1-1.7. a) A completed titania nanotube-based DSSC with FTO glass that measured 1.3 cm x 2.5 cm, and b) a schematic illustration of such a DSSC.

Eight DSSCs were constructed from anatase TiO_2 nanotube arrays synthesized via the LbL peptide-enabled deposition process using 8 protamine/TiBALDH deposition cycles. The J - V behavior of such a DSSC in the dark and under AM 1.5G illumination is shown in **Figure #1-1.8**. These eight devices exhibited an average open-circuit voltage (V_{oc}) of $757 \pm 22 \text{ mV}$, an average short-circuit current density (J_{sc}) of $9.4 \pm 0.6 \text{ mA cm}^{-2}$, and an average fill factor (FF) of 0.73 ± 0.02 , yielding an average power conversion efficiency (η_{eff}) of $5.2 \pm 0.4\%$. These fill factor and open-circuit voltage values were comparable to values reported for DSSCs synthesized with mesoporous titania thick film electrodes ($FF = 0.70$ - 0.74 , $V_{oc} = 778$ - 791 mV). However, the values of short-circuit current density and power conversion efficiency were lower than values reported for DSSCs based upon mesoporous titania films, which can be explained by comparing roughness factors. The roughness factor is a measure of the internal surface area of a

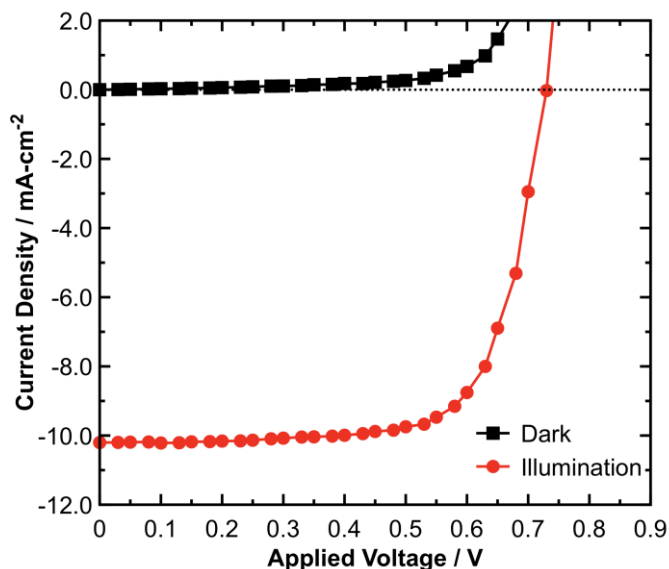


Figure #1-1.8. The J - V characteristics of a porous-wall TiO_2 nanotube-bearing dye-sensitized solar cell in the dark (■) and under illumination (●).

structure relative to its projected surface area. For commercially available TiO_2 nanoparticles, the roughness factor is generally on the order of 1000. The roughness factor of the protamine-enabled nanotube arrays was estimated by calculating both their geometric surface area and areal density. For nanotubes with an outer diameter of 284 nm, wall thickness of 35 nm and length of 9.9 μm , the total surface area per tube was approximately 16.6 μm^2 . After removing the template, the nanotubes were organized in a roughly hexagonal arrangement with a tube-to-tube spacing of approximately 340 nm leading to an area density of 9.99 nanotubes per μm^2 (or 0.10 μm^2 of projected area per tube) given three nanotubes per hexagonal area. The ratio of these two numbers (16.6:0.1) yielded an estimated roughness factor of 166 ± 50 . The reduced surface area compared to mesoporous TiO_2 negatively affected the molar quantity of dye adsorbed, which in turn led to a reduction in photocurrent density and device efficiency. The present short-circuit current values are relatively high given the modest percentage (24%) of the cross-sectional area (**Figure #1-1.9**) occupied by the porous titania walls (i.e., the surfaces available for dye loading) of the nanotube arrays. Further work to optimize the nanotube wall thickness and length for enhanced dye loading and short-circuit current density, along with modifications of DSSC construction (e.g., reduction of nanotube bundling, use of a light-scattering layer, use of an anti-reflecting film), may be pursued to achieve higher power conversion efficiencies.

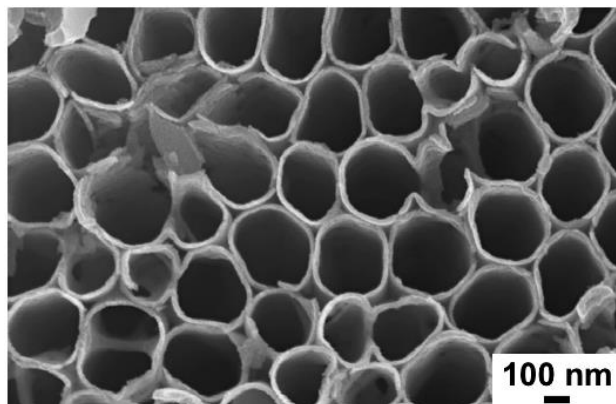


Figure #1-1.9. Plan-view secondary electron image of bundled titania nanotubes (where the interconnected titania layer is missing) upon template dissolution illustrating the relatively high void space due to the nanotube geometry used in this work.

A Hybrid Coating and Reactive Conversion Route to Aligned, Multiwalled TiO₂ Nanotube (MWTNT) Arrays (e.g., for dye-sensitized solar cell electrodes):

A novel hybrid (coating + reaction) strategy, involving combined use of sol-gel infiltration (as per a protocol developed by the Durstock group) and a gas/solid displacement reaction (as per an approach developed by the Sandhage group), has been developed to synthesize multi-walled titania nanotube (MWTNT) arrays (see the schematic illustration in **Figure #1-1.10**). After vacuum infiltration of a PAAM (13.2 μm ave. thickness, 207 nm ave. channel dia.) with a sol-gel precursor and then thermal conversion of the precursor coating into anatase TiO₂, the underlying PAAM was partially etched (3M NaOH solution, 20 min) to generate a gap (~ 100 nm wide) between the TiO₂ coating and the PAAM. The remaining Al₂O₃ was then converted into anatase TiO₂ using a gas-solid displacement reaction process (see discussion below).

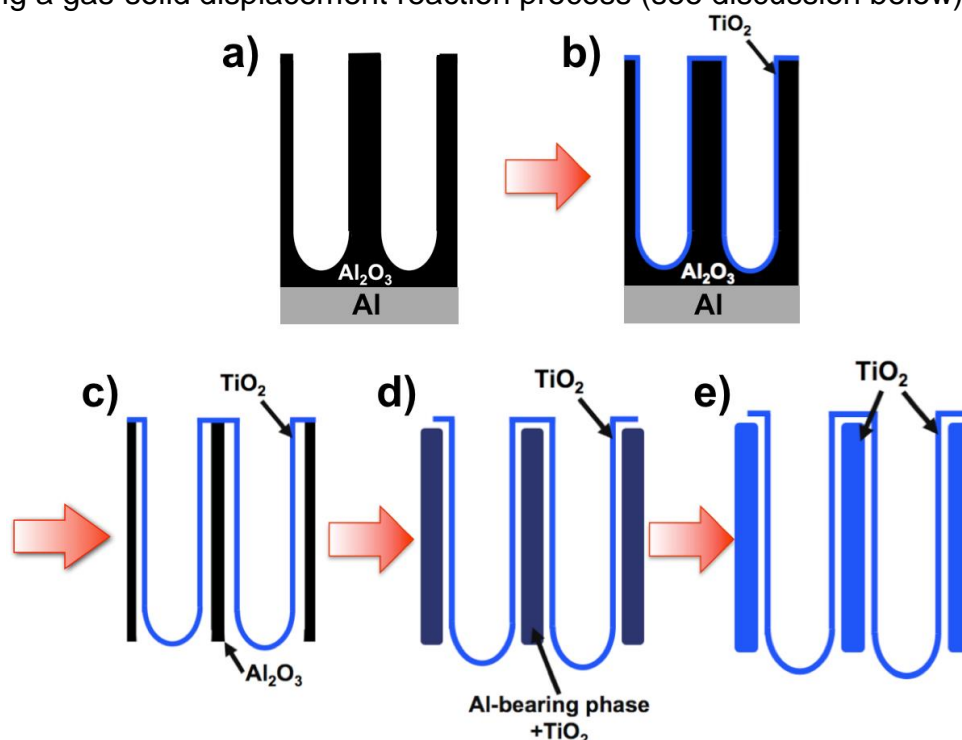


Figure #1-1.10. A schematic illustration of the hybrid sol-gel coating/gas-solid reaction procedure for the syntheses of MWTNT arrays, which began with **a)** a PAAM template. **b)** A TiO₂ coating was then deposited within the nanochannels using titanium(IV) isopropoxide, and **c)** the underlying aluminum substrate and Al₂O₃ barrier layer of the AAO were then removed. The partially etched TiO₂-coated PAAM was then **d)** reacted with TiF₄ vapor and heat treated under water vapor flow, followed by **e)** selective dissolution of any residual AlF₃ and Al₂O₃ to yield an all-TiO₂ assembly.

PAAM templates (**Figures #1-1.11a and b**) were vacuum-infiltrated with titanium (IV) isopropoxide in anhydrous isopropanol (3:1 weight ratio) and allowed to hydrolyze in air ($\sim 40\%$ relative humidity). This coating process was repeated to increase the nanotube wall thickness and ensure complete conformal coating of the PAAM nanochannels. Secondary electron (SE) images of such a coated template in plan view and cross-section after heat treatment (500°C for 3 h) to crystallize the oxide coating and pyrolyze any residual organics are shown in **Figures #1-1.11c and d**. From fracture cross-

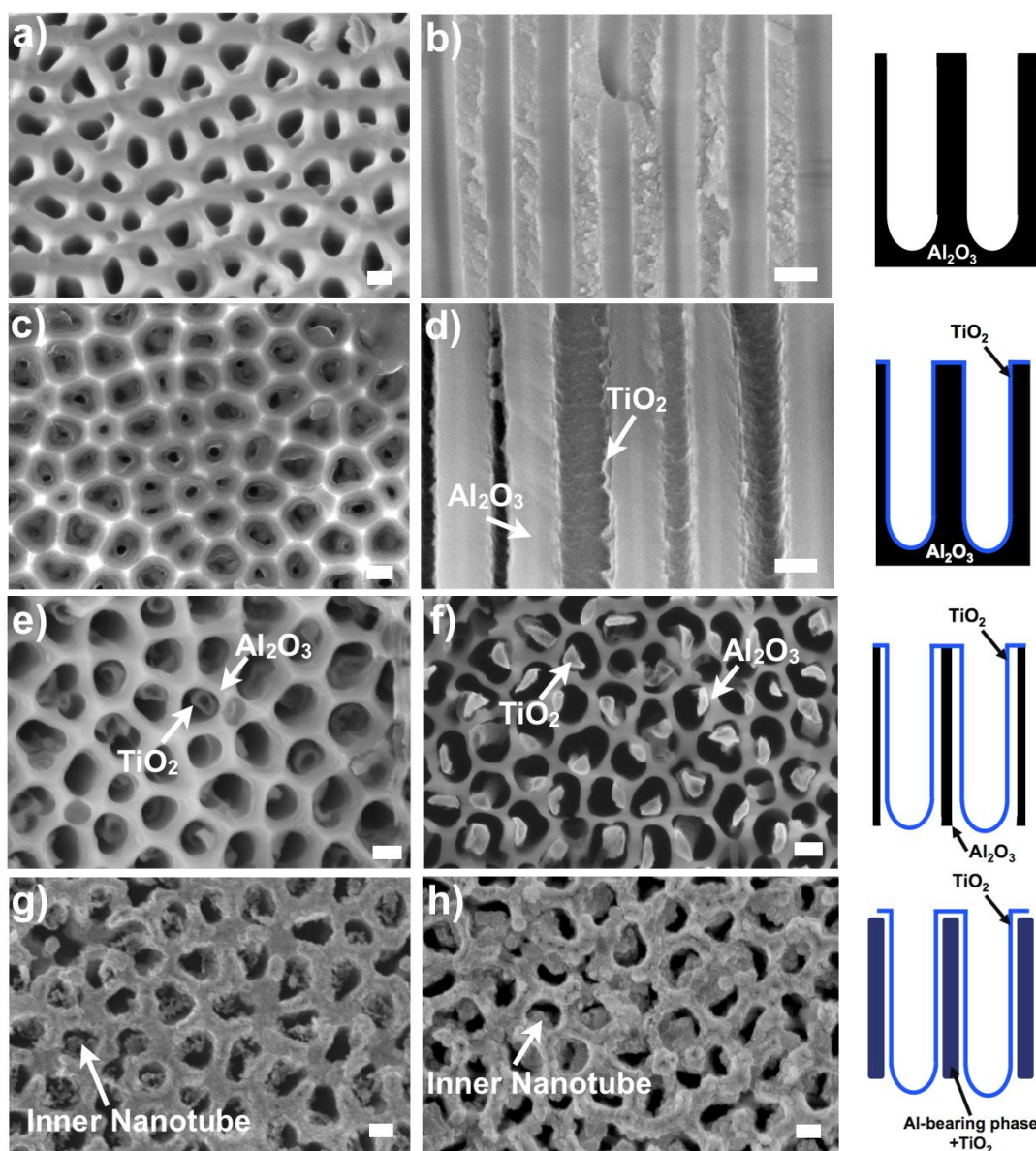


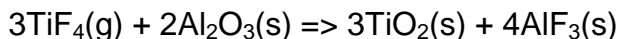
Figure #1-1.11.: **a)** Plan view and **b)** cross-sectional (b) secondary electron (SE) images of an anodic alumina (PAAM) template. **c), d)** SE images of the same template in plan view and in cross-section after two sol-gel vacuum infiltrations of titanium(IV) isopropoxide and heat treatment at 500°C for 3 h. **e), f)** SE images of the top and bottom of a sol-gel infiltrated PAAM template after aluminum substrate removal and nanochannel widening in NaOH. **g), h)** SE images of the top and bottom of the sol-gel infiltrated template after gas/solid reactive conversion of the AAO into TiO_2 at 335°C for 8 h and subsequent hydrolysis at 250°C for 8 h. A schematic (right) illustrates each step in the process. All scale bars indicate 200 nm.

section images, the thickness of the sol-gel coating was found to be 34 ± 15 nm.

Before gas/solid displacement reaction of the coated PAAM template, both the aluminum substrate and the closed-end of the template were removed by wet chemical etching. This selective etching step accomplished several objectives: (1) to remove aluminum so as to improve access of $\text{TiF}_4(\text{g})$ to the AAO template for reactive

conversion into TiOF_2 ; (2) to create space between the AAO template and the TiO_2 coating such that reactive conversion can occur throughout the nanochannel length, and (3) to enhance the surface area available for dye adsorption and electrolyte infiltration. SEM images of the top and bottom of the partially etched, TiO_2 -coated template are shown in **Figures #1-1.11e** and **f**. The sol-gel derived nanotubes were clearly visible and observed to adhere to one side of the widened nanochannels.

The partially-etched, TiO_2 -infiltrated PAAM was then completely converted into TiO_2 via a two-step gas/solid displacement reaction procedure developed by the Sandhage group. This process involved use of the following metathetic reaction:



Figures #1-1.11g and **h** show SE images of the top and bottom of TiO_2 -coated, partially etched PAAM templates after such gas/solid reactive conversion of the AAO with TiF_4 vapor. After halide reaction, the residual PAAM template appeared to increase in thickness, which was expected given the calculated increase in volume (235%) associated with the reaction of Al_2O_3 to TiO_2 and AlF_3 according to the reaction above. More importantly, the aligned structure of the TiO_2 nanotube and PAAM template was preserved after reaction of the remaining PAAM with TiF_4 vapor.

After reactive conversion and oxygenation, the templates were mounted on glass slides and incubated in NaOH to selectively dissolve residual Al-bearing species (e.g., AlF_3 or unreacted Al_2O_3). Note: Al_2O_3 and AlF_3 are both soluble in aqueous NaOH solution at room temperature. SEM images shown in **Figure #1-1.12** illustrate the successful synthesis of MWTNTs using this hybrid method of sol-gel deposition and gas/solid displacement reaction. **Figures #1-1.12a** and **b** show fractured MWTNTs with a sol-gel derived inner nanotube surrounded by an outer gas/solid reaction derived nanotube. From plan-view SEM images (**Figures #1-1.12.c** and **d**), the sol-gel derived

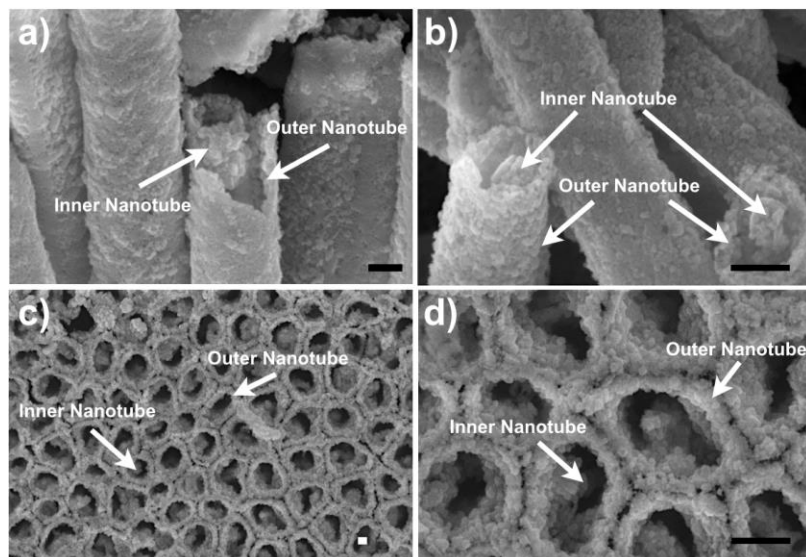


Figure #1-1.12. a), b) SEM images of broken MWTNTs and c) low and d) high-magnification plan-view images of MWTNT arrays synthesized by sol-gel vacuum infiltration followed by TiF_4 gas/solid reaction and selective dissolution of Al-bearing compounds. All scale bars indicate 200 nm.

nanotube core can be observed consistently within the outer reactively converted nanotube. Interestingly, the end of the inner nanotube was closed due to the structure of the PAAM template during sol-gel infiltration and was retained after gas/solid reaction. The average dimensions of these MWTNT arrays, determined from 20 measurements in five different areas, are given in **Table #1-1.1**. The initial wall thickness of sol-gel-

derived TiO₂ nanotubes was 30 ± 10 nm. The average diameters of the inner sol-gel derived nanotubes and the gas-solid reaction-derived nanotubes were 154 ± 40 nm and 426 ± 75 nm, respectively. Measurements taken of the widened PAAM nanochannel yielded an average diameter of 363 ± 30 nm, and after reactive conversion, the nanotube wall thicknesses were measured to be 34 ± 7 nm and 80 ± 13 nm for the inner and outer nanotubes, respectively. These values were used to calculate the difference in roughness factor between SWTNT and MWTNT arrays.

Table #1-1.1. Average dimensions of inner and outer nanotubes after gas/solid conversion.^a

Inner Nanotube Wall Thickness (nm)	Outer Nanotube Wall Thickness (nm)	Inner Nanotube Diameter (nm)	Outer Nanotube Diameter (nm)	Nanotube Length (μm)
34 ± 7	80 ± 13	154 ± 40	426 ± 75	13.2 ± 0.4

^a Averaged from 10 measurements taken on 5 different SEM images. The error corresponds to the absolute range measured.

The roughness factor (rugosity) is a ratio between the real surface area and the projected surface area. Roughness factors for MWTNT arrays were calculated using the measured dimensions of the MWTNTs after dissolution of residual AlF₃ and Al₂O₃. The average (real) surface area of a single inner and outer nanotube were estimated as 10.0 ± 2.4 μm² and 28.7 ± 5.8 μm², respectively using the average values for the nanotube dimensions listed in **Table #1-1.1**. The sum of these two areas yielded an average total nanotube surface area of 38.7 ± 8.2 μm². Assuming a hexagonal arrangement of nanotubes, three pairs of nanotubes per hexagonal area, and an average channel center-to-channel center spacing of 398 ± 70 nm, the areal density was 7.3 nanotubes per μm² or 0.137 μm² per nanotube (projected surface area). The ratio of these two numbers (38.7:0.137) which yielded a roughness factor of approximately 282 ± 99 , which was 3.8 and 2.6 times larger than SWTNT arrays synthesized by sol-gel infiltration (75 ± 37) and peptide-enabled deposition (107 ± 50), respectively. The error reported in the estimates of roughness factor corresponded to the absolute range of roughness factors calculated using the absolute range of geometric parameters measured. The combination sol-gel/reactive conversion method presented here is a first demonstration of the syntheses of aligned MWTNT arrays with two concentric TiO₂ nanotubes. In principle, an increase in the number of concentric TiO₂ nanotubes and/or longer nanotubes (controlled by template processing) can further improve the roughness factor beyond what is typical for standard mesoporous TiO₂ films (~1000).

To determine the advantages of MWTNT arrays when integrated into DSSC devices, SWTNT arrays were synthesized with the same sol-gel precursor infiltration procedure used for MWTNT syntheses. Both arrays were attached to FTO glass with the aid of TiO₂ nanoparticle paste (1.8 ± 0.2 μm thick), and fracture cross-sections of each electrode are shown in **Figure #1-1.13**. Both nanotube arrays were fabricated from the same PAAM template to reduce variance; that is, half of a given PAAM template was used for SWTNT synthesis, and the other half was used for MWTNT synthesis. Due to significant bundling and bending of the SWTNT arrays (**Figure #1-1.13a**), it was difficult

to accurately determine the length of the SWTNTs after template dissolution. SWTNT clusters, which were about 20-30 μm in size, were attributed to capillary forces that acted upon the nanotubes after dissolution of the template and drying in air. In contrast, MWTNT arrays maintained the vertically aligned structure imparted by the PAAM template (**Figure #1-1.13b**) with minimal bundling or “hourglass” effects.

The ability to rigidly maintain the ordered structure of the PAAM template after dissolution can be attributed to the thicker outer nanotube walls (80 nm) of the MWTNT arrays which apparently increased the resistance of the nanotubes to bending. Nanotube bundling has been observed in other TiO_2 nanotube synthesis approaches (i.e., electrochemical anodization and template-assisted methods), and this clustering effect has been shown to negatively affect electron transport efficiency and light scattering. In the electrode pictured in **Figure #1-1.13a**, nanotube bundling may also affect electrical contact between the SWTNT nanotube array and nanoparticle paste. Bundling of the SWTNTs caused the nanotubes to curl at the bottom-half of the SWTNT array, which partially detached the nanotubes from the TiO_2 nanoparticle paste. The detachment of SWTNTs from the nanoparticle paste meant less surface area was in contact with the conducting oxide, and electrons injected into the nanotube array might have experienced a longer diffusion path length prior to being collected as a result.

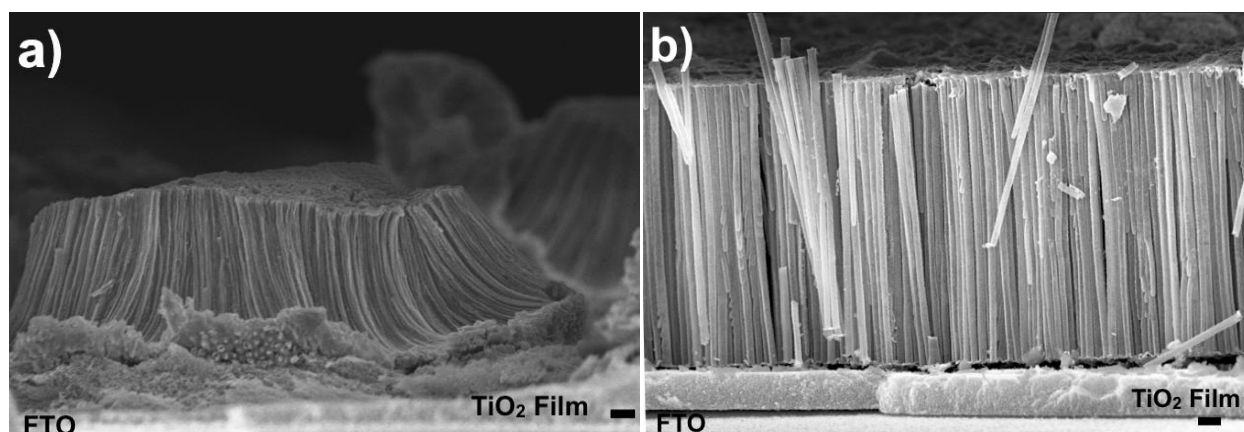


Figure #1-1.13. **a)** SEM images of fracture cross-sections of SWTNT arrays and **b)** MWTNT arrays adhered to fluorine-doped tin oxide (FTO) glass with the aid of a TiO_2 film. All scale bars indicate 1 μm .

The effect of nanotube clustering on electrode morphology was seen in plan view optical and SEM images shown in **Figures #1-1.14a and b** where a significant amount of microcracking and void space was observed between SWTNT bundles. Conversely, MWTNT arrays showed less void space and microcracking due to the improvement structural retainment after the PAAM template had been completely dissolved (**Figures #1-1.14c and d**). From image analyses, $64 \pm 9.6\%$ of the electrode area was covered by SWTNTs, while $80 \pm 3.2\%$ of the electrode area was coated by the MWTNTs. The reduction in nanotube bundling, and the corresponding decrease in void space, influenced the amount of N719 dye (cis-di(thiocyanato-bis(2,2'-bipyridyl-4,4'-dicarboxylato) ruthenium(II) bis(tetrabutylammonium)) adsorbed by the electrodes, as discussed below. Optical micrographs were taken after 24 h incubation in a 0.3 mM N719 solution (in acetonitrile/t-butanol 1:1 vol. ratio) and subsequent integration into

DSSCs (**Figures #1-1.14b inset** and **#1-1.14d inset**)). The images showed that the MWTNT devices possessed a deep, opaque red color, whereas SWTNT devices possessed a lighter red color, and were more translucent. The deep red color observed in MWTNT devices was likely to have been the result of improved dye loading and/or light scattering.

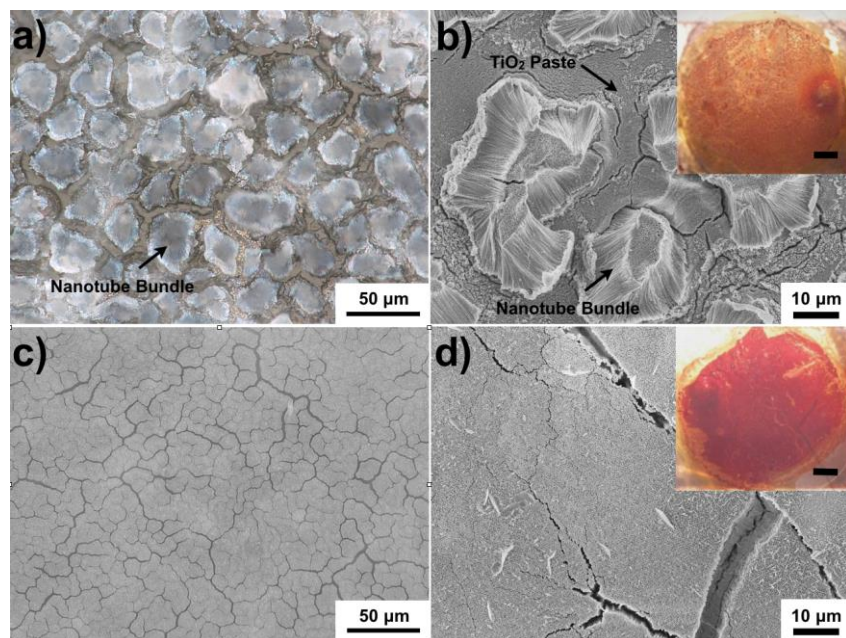


Figure #1-1.14. Representative SWTNT and MWTNT electrodes viewed by optical microscopy **a)**, **c)** and SEM **b)**, **d)**, respectively. Optical images of representative SWTNT (**b)**, inset) and MWTNT (**d)**, inset) after integration into DSSC devices (1 mm scale bars).

Experiments were conducted to determine if the MWTNT architecture had an effect on the amount of N719 dye adsorbed when compared to SWTNT arrays. Five electrodes of each type were incubated for 24 h in 0.3 mM N719 dye solution (in acetonitrile/t-butanol, 1:1 vol. ratio) at room temperature. The dye was subsequently desorbed from the surfaces of the electrode by incubating in 2 mL of 0.1 M NaOH in water/ethanol, 1:1 vol. ratio for 5 mins. The absorbance of desorbed dye in solution was measured by UV-Vis spectroscopy and the N719 dye concentration was obtained by comparison to a calibration curve. The dye concentration was normalized to the active lateral area of the electrode using image analysis software to take into account gaps as small as 6 µm in the nanotube arrays.

The absorbance of the dye in aqueous solution (0.1 M NaOH) was measured by UV-Vis spectroscopy and compared to five solutions of known N719 concentration (5 µM, 10 µM, 15 µM, 20 µM, and 30 µM). The instrument was calibrated on a daily basis with fresh solutions, because N719 degraded over time in aqueous solution. A calibration curve relating absorbance to the molar concentration of N719 dye was determined by linear regression ($R^2 > 0.99$ in both cases), and used to determine the concentration of N719 dye present in solutions used to desorb N719 dye from SWTNT and MWTNT electrodes. Given that 2 mL of solution was used to desorb the N719 dye, the moles of N719 dye desorbed from the electrodes were calculated. Typically, dye desorption is normalized to the mass of TiO₂ on the electrode. In this study, the areal density of TiO₂ was enhanced and surface area was improved by increasing the amount of TiO₂ present. Therefore normalizing on a per unit mass basis could not provide adequate

insight into dye loading, and stronger comparison could be made by normalizing SWTNT and MWTNT electrode dye loading by area. Optical image analyses (Image-J) were used to accurately measure electrode area. More specifically, the optical micrographs taken of each electrode were passed through an image analysis macro that filtered the image based on whiteness using four grayscale thresholds. The area determined at each threshold was averaged to give the electrode area. This program attempted to compensate for the detrimental effect of void space in the electrode, and only take into account area covered by TiO₂ nanotubes.

The average N719 dye loading on five MWTNT electrodes was 195 ± 31 nanomoles N719 per cm², which was 2.2 times greater than for SWTNT arrays prepared by sol-gel infiltration alone (87 ± 28 nanomoles N719 per cm²). This result confirmed that the significant difference in color intensity noted previously was due, in part, to an increase in dye loading. The dye loading ratio (195 : 87) was less than the ratio of estimated roughness factors for MWTNTs and SWTNTs (282 : 73), which may be due to a failure of the roughness factor model to take into account internal porosity within the coating, possible differences in the binding affinity for N719, variability in the nanoparticle paste layer thickness, or inaccessible surface area due to the sol-gel derived nanotube adhering to the wall of the outer nanotube.

To demonstrate the feasibility of aligned MWTNT arrays as working electrodes, and to evaluate the effect of the electrode architecture on DSSC performance, five electrodes of SWTNT and MWTNTs were both fabricated into DSSCs. The current-voltage (*J-V*) behavior of the best-performing MWTNT device (6.5% efficiency) is shown in comparison to the best-performing SWTNT (4.0% efficiency) in **Figure #1-1.15**, and the overall *J-V* characteristics are shown in **Table #1.1.2**. It is also important to note that the worst-performing MWTNT device (4.6%) was still better than best-performing

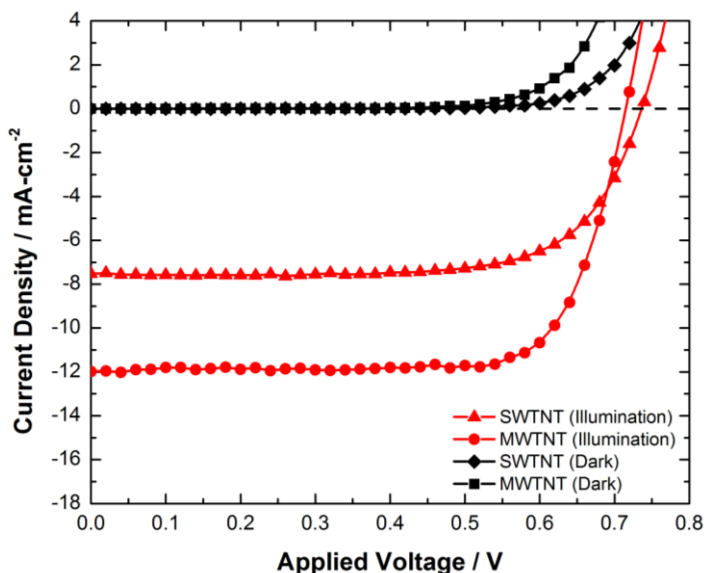


Figure #1-1.15. Current-voltage behavior of the best performing SWTNT and MWTNT devices in the dark (◆, ■) and under AM 1.5 G illumination (▲, ●).

SWTNT device. The 83% improvement in average efficiency was primarily due to the increased average short-circuit current density (by a factor of 1.9). The improvement in short-circuit current density exhibited by MWTNT devices was consistent with the improvement in roughness factor and dye loading.

Table #1.1.2. *Dye-sensitized solar cell J-V characteristics for SWTNT and MWTNT devices at AM 1.5G illumination.^a*

Parameter	SWTNT Devices	MWTNT Devices
J_{sc} (mA cm ⁻²)	5.6 ± 2.0 (3.2-7.6)	10.4 ± 1.2 (9.5-12.0)
V_{oc} (mV)	728 ± 29 (685-763)	710 ± 30 (670-755)
FF	0.714 ± 0.04 (0.66-0.75)	0.714 ± 0.02 (0.71-0.75)
η_{eff} (%)	3.0 ± 1.0 (1.9-4.0)	5.5 ± 0.8 (4.7-6.5)
Dye Adsorption (nmol cm ⁻²)	87 ± 28 (63-130)	195 ± 31 (177-250)

^a Averaged over five devices with the indicated error corresponding to plus-minus one standard deviation, and the values in parentheses correspond to the absolute range.

AFRL/Georgia Tech Interactions:

- J. D. Berrigan worked as an intern within the Durstock group for the full summer of 2009 at AFRL (Wright-Patterson Air Force Base, WPAFB).
- J. D. Berrigan and N. Haase worked as interns with the Johnson group in March and October of 2011 at AFRL (Tyndall Air Force Base, TAFB).
- Taylor McLachlan worked as an intern with the Durstock group in June-July, 2012 and for 2 weeks in 2013 at AFRL/WPAFB.
- Ben deGlee worked as an intern in June-July, 2012 with the Naik and Durstock groups at AFRL/WPAFB.
- Sandhage presented an overview of the BIONIC Center activities in a poster session at the AFRL/RX Bio Review Meeting at Wright-Patterson Air Force Base (Oct. 21, 2009).
- Sandhage presented an overview of BIONIC Center workforce development activities at the Third Persh Conference (on Workforce Development - Meeting Materials Science and Engineering Needs for the 21st Century) in a session entitled "How Does the U.S. Government Better Engage Education," Arlington, VA, Oct. 28, 2010.
- K. H. Sandhage presented a talk on "Bio-Enabled Manufacturing of Nanostructured Materials," at the Nano-Bio Manufacturing Strategic Vision Workshop, TecEdge, Dayton, OH, Sept. 14, 2011.
- Sample exchanges have been conducted with the Durstock and Naik groups for collaborative development of materials for battery and solar cell applications.
- Nanotube and nanorod arrays have been provided to Drummy (AFRL) and Fraser (OSU) for high resolution TEM analyses.
- Sample exchanges have been conducted with G. Strack and H. R. Luckarift in the Johnson group for collaborative development of cathodes for biofuel cells.
- Regular teleconferences have been held with the Durstock, Johnson, Naik, and Fraser groups to discuss and plan collaborative research.
- M. F. Durstock acted as a member of J. D. Berrigan's Ph.D. thesis committee.
- M. F. Durstock is serving as a member of the PhD thesis committee of T. McLachlan.

Manpower Development/Transitions (Former BIONIC Students at AFRL):

- Dr. J. Dan Berrigan joined the AFRL/WPAFB research group of Michael Durstock as a Post-Doctoral Fellow, and has been promoted to the position of staff researcher.
- Dr. Jonathan P. Vernon (an early BIONIC intern) joined the AFRL/WPAFB research group of Tim Bunning as a Post-Doctoral Fellow, and has been promoted to the position of staff researcher.

Publications:

- Y. Fang, Q. Wu, M. B. Dickerson, Y. Cai, S. Shian, J. D. Berrigan, N. Poulsen, N. Kröger, K. H. Sandhage, "Protein-Mediated Layer-by-Layer Syntheses of Free-standing Microscale Titania Structures with Biologically-assembled 3-D Morphologies," *Chem. Mater.*, **21** [24] 5704-5710 (2009).
- S. Shian, K. H. Sandhage, "A Gas-Tight, Cu K α X-ray Transparent Reaction Chamber for High Temperature X-ray Diffraction Analyses of Halide Gas/Solid Reactions," *Rev. Sci. Instr.*, **80**, 115108/1-115108/7 (2009).
- K. H. Sandhage, "Materials 'Alchemy': Shape-preserving Chemical Transformation of Micro-to-Macroscopic 3-D Structures," *JOM*, **62** [6] 32-43 (2010).
- S. Shian, K. H. Sandhage, "Hexagonal and Cubic TiOF₂," *J. Appl. Crystall.*, **43** [4] 757-761 (2010).
- H. Cheun, J. B. Kim, Y. H. Zhou, Y. Fang, A. Dindar, C. Fuentes-Hernandez, J. Shim, K. H. Sandhage, B. Kippelen, "Inverted Polymer Solar Cells with Amorphous Indium Zinc Oxide as Electron Collecting Electrode," *Optics Express*, **18**, A506-A512 (2010).
- J. D. Berrigan, T. S. Kang, Y. Cai, J. R. Deneault, M. F. Durstock, K. H. Sandhage, "Protein-Enabled Layer-by-Layer Syntheses of Aligned, Porous-Wall, High-Aspect-Ratio TiO₂ Nanotube Arrays," *Adv. Funct. Mater.* **21**, 1693-1700 (2011).
- N. R. Haase, S. Shian, K. H. Sandhage, N. Kröger, "Biocatalytic Nanoscale Coatings Through Biomimetic Layer-by-layer Mineralization," *Adv. Funct. Mater.*, **21** (22) 4243-4251 (2011).
- Z. Bao, M.-K. Song, S. Davis, Y. Cai, M. Liu, K. H. Sandhage, "Bio-enabled Syntheses of High Surface Area, Micro/mesoporous C Particles with Selectable 3-D Biogenic Morphologies for Tailored Catalysis, Filtration, or Adsorption," *Energy & Environ. Sci.*, **4** [10] 3980-3984 (2011).
- H. Cheun, J. D. Berrigan, Y. Zhou, M. Fenoll, J. Shim, C. Fuentes-Hernandez, K. H. Sandhage, B. Kippelen, "Roles of Thermally-Induced Vertical Phase Segregation and Crystallization on the Photovoltaic Performance of Bulk Heterojunction Inverted Polymer Solar Cells," *Energy Environ. Sci.*, **4**, 3456-3460 (2011).
- Y. Fang, V. W. Chen, Y. Cai, J. D. Berrigan, S. R. Marder, J. W. Perry, K. H. Sandhage, "Biologically-enabled Syntheses of Freestanding Metallic Structures Possessing Subwavelength Pore Arrays for Extraordinary (Plasmon-Mediated) Infrared Transmission," *Adv. Funct. Mater.*, **22** [12] 2550-2559 (2012). ([Back Cover](#))
- Y. Fang, J. D. Berrigan, Y. Cai, S. R. Marder, K. H. Sandhage, "Syntheses of Nanostructured Cu- and Ni-based Micro-assemblies with Selectable 3-D Hierarchical Biogenic Morphologies," *J. Mater. Chem.*, **22** (4) 1305-1312 (2012). ([Highlighted in Editors' Choice section of the Jan. 20, 2012 edition of Science](#))
- J. P. Vernon, N. Hobbs, A. Lethbridge, P. Vukusic, D. D. Deheyn, K. H. Sandhage, "3-D Photoluminescent Lanthanide-doped Barium Titanate Structures Synthesized by

- Coating and Shape-preserving Reaction of Complex-shaped Bioorganic Templates," *J. Mater. Chem.*, **22** (21) 10435-10437 (2012). (Inside Front Cover)
- D. K. Hwang, C. Fuentes-Hernandez, J. D. Berrigan, Y. Fang, J. Kim, W. J. Potscavage, C. Hyeunseok, K. H. Sandhage, B. Kippelen, "Solvent and Polymer Matrix Effects on TIPS-Pentacene/Polymer Blend Organic Field-Effect Transistors," *J. Mater. Chem.*, **22**, 5531-5537 (2012).
 - H. Cheun, C. Fuentes-Hernandez, Y. Zhou, Y. Fang, Y. Cai, H. Li, A. Sigdel, J. Meyer, J. Maibach, A. Dindar, J. Shim, J. Berry, J.-L. Bredas, A. Kahn, K.H. Sandhage, B. Kippelen, "Oriented Growth of Al₂O₃:ZnO Nanolaminates for Use as Electron-Selective Electrodes in Inverted Polymer Solar Cells," *Adv. Funct. Mater.*, **22** [7] 1531-1538 (2012).
 - R. A. Gittens, R. Olivares-Navarrete, T. McLachlan, Y. Cai, S. L. Hyzy, J. M. Schneider, Z. Schwartz, K. H. Sandhage, B. D. Boyan, "Differential Responses of Osteoblast Lineage Cells to Nanotopographically-Modified, Microroughened Titanium-Aluminum-Vanadium Alloy Surfaces," *Biomater.*, **33** (35) 8986-8994 (2012)..
 - D. W. Lipke, Y. Zhang, Y. Cai, K. H. Sandhage, "Intergranular Tungsten/Zirconium Carbide Nanocomposites via a Selective Liquid/Solid Displacement Reaction," *J. Am. Ceram. Soc.*, **95** [9] 2769-2772 (2012).
 - J. D. Berrigan, T. M. McLachlan, J. R. Denault, Y. Cai, T.-S. Kang, M. F. Durstock, K. H. Sandhage, "Conversion of Porous Anodic Al₂O₃ into Freestanding, Uniformly-aligned, Multi-wall TiO₂ Nanotube Arrays for Electrode Applications," *J. Mater. Chem. A*, **1** (1) 128-134 (2013).
 - R. A. Gittens, R. Olivares-Navarrete, A. Cheng, D. M. Anderson, T. McLachlan, I. Stephan, J. Geis-Gerstorfer, K. H. Sandhage, A. G. Fedorov, F. Rupp, B. D. Boyan, R. Tannenbaum, Z. Schwartz, "The Roles of Titanium Surface Micro/Nanotopography and Wettability on the Differential Response of Human Osteoblast Lineage Cells," *Acta Biomater.*, **9** (35) 6268-6277 (2013).
 - S. C. Davis, V. C. Sheppard, G. Begum, Y. Cai, Y. Fang, J. D. Berrigan, N. Kröger, K. H. Sandhage, "Rapid Flow-through Biocatalysis with High Surface Area, Enzyme-loaded Carbon and Gold-bearing Diatom Frustule Replicas," *Adv. Funct. Mater.*, **23** [36] 4611-4620 (2013).
 - Y. Kim, M. Kathaperumal, O. Smith, M.-J. Pan, Y. Cai, K. H. Sandhage, J. Perry, "High Energy Density Sol-Gel Thin Film based on Neat 2-Cyanoethyltrimethoxysilane," *ACS Appl. Mater. Interf.*, **5** (5) 1544-1547 (2013).
 - V. Singh, T. L. Bougher, A. Weathers, Y. Cai, K. Bi, M. T. Pettes, S. A. McMenamin, W. Lu, D. P. Resler, T. R. Gattuso, D. H. Altman, K. H. Sandhage, L. Shi, A. Henry, B. A. Cola, "High Thermal Conductivity of a Chain-Oriented Amorphous Polythiophene," *Nature Nanotechnol.*, **9** (5) 384-390 (2014).

Presentations (*invited):

- *K. H. Sandhage, "Integration of Biological Self-Assembly with Synthetic Chemical Processing to Yield Functional Nanostructured 3-D Microassemblies," MRS Spring Meeting, San Francisco, CA, April 15, 2009.
- *K. H. Sandhage, S. Shian, Z. Bao, S. Davis, M. R. Weatherspoon, M. B. Dickerson, M. Crne, Y. Fang, Y. Cai, G. Wang, S. C. Jones, S. R. Marder, M. Srinivasarao, "Materials 'Alchemy': Changing the Chemistries, but not Shapes, of 3-D Assemblies," Composites at Lake Louise, Lake Louise, Canada, Oct. 26, 2009.

- *K. H. Sandhage, S. C. Davis, J. P. Vernon, A. S. Gordin, J. D. Berrigan, S. Shian, Y. Fang, Y. Cai, M. B. Dickerson, R. R. Naik, N. Kröger, S. R. Marder, "Integration of Bio-Enabled and Synthetic Syntheses of Functional 3-D Nanostructured Assemblies," CIMTEC 2010 meeting, Montecatini Terme, Italy, June 10, 2010.
- *K. H. Sandhage, "Materials Alchemy: Shape-preserving Chemical Transformation of Macroscopic and Microscopic 3-D Structures," presented to the Glass and Ceramics Department at the University of Erlangen, Erlangen, Germany, Oct. 1, 2010.
- *K. H. Sandhage, "'(Bio)Materials Alchemy': Shape-preserving Chemical Conversion of Intricate 3-D Structures into Sensor, Catalytic, or Optical Materials," presented at the Air Force Institute of Technology for the Air Force Office of Scientific Research Seminar Series, Dayton, OH, Nov. 4, 2010.
- *K. H. Sandhage, "'(Bio)Materials Alchemy': Shape-preserving Chemical Conversion of Intricate 3-D Structures into Sensor, Catalytic, or Optical Materials," presented at the U.S.-Israeli Biotechnology Discussions Workshop, Boston, MA, Dec. 2-3, 2010.
- *Y. Fang, J. P. Vernon, S. Shian, J. D. Berrigan, Y. Cai, N. Poulsen, M. B. Dickerson, N. Kröger, K. H. Sandhage, "Bio-enabled Syntheses of Functional 3-D Nanostructured Materials via Layer-by-Layer Deposition," PacifiChem 2010 (Area 9: Materials and Nanotechnology; Session on "Biological and Bio-Inspired Materials Synthesis and Assembly"), Honolulu, HI, Dec. 15, 2010.
- *Y. Fang, J. P. Vernon, S. Shian, J. D. Berrigan, C. Cameron, Y. Cai, M. B. Dickerson, S. R. Marder, R. R. Naik, N. Kröger, K. H. Sandhage, "Shape-preserving Chemical Conversion of Microscale and Nanostructured 3D Inorganic or Organic Templates into Functional Ceramic or Metallic Structures," Electronic Materials and Applications Conference, Orlando, FL, Jan. 19, 2011.
- *K. H. Sandhage, "Shape-Preserving Chemical Conversion of Self-Assembled Synthetic or Biological 2-D/3-D Templates into Nanostructured Catalytic, Sensor, Optical, or Electronic Materials," Colloquium Talk, University of Albany, Albany, NY, Feb. 4, 2011.
- *K. H. Sandhage, "Materials 'Alchemy': Shape-Preserving Chemical Conversion of 3-D Biogenic or Synthetic Structures into Catalytic, Sensor, Electronic, or Optical Materials," Colloquium Talk, MSE Dept., Boston University, Boston, MA, March 4, 2011.
- *K. H. Sandhage, Y. Fang, J. D. Berrigan, J. P. Vernon, Y. Cai, S. Shian, M. B. Dickerson, T.-S. Kang, J. R. Deneault, R. R. Naik, M. F. Durstock, S. R. Marder, N. Kröger, "Biomolecule-enabled Syntheses of Functional Coatings on Nanostructured Templates," Exploring Biological Interfaces Workshop, San Juan, Puerto Rico, April 3, 2011.
- *J. D. Berrigan, J. P. Vernon, Y. Fang, C. G. Cameron, W. B. Goodwin, S. Shian, Y. Cai, M. B. Dickerson, S. R. Marder, R. R. Naik, N. Kröger, K. H. Sandhage, "Bio-enabled Syntheses of Functional Nanostructured Micro-Assemblies with Intricate Three-Dimensional Morphologies and Tailored Chemistries," 20th International Materials Research Congress, Cancun, Mexico, Aug. 15, 2011.
- *K. H. Sandhage, et al., "Materials Alchemy": Changing the Chemistries, but not Shapes, of 3-D Micro-to-Nanostructured Assemblies," Colloquium talk presented to the School of Materials Science & Engineering, Georgia Tech, Atlanta, GA, Aug. 22, 2011.

- *K. H. Sandhage, "Bio-Enabled Manufacturing of Nanostructured Materials," Nano-Bio Manufacturing Strategic Vision Workshop, Wright Brothers Institute, Dayton, OH, Sept. 14, 2011.
- K. H. Sandhage, "Shape-preserving Chemical Transformation of Macroscopic and Microscopic 3-D Structures via Fluid/Solid Displacement Reactions," 220th Electrochemical Society Meeting, Boston, MA, Oct. 10, 2011.
- K.H. Sandhage, et al., "Changing the Chemistries, but not Shapes, of 3-D Biogenic and Synthetic Assemblies," Materials Design Workshop, Georgia Tech, Atlanta, GA, Oct. 14, 2011.
- J. D. Berrigan, T.-S. Kang, Y. Cai, J. R. Deneault, T. M. McLachlan, R. A. Vaia, M. F. Durstock, K. H. Sandhage, "Protein-Enabled Layer-by-Layer Syntheses of Aligned, Porous-Wall, High-Aspect-Ratio TiO₂ Nanotube Arrays," MRS meeting, Boston, MA, Nov. 29, 2011.
- J. D. Berrigan, T.-S. Kang, J. R. Deneault, T. McLachlan, R. A. Vaia, M. F. Durstock, K. H. Sandhage, "Bio-enabled Synthesis of High-Aspect-Ratio, Porous-Wall Aligned Titania Nanotube Arrays," Fall MRS Meeting, Boston, MA, Nov. 30, 2011.
- *K. H. Sandhage, "Can Rigid, Nanostructured Inorganic or Organic Bioderived Templates with Intricate 3-D Morphologies and Hierarchical Pore Structures be Tailored for Applications in Catalysis, Optics, and Energy Harvesting?" Workshop on "Bio-Inspired Engineering: The Analysis and Design Loop," Harvard University, Cambridge, MA, Jan. 17 2012.
- *K. H. Sandhage, "Bio-Enabled Materials: Synthetic Chemical Tailoring of Complex Biogenic 3-D Structures," Colloquium Talk, Department of Chemistry, North Georgia College and State University, Dahlonega, GA, Jan. 27, 2012.
- *K. H. Sandhage, "(Bio)Materials Alchemy: Shape-Preserving Chemical Conversion of 3-D Biogenic and Synthetic Structures into Catalytic, Sensor, Electronic, and Optical Materials," Colloquium Talk, MSE Dept., Ohio State Univ., Columbus, OH, Feb. 17, 2012.
- Y. Fang, V. W. Chen, Y. Cai, J. D. Berrigan, S. R. Marder, K. H. Sandhage, J. W. Perry, "Extraordinary IR Transmission through Subwavelength Pores in Gold Replicas of *Coscinodiscus asteromphalus* Diatom Frustules," MRS Spring Meeting, San Francisco, CA, April 10, 2012.
- Y. Fang, J. D. Berrigan, Y. Cai, S. R. Marder, K. H. Sandhage, "Syntheses of Nanostructured Cu- and Ni-based Micro-assemblies with Selectable 3-D Hierarchical Biogenic Morphologies," Poster, MRS Spring Meeting, San Francisco, CA, April 10, 2012.
- *K. H. Sandhage, "Bio-Enabled Syntheses of Porous 3-D Hierarchical Assemblies with Tailored Functional Chemistries," MRS Spring Meeting, San Francisco, CA, April 10, 2012.
- *K. H. Sandhage, J. P. Vernon, J. D. Berrigan, S. C. Davis, M. K. Song, Y. Fang, Y. Cai, M. Liu, S. R. Marder, N. Kroger, "Shape-preserving Chemical Transformation of 3-D Biogenic and Synthetic Templates," CIMTEC 2012 Meeting, Montecatini Terme, Italy, June 12, 2012.
- *K. H. Sandhage, "Biomaterials Alchemy," Gordon Research Conference on Biomineralization, Colby-Sawyer College, New London, NH, Aug. 16, 2012.

- K. H. Sandhage, "Functional Protein-Enabled Inorganic/Organic Coatings," Symposium on Advances in Nonwovens, Technical Textiles, and Sustainable Materials, AATCC (Association of Textile, Apparel, and Materials Professionals) Conference, Atlanta, GA, Oct. 11, 2012
- *K. H. Sandhage, "Materials "Alchemy": Chemical Transformation of 3-D Macro-to-Microscale Structures into Replicas Tailored for Catalytic, Optical, Energy, and Aerospace Applications," Colloquium talk presented to the Institute for Electronics and Nanotechnology (Nano@Tech series), Georgia Institute of Technology, Atlanta, GA, Feb. 26, 2013.
- J. D. Berrigan, T. McLachlan, J. R. Deneault, Y. Cai, T.-S. Kang, M. F. Durstock, K. H. Sandhage, "Conversion of Porous Anodic Al₂O₃ into Freestanding, Uniformly-Aligned, Multi-Wall TiO₂ Nanotube Arrays for Electrode Applications," poster presented in the Energy Harvesting, Harnessing, and Storage session of the Symposium on Nanostructured Metal Oxides for Advanced Applications, MRS Spring Meeting, San Francisco, CA, April 4, 2013.
- *K. H. Sandhage, "Bio-Enabled Materials Processing and Scaleup," Institute for Materials Workshop on Biomaterials and Scaling, Global Learning Center, Georgia Institute of Technology, Atlanta, GA, April 15, 2013.
- *K. H. Sandhage, "Bio-Enabled Functional Coatings," Future of Packaging: 2013-2023, Global Learning Center, Georgia Institute of Technology, Atlanta, GA, May 1, 2013.
- *K. H. Sandhage, "Shape-preserving Chemical Conversion Techniques for Electrode Applications," Institute for Materials Workshop on Electrodes for Energy Applications, Global Learning Center, Georgia Institute of Technology, Atlanta, GA, May 6, 2013.
- *K. H. Sandhage, "3-D Highly Porous Structures for Catalysis and Adsorption," Institute for Materials Workshop on Materials and Interfaces for Catalysis, Environment, and Separations, Global Learning Center, Georgia Institute of Technology, Atlanta, GA, May 10, 2013.
- *K. H. Sandhage, "Shape-Preserving Chemical Conversion of 3-D Biogenic and Synthetic Structures into Replicas Tailored for Catalytic, Optical, Energy, and Aerospace Applications," Colloquium talk presented to the School of Physics Science and Engineering, Tongji University, Shanghai, China, July 18, 2013.
- *K. H. Sandhage, "Bio-Enabled 3-D Micro-to-Nanoscale Structures Tailored for Catalytic, Optical, Energy, and Environmental Applications," International Workshop on Bioinspired Engineering, Shanghai Jiao Tong University, Shanghai, China, July 19-21, 2013.
- *K. H. Sandhage, S. C. Davis, J. P. Vernon, Z. Bao, V. C. Sheppard, N. Hobbs, G. Begum, Y. Cai, Y. Fang, J. D. Berrigan, A. Lethbridge, P. Vukusic, D. D. Deheyn, N. Kröger, "Functional (Catalytic, Optical) Inorganic and Inorganic/Organic Structures with Bio-enabled Hierarchical 3-D Morphologies," Symposium on Bio-Inspired Hybrid Materials Synthesis, International Materials Research Congress, Cancun, Mexico, Aug. 11-15, 2013.
- N. Kröger, K. H. Sandhage, N. R. Haase, "Biocatalytic Nanoscale Coatings Through Biomimetic Layer-by-Layer Mineralization," Symposium on Bio-Inspired Hybrid Materials Synthesis, International Materials Research Congress, Cancun, Mexico, Aug. 11-15, 2013.

- M. B. Dickerson, W. Lyon, A. Sierra, W. Grunner, P. Mirau, N. Bedford, M. Jespersen, Y. Fang, K. H. Sandhage, R. R. Naik, "Biomimetic Synthesis of Hybrid Materials with Multi-Modal Antimicrobial Activity," Symposium (D) on the Engineering and Application of Bioinspired Structured Materials, MRS Fall Meeting, Boston, MA, Dec. 3, 2013.
- P. B. Broughton, P. B. Dennis, M. B. Dickerson, K. H. Sandhage, R. R. Naik, "A Titania-based Biocomposite Capable of Multimodal Organophosphate Hydrolysis at Elevated Temperatures," poster presented in Symposium (AA) on the Engineering and Application of Bioinspired Structured Materials, MRS Fall Meeting, Boston, MA, Dec. 3, 2013.
- *K. H. Sandhage, "Changing Chemistry But Not Shape ("Materials Alchemy"), Colloquium talk presented at the School of Mechanical and Biomedical Engineering, National University of Ireland, Galway, Galway, Ireland, Jan. 13, 2014.
- *K. H. Sandhage, "Shape-preserving Chemical Transformation: Materials Alchemy," Materials Science and Engineering Colloquium, Florida State University, Tallahassee, FL, March 19, 2014.
- *K. H. Sandhage, "Conformal Chemical Transformation of Complex 3-D Biogenic and Synthetic Structures: Getting Stoned While Staying in Shape," Colloquium Talk presented as part of the Biomineralization: From Cell Biology to Materials Science Seminar Series, B CUBE, Technical University of Dresden, Dresden, Germany, June 4, 2014.
- K. H. Sandhage, S. C. Davis, W. B. Goodwin, C. G. Cameron, Y. Fang, Y. Cai, I. J. Gomez, J. C. Meredith, "(Bio)Materials Alchemy: Chemical Transformation of Bio-organic and Bio-inorganic 3-D Hierarchical Structures into 3-D Replicas of New (Non-Biogenic) Functional Inorganic Materials," CIMTEC 2014 Meeting, Montecatini Terme, Italy, June 12, 2014.
- *K. H. Sandhage, "Shape-preserving Chemical Transformation of 3-D Biogenic and Synthetic Structures into Functional Inorganic Replicas (or Getting Stoned While Staying in Shape)," Materials Horizons Symposium, Royal Society of Chemistry, Atlanta, GA, July 23, 2014.
- *K. H. Sandhage, "Shape Preserving Chemical Transformation of Three-Dimensional (3-D) Structures: 'Materials Alchemy'," Colloquium Talk presented at the Nanoscale Science and Engineering Center, University of Georgia, Athens, GA, Nov. 14, 2014.

Project IRG #1-2: Syntheses of Light-Harvesting Organic Materials

Georgia Tech Participants: Project PI: Prof. Seth R. Marder; Students: Marcel Said, Fadi Jradi, Rebecca Hill, Jessica Nock, Helen Westbrook, William D. Underwood; Postdocs/Research Scientists: Dr. Stephen Barlow,

AFRL Collaborators: Dr. Michael F. Durstock, Dr. Michael Clark, Dr. Benjamin Leever

Research Goals:

- Development of new organic dyes for use in dye-sensitized solar cells (DSSCs) with increased wavelength range for absorption and absorptivity to give improved light harvesting; increased separation of hole and electron in the dye's excited state to minimize recombination; and improved compatibility with hole-transport materials that can potentially replace liquid electrolytes.

- Development of bulk-heterojunction (BHJ) solar cells using perylene diimides (PDIs) as acceptors. Based on the similarity of their electron affinities to those of fullerenes and on observations of efficient photocharge generation in blends with donor polymers, small-molecule PDIs appear promising acceptors, but photocurrents to date have been low, presumably owing to crystallization of highly anisotropic domains. Our goal was to try and address these limitations by using PDI conjugated polymers (as the only acceptor or in combination with small-molecule PDIs).
- Understanding of the role of trap (gap) states in BHJ cells. Inherent traps originating from the synthesis or material processing can impede charge transport and lead to recombination. Our goal was to investigate the possibility of passivating these states using ‘ultra-low’ addition of molecular dopants without a loss of semi-conductive properties.

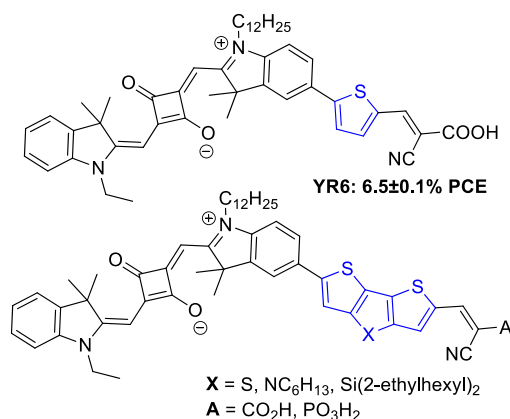
Key Achievements:

- New squaraine-based solar sensitizers for DSSCs developed (collaboration with Graetzel and El Sayed groups) that have advanced the maximum power conversion efficiencies obtained for this class of molecules from 6.3% to 9.6%, making them among the most efficient all-organic sensitizers developed to date
- Multi-technique investigation of the three-component poly(hexylthiophene) / small-molecule PDI / PDI polymer system
- Effects of p-doping in poly(hexylthiophene) and associated BHJ solar cells investigated, revealing effects attributable to disruption of the polymer crystallinity, trap-filling, and contribution of charge carriers.

Approaches and Results:

Squaraine-Based Dyes

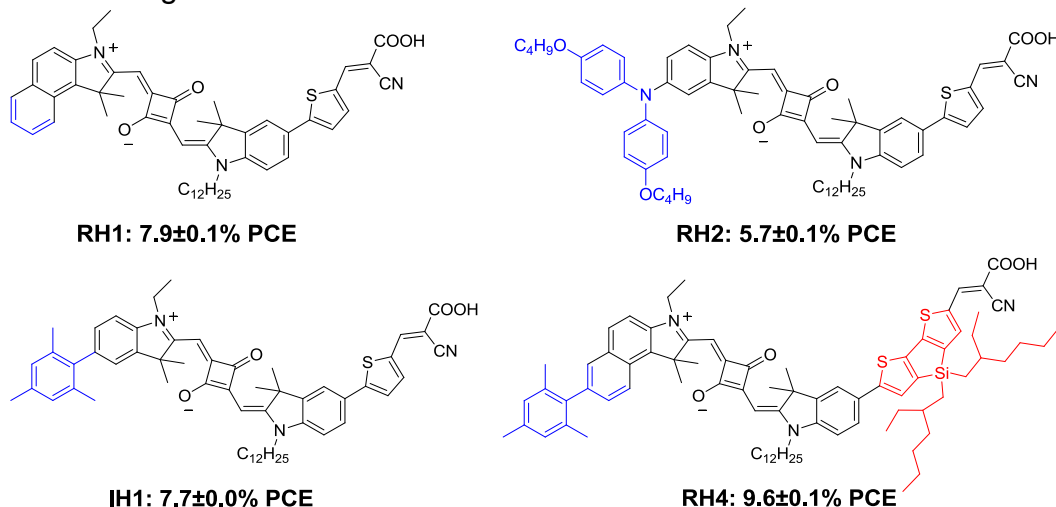
Our main efforts in the area of dye-sensitized solar cells (DSSCs) have concentrated on improving the properties of squaraine type dyes, which we regarded as particularly promising due to their strong light absorption and suitable energetics for photoinduced electron transfer to titania. Before we began work on this project, supported by BIONIC and leveraging NSF and DoE support, the best power conversion efficiency (PCE) reported for a squaraine sensitizer was 6.3%. Among our first family of sensitizers was the top structure (YR6) shown below; collaborators in Graetzel’s group (Lausanne) obtained a PCE of 6.7% for this dye (6.5% in El Sayed group). Subsequently we have synthesized a wide range of related compounds and collaborated with El Sayed’s group (GT) to test these in devices.



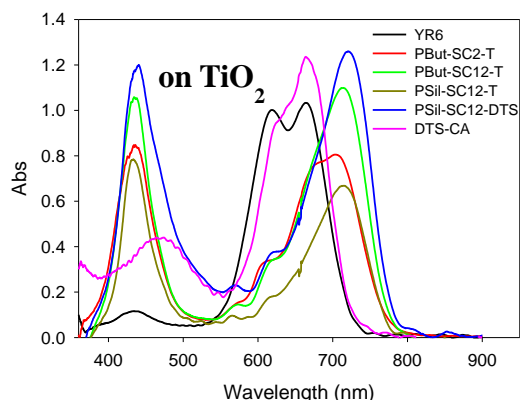
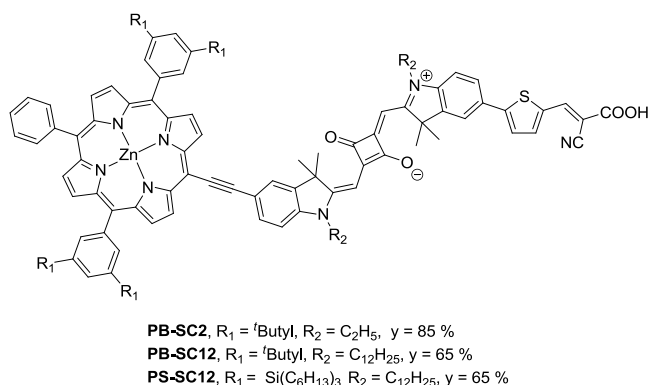
One strategy has been to introduce a more extended conjugated bridge (the lower structure in the Figure to the left, X = S, NC₆H₁₃, Si(2-ethylhexyl)₂) to both red-shift the main low-energy absorption peak, and introduce new absorption bands at higher energy. Examples with X = Si(2-ethylhexyl)₂ exhibit PCEs 8.9%. This high PCE (table below) is mainly due to very high short-circuit current, J_{SC} , which is

19.1% and an elevated open-circuit voltage, V_{OC} , of 0.682 mV (35 mV higher than that for YR6) which was attributed to slower electron recombination rate (9.1 ms compared to 7.5 ms for YR6). Upon changing the anchoring groups from cyanocarboxylic acid to cyanophosphonic acid, a general drop in PCE was observed, which is attributed to a drop in the electron injection efficiency (e.g., 94.6% for a squaraine with a dithienosilole bridge vs. 78.6% for its phosphonic acid counterpart).

We also investigated the effect of modifying the donor group and employing out-of-plane substituents on the “donor end” of the squaraine, opposite that of the anchoring group. In **IH1** (see below), a mesityl group that turns out-of-plane was used to prevent dye to dye interactions and increased both V_{OC} and J_{SC} . By changing the donor from indoline to benzo[*e*]indoline, a 15 nm bathochromic shift and an increased molar extinction coefficient was observed for the **RH1** dye and an increased PCE of 7.9% was obtained. The 5-diphenylamineindoline in **RH2** results in a 41 nm redshift, but the PCE of the resulting devices is only 5.7%, possibly due to the low driving force for dye regeneration. In the dyes **RH3** and **RH4**, combining the benzo[*e*]indoline with the π -bridges of thiophene and di-*n*-hexyl-substituted CPDT resulted in a total 27 nm redshift and an increase in high energy absorption. **RH4** achieved a power conversion efficiency of 9.6%, which is a record efficiency for squaraine dye-DSSCs and is close to 10%, the record PCE for organic sensitizers in DSSCs.

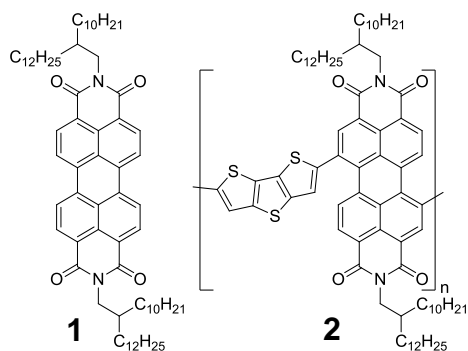


In collaboration with the Anderson group (Oxford University) a series of porphyrin-squaraine dyes have been synthesized (see Figure above); these exhibit panchromatic absorption with very strong ($\epsilon \sim 10^5 \text{ M}^{-1}\text{cm}^{-1}$) absorption bands at both ends of the visible spectrum (also see below). In the best-performing dual chromophore dye, the PCE was increased from 6.7% to 7.6% relative to a squaraine-only analogue mainly due to an increase in J_{SC} attributable to the porphyrin-based absorption band.



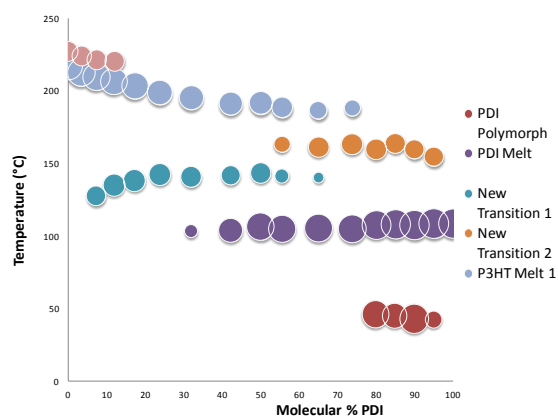
PDI-Materials for Bulk-Heterojunction OPVs

Perylene diimides (PDI)s such as **1** exhibit a number of promising properties for use in place of fullerenes in bulk heterojunction (BHJ) cells; in particular, efficient photoluminescence quenching and charge generation is reported for combinations of **1** and P3HT. We chose **2** as a polymer to investigate as a potential “bridge” between small-molecule PDI domains, or as a potentially as a “surfactant” for the P3HT / PDI blend. This shares the same *N*-substituents as **1** and has the highest electron mobility of PDI polymers to date.



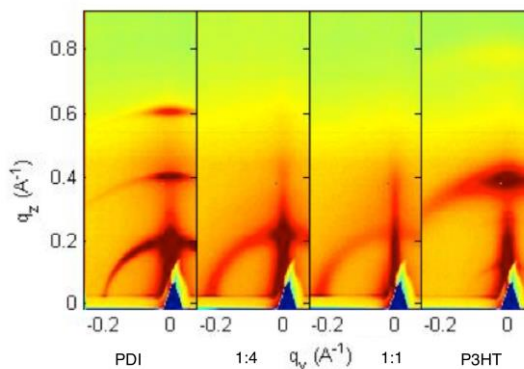
To investigate possible interactions between **2** and P3HT and / or **1**, fluorescence spectra of spin-coated mixed films were examined. When excited at 550 nm, near-complete photoluminescence quenching of the **1** fluorescence was observed when deposited as a BHJ with the polymer. Significant quenching of all emission is observed when P3HT is mixed with the **2**, more so than when P3HT is mixed with **1**. However, quenching of the P3HT/**1** is greatly improved with just a small addition of **2**. These observations support the possibility of energy and electron transfer between these species.

Differential scanning calorimetry for P3HT, **1**, and their mixtures yielded the phase diagram shown at right (size of the data points represents transition enthalpy). The P3HT transition shifts to lower temperatures as the PDI content increases and new peak appears, both being replaced by a second new transition at very high percentages (70-90%) of PDI. For longer heating times, the PDI transition becomes less endothermic and the P3HT melting temperature decreases, indicating the further incorporation of these materials into the new transitions. Additional work involving incorporation of the PPDI into blends of the other materials resulted in the disappearance of the transition peaks, suggesting blending of the crystalline materials with the amorphous polymer.



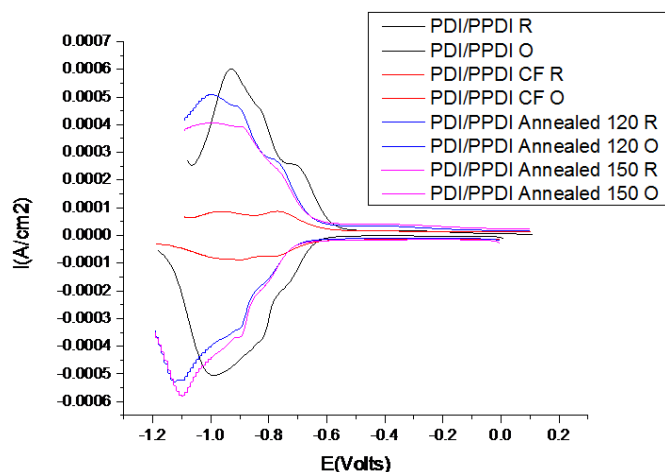
Atomic force microscopy indicated large segregated phases for blends of P3HT and **1** that increase in size with a decrease in the spin rate (i.e., increase in drying time). Upon addition of **2** these phases become more strand-like, with much greater blending, especially at the lowest spin speeds. Further addition of **2** enhances these effects until, for 1:1 wt/wt P3HT / **2** a near-lamellar structure emerges, suggesting that the P3HT has moved to the surface of the film.

WAXS images (right) show only a few features. Upon blending, none of the features associated with neat films are specifically preserved. The 1:1 w/w P3HT / **1** blend has a weak broad peak corresponding to a spacing of 2.66 nm. This spacing increases to 2.85 nm at a 1:4 ratio, and decreases to 2.60 nm with the addition of 5 wt% **2**. The lack of any features assignable to crystalline P3HT is consistent with the decrease in the P3HT melting point in the thermal experiments. Films with higher loadings of **2** exhibited no WAXS peaks.



Neutron reflectivity measurements were taken for a few films, deposited from both chloroform and dichlorobenzene, to determine through-plane composition. In the 1:1:1 ternary blend, switching from chloroform to dichlorobenzene moves the P3HT towards the surface of the film, agreeing with the AFM results.

The effect of **1** on OPV performance was found to depend critically on the source of the P3HT; for Rieke Metals P3HT 4002-E, the presence of **1** resulted in a sudden drop of the open-circuit voltage and the fill factor, and began to adversely affect the current density at more substantial percentages, but for Plexcore P3HT processed in the same way, the short circuit current density jumped to around double the initial value at 5% and 10% addition of **1**, but began to fall drastically again at 25%.



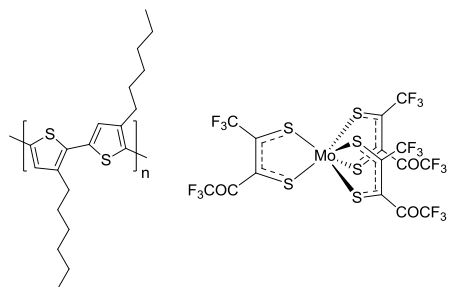
The interactions of **1** and **2** were also studied in the absence of P3HT using AFM, fluorescence, and electrochemistry. In general evidence suggested that annealing led to more homogenous films with better mixing of the two PDI materials. Different degrees of mixing also affect the onset reduction potential of the blended system; When the blended films are annealed, or deposited from chloroform, the onset shifts cathodically by almost 0.1 V. Similar experiments

with the pure films did not yield such shifts. This is consistent with **2** is being diluted into a more homogeneous mixture with **1**, in that the electronic interactions between **2** chains are weakening and, as such, the LUMO is destabilized.

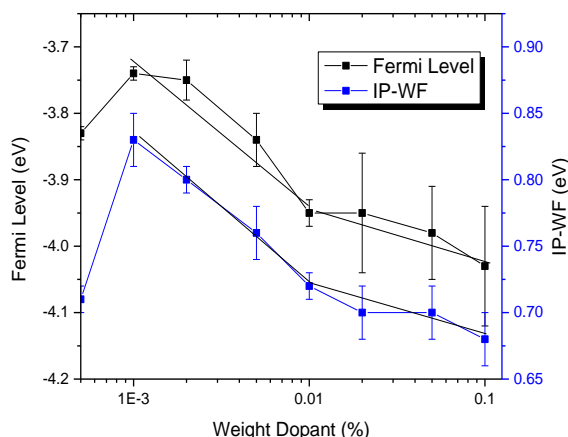
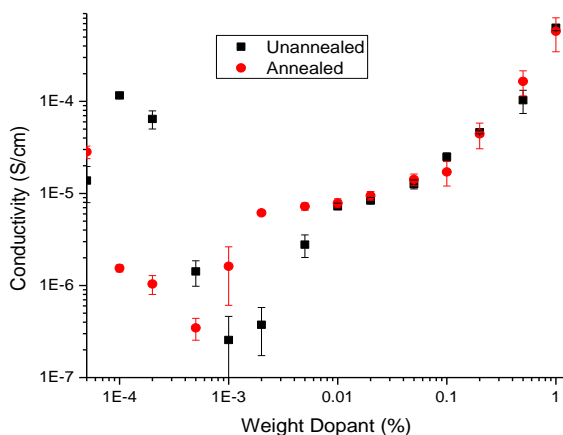
This work provided a wealth of information regarding the P3HT / **1** / **2** system, and three-component BHJ blends in general, but was suspended since we were unable to make significant advances in PDI-based solar cells.

Ultra-low p-Doping of P3HT

Inherent traps originating from the synthesis or material processing can impede charge transport and lead to recombination. We were interested in examining the effects of trap filling using ultra-low levels of molecular p-dopants on BHJ OPV blends. We began our studies with P3HT as a prototypical BHJ donor and $\text{Mo}(\text{tfd-COCF}_3)_3$ (developed in the Marder group, EA ~ 5.5 eV) as the dopant (see structures on right).

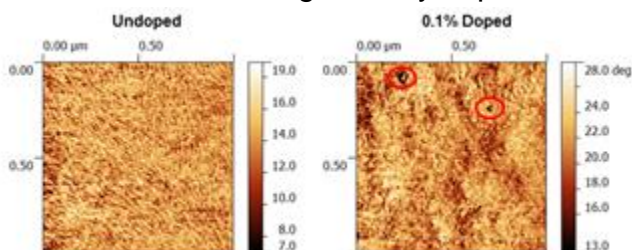


The effect of doping on film conductivity and on the work function determined by UPS (below) suggested the ultra-low doping region where trap-filling is the dominant effect to be 0.001- 0.01 wt% dopant. The initial drop in conductivity at the very lowest concentrations is perhaps to be due to morphological changes.



OPV BHJ cells prepared with low concentrations of dopants gave an initial drop in PCE due to a drop in the fill factor, but as the dopant concentrations approached the ultra-low doping region the current improved. However this improvement did not result in a higher efficiency than the undoped case. Higher doping concentrations resulted in an even greater decrease in FF and PCE due to the appearance of so-called “S-curve” behavior.

WAXS measurements showed that, after annealing, the long-range order of the P3HT lamellar stacking actually improved in films with the lowest dopant concentrations relative to the undoped film. Fitting of the exciton bandwidth of the absorbance conversely indicated a decrease in short-range order.



Furthermore AFM (left) indicated a change in the typical appearance of P3HT films after doping.

In conclusion, molecular dopants can indeed passivate the trap states present in the electronic gap of P3HT, but not without disrupting the order of the film, even at the lowest additions. This disruption leads to lower efficiency OPV cells, despite an improvement observed in the current the ultra-low doping region. Use of dopants in less ordered systems, such as many of the donor-acceptor conjugated polymers now widely used in OPVs, might therefore offer the desired improvement without detrimental effects from morphological disruption; this is currently being pursued in the Marder group.

AFRL/Georgia Tech Interactions:

- 4 visits (for 3-6 weeks) by Marcel Said (graduate student) to WPAFB to collaborate on device fabrication and materials characterization
- X-ray diffraction measurements on polymer / PDI films by Michael Clark at Wright Patterson to complement other structural characterization obtained at GT
- Participation by Benjamin Leever (WPAFB) in Marder group synchrotron X-ray scattering experiments at the Advanced Photon Source at Argonne National Labs
- Participation in IRG-1 monthly phone conferences with AFRL personnel

Manpower Development/Transitions (Former BIONIC Students at AFRL):

None to date

Publications:

- Y. Shi, R. B. M. Hill, J.-H. Yum, A. Dualeh, S. Barlow, M. Grätzel, S. R. Marder, M. K. Nazeeruddin, *Angew. Chem., Int. Ed.*, **50**, 6619-6621 (2011)
- M. Planells, L. Pellejà, J. N. Clifford, M. Pastore, F. De Angelis, N. López, S. R. Marder, E. Palomares, "Energy levels, charge injection, charge recombination and dye regeneration dynamics for donor-acceptor π -conjugated organic dyes in mesoscopic TiO₂ sensitized solar cells," *Energy & Environ. Sci.*, **4**, 1820-1829 (2011).
- C. Huang, S. Barlow, S. R. Marder, "Perylene-3,4,9,10-tetracarboxylic Acid Diimides: Synthesis, Physical Properties, and Use in Organic Electronics," *J. Org. Chem.*, **76**, 2386-2407 (2011).
- J. H. Delcamp, Y. Shi, J.-H. Yum, T. Sajoto, E. Dell'Orto, S. Barlow, M. K. Nazeeruddin, S. R. Marder, M. Grätzel, "The Role of π -Bridges in High-Efficiency DSCs Based on Unsymmetrical Squaraines," *Chem. Eur. J.*, **19**, 1819-1827 (2013)
- F. Jradi, X. Kang, D. O'Neil, G. Pajares, Y. A. Getmanenko, P. Szymanski, T. Parker, M. El-Sayed, S. R. Marder, "Squaraine based dye sensitized solar cells: the effect of π -bridges and anchoring groups on solar cell performance," submitted to *Chem. Mater.*, Dec. 2014.
- R. Hill, X. Kang, I. Davydenko, D. O'Neil, P. Szymanski, T. Parker, M. A. El-Sayed, S. R. Marder. "High efficiency squaraine sensitized solar cells: the effect of extended conjugation and bulky substituents on solar cell performance," in preparation.

Presentations (*invited):

- *S. R. Marder, "Dithienopyrrole-Based Donor-Acceptor Copolymers: Low Band-Gap Materials for Transport and Photovoltaics," Pacific Polymer/DEST-ISL ICOS Conference, Cairns, Australia, Dec., 2009.
- *S. R. Marder, "Applications of Rylene Diimide Containing Materials for Organic Solar Cell Applications," 240th ACS National Meeting, Boston, MA, Aug. 22, 2010.

- *S. R. Marder, "Development of Materials for Organic Electronics and Optoelectronics," Second US-Mexico Meeting "Advances in Polymer Sciences" and XXIV SPM National Congress, Riviera Maya / Cancun, Mexico, Dec. 7, 2011.
- R. Hill, I. Davydenko, F. Jradi, Y.R. Shi, J. Yum, A. Dualeh, S. Barlow, M. Graetzel, S. Marder, M.K. Nazeeruddin, "Extended Asymmetric Squaraine Sensitizers for Dye-Sensitized Solar Cells." Poster presented at the International Conference on Science and Technology of Synthetic Metals 2012 (ICSM 2012), Atlanta, GA, July 8, 2012.
- B. Wunsch, M. Rumi, M. Said, J. Delcamp, Y. R. Shi, J. Yum, A. Dualeh, S. Barlow, M. Graetzel, S. R. Marder, M. K. Nazeeruddin, Poster presented at the International Conference on Science and Technology of Synthetic Metals 2012 (ICSM 2012), Atlanta, GA, July 8, 2012.
- F. M. Jradi, "Asymmetric Squaraine Dyes Exhibiting Panchromatic Absorption for Dye- Sensitized Solar Cells," 64th Southeastern Regional Meeting of the ACS, Raleigh, NC, Nov. 14, 2012.
- R. Hill, I. Davydenko, F. M. Jradi, X. Kang, D. O'Neil, P. Szymanski, T. Parker, S. Barlow, M. El-Sayed, S. Marder, "Donor-Modified Asymmetric Squaraine Sensitizers for Dye Sensitized Solar Cells," 65th Southeastern Regional Meeting of the ACS, Atlanta, GA, Nov. 13, 2013.
- *S. R. Marder, "Interface Modification for Organic Electronics and Optoelectronics," 2014 Gordon Conference on Hybrid Electronic and Photonic Materials, Hong Kong University of Science and Technology, Hong Kong, China, June 22, 2014.
- *S. R. Marder, "The Design, Synthesis, and Characterization of Near-Infrared Absorbing Dyes for Mesoscopic Solar Cells," 9th Aseanian Conference on Dye-Sensitized and Organic Solar Cells (DSC-OPV9), Sydney, Australia, Dec. 8, 2014.

Project IRG #1-3: Modeling, Fabrication, and Testing of Nanostructured Inorganic/Organic Photovoltaic Devices

Georgia Tech Participants: Project PI: Prof. Bernard Kippelen; Students: Alfred Ernst III, James Hsu, William J. Potscavage, Jr.; Post-docs/Research Scientists: Dr. Hyeunseok Cheun, Dr. Canek Fuentes-Hernandez, Dr. Asha Sharma, Dr. Yinhua Zhou

University Collaborators: Prof. Seth Marder, Prof. Ken Sandhage, Dan Berrigan, Dr. Ye Cai, Dr. Yunnan Fang

Research Goals: This project is aimed at fabricating photovoltaic devices that integrate nanostructured metal oxide electron- and hole-selective contacts and electrodes with chemically-tailored interfaces (e.g. titania nanorod/nanotubes arrays, Al₂O₃, ZnO, and nanolaminates of Al₂O₃:ZnO, and IZO) and evaluating their electrical and photovoltaic performance.

Key Achievements:

- (2009-2011) The Kippelen and Sandhage groups studied the structural, electrical, and optical properties of (Al₂O₃)_x:(ZnO)_y nanolaminates deposited by atomic layer deposition. An increase of the electrical conductivity of (Al₂O₃)_x:(ZnO)_y nanolaminates compared with ZnO films was attributed to a combination of morphological changes, doping, and quantum confinement effects. Inverted polymer-based solar cells using such films as electron-collecting electrodes were fabricated and yielded power conversion efficiency of 3 % under simulated AM 1.5G, 100 mW/cm² illumination.

- (2009-2011) The Kippelen and Sandhage groups studied the roles of thermally-induced vertical phase segregation and crystallization on the photovoltaic performance of bulk heterojunction inverted polymer solar cells. The photoactive layers were comprised of poly(3-hexylthiophene) (P3HT) and [6,6]-phenyl C61 butyric acid methyl ester (PCBM) blends deposited on an ITO electrode modified with ZnO. Depth profiling X-ray photoelectron spectroscopy (XPS) experiments showed that annealing leads to a vertical phase segregation where P3HT-rich regions are adjacent to the bottom ZnO layer used as an electron-collecting electrode. X-ray diffraction experiments showed that improvements in the photovoltaic performance upon annealing could be attributed to a higher crystallinity of the P3HT polymer. The main conclusion of this study was that vertical phase segregation does not seem to play a significant role on the cell performance, against conventional wisdom and previous reports.
- (2011-2012) The Kippelen group investigated the use of new flexible optically transparent substrates based on paper and nanofibrillated cellulose (NFC) films. The motivation of this work was to find replacements for the conventional synthetic polymeric substrates derived from conventional fossil-fuel-based chemistry, and find new solutions that are environmentally more friendly. The NFC films were provided by the teams of Jeffrey Youngblood and Robert Moon at Purdue University. Organic photovoltaic devices with a structure Glass/NFC films/Ag (150 nm)/P3HT:ICBA (190 nm)/MoO₃ (15 nm)/Ag (20 nm) were successfully fabricated and yielded operating devices with power conversion efficiencies of 1.3%. Atomic force microscopy revealed that the average RMS roughness of the optically transparent NFC films was 1.9 nm to be compared with 4 nm for regular ITO substrates.

Approaches and Results:

- (Al₂O₃)_x:(ZnO)_y nanolaminates were fabricated by atomic layer deposition (ALD) and used as electron-collecting electrodes in organic solar cells. In this work, the Kippelen and the Sandhage groups studied the structural, electrical, and optical properties of these nanolaminates as a function of the relative values of x and y . 300-nm-thick (Al₂O₃)₁:(ZnO)₂₀ nano-laminates showed a high optical transmittance ($\geq 80\%$) in the visible region with a low resistivity of $4.5 \times 10^{-4} \Omega\text{-cm}$ and a low work function (4.2 eV). An increase of the electrical conductivity of these (Al₂O₃)_x:(ZnO)_y nanolaminates compared with neat ZnO films fabricated by ALD was attributed to a combination of morphological changes, doping, and quantum confinement effects. These electrodes were found to perform well in P3HT:PCBM polymer-based inverted solar cells and yielded power conversion efficiency values of 3 % under simulated AM 1.5G, 100 mW/cm² illumination. The work was published in the journal *Advanced Functional Materials*.
- Brief 160 °C annealing treatments dramatically enhanced the performance of bulk heterojunction inverted polymer solar cells with an ITO/ZnO/P3HT:PCBM/MoO₃/Ag structure. The influence of such treatments on cell performance has been correlated to vertical phase segregation and crystallization within the photoactive layer of such cells. The photoactive layer, comprised of a mixture of P3HT and PCBM deposited on ZnO, was annealed for 10–30 min at 160 °C. Depth profiling with X-ray photoelectron spectroscopy (XPS) revealed that such annealing resulted in enrichment of the P3HT concentration near the ZnO layer, particularly after 20 and 30 min of annealing.

Crystallization of P3HT was detected by X-ray diffraction (XRD) analyses after 10 to 30 min of such annealing, with little difference in the extent of crystallization detected over this time frame. It was found that vertical segregation does not seem to play a role as significant as that of crystallization on cell performance. The work was published in the journal *Energy and Environmental Science*.

AFRL/Georgia Tech Interactions:

The Kippelen group has numerous interactions with the Marder and Sandhage groups at Georgia Tech. The Marder group provided some of the photoactive materials. Collaborations between the Kippelen and Sandhage groups included the photovoltaic characterization of dye sensitized solar cells fabricated in the Sandhage group in the Kippelen group, structural characterization of metal oxide films and nanolaminates of $\text{Al}_2\text{O}_3/\text{ZnO}$ using X-ray and TEM experiments, and the characterization of concentration profiles in polymer bulk heterojunctions photoactive layers (P3HT:PCBM) using depth profiling XPS. The Kippelen group participates in regular conference calls with the team of Mike Durstock at AFRL with the Marder and Sandhage groups.

Publications:

- H. Cheun, J. B. Kim, Y. H. Zhou, Y. Fang, A. Dindar, C. Fuentes-Hernandez, J. Shim, K. H. Sandhage, B. Kippelen, "Inverted Polymer Solar Cells with Amorphous Indium Zinc Oxide as Electron Collecting Electrode," *Optics Express*, **18**, A506-A512 (2010).
- Y. Zhou, H. Cheun, W. J. Potscavage Jr., C. Fuentes-Hernandez, S.-J. Kim, B. Kippelen, "Inverted Organic Solar Cells with ITO Electrodes Modified with an Ultrathin Al_2O_3 Buffer Layer Deposited by Atomic Layer Deposition," *J. Mater. Chem.*, **20**, 6189-6194 (2010).
- H. Cheun, C. Fuentes-Hernandez, Y. Zhou, W. J. Potscavage, S.-J. Kim, J. Shim, A. Dindar, B. Kippelen, "Electrical and Optical Properties of ZnO Processed by Atomic Layer Deposition in Inverted Polymer Solar Cells," *J. Phys. Chem.*, **114**, 20713-20718 (2010).
- Y. Zhou, H. Cheun, S. Choi, W. J. Potscavage Jr., C. Fuentes-Hernandez, B. Kippelen, "Indium Tin Oxide-free and Metal-free Semitransparent Organic Solar Cells," *Appl. Phys. Lett.*, **97**, 153304/1-153304/3 (2010).
- Y. Zhou, H. S. Cheun, S. Choi, C. Fuentes-Hernandez, B. Kippelen, "Optimization of a Polymer Top Electrode for Inverted Semitransparent Organic Solar Cells," *Org. Electron.*, **12**, 827-831 (2011).
- H. Cheun, J. D. Berrigan, Y. Zhou, M. Fenoll, J. Shim, C. Fuentes-Hernandez, K. H. Sandhage, B. Kippelen, "Roles of Thermally-induced Vertical Phase Segregation and Crystallization on the Photovoltaic Performance of Bulk Heterojunction Inverted Polymer Solar Cells," *Energy & Environ. Sci.*, **4**, 3456-3460 (2011).
- D. K. Hwang, C. Fuentes-Hernandez, J. D. Berrigan, Y. Fang, J. Kim, W. J. Potscavage Jr., K. H. Sandhage, B. Kippelen, "Solvent and Polymer Matrix Effects on TIPS-Pentacene/Polymer Blend Organic Field-effect Transistors," *J. Mater. Chem.*, **22**, 5531-5537 (2012).
- H. Cheun, C. Fuentes-Hernandez, Y. Zhou, Y. Fang, Y. Cai, H. Li, A. Sigdel, J. Meyer, J. Maibach, A. Dindar, J. Shim, J. Berry, J.-L. Bredas, A. Kahn, K. H. Sandhage, B. Kippelen, "Oriented Growth of $\text{Al}_2\text{O}_3/\text{ZnO}$ nanolaminates for use as Electron-Selective Electrodes in Inverted Polymer Solar Cells," *Adv. Funct. Mater.*, **22**, 1531-1538 (2012).

Presentations (*invited):

- S. Choi, W.J. Potscavage Jr., B. Kippelen, "Area-Scaling of the Performance of Organic Solar Cells," MRS Fall Meeting, Boston, MA, Dec., 2009.
- *B. Kippelen, "Organic Photovoltaics," presented at the Energy Forum for Energy and the Environment, Georgia Institute of Technology, Atlanta, GA, Feb. 11, 2010.
- *B. Kippelen, "Tailoring Interfaces in Organic and Printed Electronics," presented at the 9th North American Organic Electronics Association (OE-A) Working Group Meeting, Atlanta, GA, March 5, 2010.
- *B. Kippelen, "Organic Photonics and Electronics: Myth or Reality?," Plenary talk presented at the SPIE Photonics Europe, Brussels, Belgium, April 12, 2010.
- Y.H. Zhou, H. Cheun, W.J. Potscavage Jr., C. Fuentes-Hernandez, S.-J. Kim, B. Kippelen, "Efficient Inverted Polymer Solar Cells Using an Ultrathin Aluminum Oxide Buffer Layer Deposited by Atomic Layer Deposition," presented at the International Symposium on Functional-pi-Electron Systems, Atlanta, GA, May 23, 2010.
- Y. H. Zhou, H. Cheun, W. J. Potscavage Jr., B. Kippelen, "Metal-Free Inverted Hybrid Organic Solar Cells," presented at SPIE, San Diego, CA, Aug. 1, 2010.
- B. Kippelen, S. Choi, W. J. Potscavage Jr. (invited), "Modeling of Large-Area Organic Solar Cells," 10th International Conference on Numerical Simulation of Optoelectronic Devices, Atlanta, GA, Sept. 6, 2010.
- *B. Kippelen, "Organic Photovoltaics: Status and Promise," presented to the Department of Materials Science, University of Florida, Gainesville, FL, Sep. 14, 2010.
- *B. Kippelen, "Interfaces in Organic Photovoltaics," presented at the conference on Sustainable Energy Future: Focus on Organic Photovoltaics, Oak Ridge National Laboratories (ORNL), Knoxville, TN, Sep. 15, 2010.
- *B. Kippelen, "Organic Photovoltaics: A Myth or Reality?," presented to the School of ECE, Seminar Series, Georgia Institute of Technology, Atlanta, GA, Sep. 22, 2010.
- B. Kippelen, X. H. Zhang, S.P. Tiwari, J.B. Kim, T. Sajoto, S. Barlow, S.R. Marder, D.K. Huang, C. Fuentes-Hernandez, "Recent Advances in Organic and Hybrid Transistors for Display Backplane Technology and Complementary Digital Circuits," presented at the 8th International Conference on Electroluminescence and Organic Electronics, Ann Arbor, MI, Oct. 17, 2010.
- *B. Kippelen, "Organic Semiconductors for Photovoltaic and Light-Emitting Devices: Status and Promise," Frontiers in Optics (FiO) Conference, Rochester, NY, Oct. 24, 2010.
- *B. Kippelen, "Tailoring Interfaces in Organic Photovoltaic Devices," ACS 241st National Meeting and Exposition, Solar Energy Conversion and Utilization for Fuels and Energy Production, Anaheim, CA, March 27, 2011.
- *B. Kippelen, "Interfaces in Organic Photovoltaic Devices," 2011 Glass and Optical Materials Division Annual Meeting, Savannah, GA, May 15, 2011.
- *B. Kippelen, "The Future of Plastic Optoelectronics," IEEE Technology Time Machine Conference, Hong Kong, June 3, 2011.
- *B. Kippelen, "The Future of Organic Photovoltaics: Controlling Interfaces with Solution Processible Materials," Plenary talk presented at the Sun Energy Conference and Exhibition (SuNEC 2010), Sicily, Italy, July 5-7 (2011).

- H. Cheun, J. Shim, H. Li, Y.H. Zhou, Y. Fang, Y. Cai, C. Fuentes-Hernandez, K. H. Sandhage, J. L. Bredas, B. Kippelen, "Al₂O₃:ZnO nanolaminates as electron-collecting electrodes in inverted polymer solar cells," Optics and Photonics, SPIE annual meeting, San Diego, CA, Aug. 21, 2011.
- H. Cheun, J. D. Berrigan, Y. Zhou, M. Fenoll, J. Shim, C. Fuentes-Hernandez, K. H. Sandhage, B. Kippelen, "Roles of Thermally Induced Vertical Phase Segregation and Crystallization on the Photovoltaic Performance of Bulk Heterojunction Inverted Polymer Solar Cells," Optics and Photonics, SPIE annual meeting, San Diego, CA, Aug. 21, 2011.
- Y. H. Zhou, J. Shim, H. Cheun, A. Dindar, C. Fuentes-Hernandez, J. Meyer, A. Kahn, B. Kippelen, "Inverted Organic Solar Cells Using a Water-soluble Polymer Modified Indium Tin Oxide as an Electron-collecting Electrode," Optics and Photonics, SPIE annual meeting, San Diego, CA, Aug. 21, 2011.
- B. Kippelen, "Organic Photovoltaics: Fundamentals and Applications," School of Soft Matter Research of the Freiburg Institute for Advanced Studies, Photosensitive Processed in Nature and Technology, Anacapri, Capri Island, Italy, Sep. 19, 2011.
- *B. Kippelen, "Controlling Interfaces in Organic Photovoltaics: Towards All Polymeric Solar Cells," Organic Photovoltaics 2011, Philadelphia, PA, Sept. 20, 2011.
- *B. Kippelen, "Interface Engineering in Organic Photovoltaics: Towards All Polymeric Devices," Plastics in Photovoltaics 2011, Philadelphia, PA, Sept. 20, 2011.
- *B. Kippelen, "Organic Photovoltaics: Clean Energy for the 21st Century," Plenary talk presented at the IEEE International Conference on Smart Grid and Clean Energy Technologies, Chengdu, China, Sept. 27, 2011.
- *B. Kippelen, "Organic Photovoltaics: Novel Device Architectures," International Workshop on Nano and Bio-Photonics, St. Germain au Mont d'Or, France, Oct. 23, 2011.
- *B. Kippelen, "Carbon-based Optoelectronics," French-US Symposium: Graphene, Taking Electronics Beyond Silicon," Atlanta, GA, Oct. 28, 2011.
- *B. Kippelen, "Physics of Organic Semiconductors: Towards Flexible Optoelectronics," Composites at Lake Louise, Fairmont Chateau Lake Louise Hotel, Alberta, Canada, Oct. 29, 2011.
- *B. Kippelen, "Organic semiconductors: toward flexible optoelectronics," Colloquium talk presented at the School of ECE Seminar Series, Georgia Institute of Technology, Atlanta, GA, Nov. 9, 2011.
- *B. Kippelen, "The Role of ALD in Printed Electronics," Cambridge Nanotech User Group Meeting, Atlanta, GA, Nov. 13, 2011.
- *B. Kippelen, "Interface Science and Engineering of Organic Solar Cells," Materials Research Society Annual Fall Meeting, Boston, MA, Nov. 28, 2011.
- *B. Kippelen, "Organic Semiconductors: Toward Flexible Optoelectronics," Colloquium talk presented to the School of ECE Seminar Series, Georgia Institute of Technology, Atlanta, GA, Feb. 15, 2012.
- *B. Kippelen "Interface Modification in Organic Photovoltaic Devices," Smart Coatings 2012, Orlando, FL, Feb. 22, 2012.
- *B. Kippelen, "Advances in Printed Organic Electronics Through Interface Modification," Colloquium talk presented to the Princeton Institute for the Science and

Technology of Materials & Princeton Center for Complex Materials, Spring 2012 Seminar Series, Princeton, NJ, March 14, 2012.

Seed Grant #1: Rational Engineering of Semiconductor Nanowires and Superstructures for Advanced Photon Harvesting (2010-2012)

Georgia Tech Participants: Project PI: Prof. Michael A. Filler; Students: Naechul Shin, Ildar Musin

University Collaborators: Prof. Kenneth H. Sandhage

AFRL Collaborators: WPAFB: Dr. Michael F. Durstock

Research Goal:

- To understand the role of surface chemistry during semiconductor nanowire synthesis and to use this information to rationally fabricate superstructured materials for applications in solar cells.

Key Achievements:

- Demonstrated that surface hydrogen is responsible for changes to nanowire growth direction and created kinking superstructures.
- Rationally controlled sidewall deposition by incorporating “molecular resists” that selectively terminate sidewall facets during growth.
- Fabricated diameter-modulated superstructures with user-defined periodicities.
- Controlled nanowire elongation rate by in-situ alloying of the growth catalyst.

Approaches and Results:

Nanoscale inorganic crystals offer exciting new opportunities to reduce the cost and increase the efficiency of photovoltaic technologies. 1-D semiconductor nanowires are a quintessential class of these materials and the vapor-liquid-solid technique – where a liquid droplet collects semiconductor atoms from the vapor and directs the crystallization of each solid layer – is a workhorse synthesis method. The placement of multiple functionalities along the nanowire length, via user-defined changes to carrier density, alloy composition, heterostructure, etc., is a key feature of VLS synthesis. Such nanoscale encoding is possible by delivering precursors, either concurrently or sequentially, containing a variety of semiconductor and/or dopant atoms. Unfortunately, major synthetic challenges, stemming from an inadequate understanding of key mechanistic details and the use of chemistries originally developed for 2-D films, prevent robust programming of nanowire structure and severely restrict the accessible property space.

The PI and his team used *in situ* infrared spectroscopy to show the influence of solid-vapor interface chemistry on nanowire growth. For the Si/Au (nanowire/catalyst) system, high hydrogen coverage modifies the force balance at the trijunction (i.e., where the vapor, liquid, and solid intersect) and drives a transition from <111> to <112> oriented growth [1]. A wealth of reports corroborate this structural motif, often referred to as “kinking,” but this work identified the basic role of surface chemical bonding and provided a previously absent mechanism. The delivery of alternative surface species (e.g., $-\text{CH}_3$) was also found to influence nanowire crystal growth direction.

For example, the addition of methylgermane to the conventional Ge nanowire synthesis environment (i.e., GeH_4/H_2) led to $\langle 110 \rangle$ oriented Ge nanowires. As shown in **Figure #S-1.1**, cyclically varying methylgermane flow enables “kinking superstructures” – multiple, user-programmable changes to growth orientation – comprised of $\langle 111 \rangle$ or $\langle 110 \rangle$ segments [2]. The modulation of gas phase composition, as opposed to global parameters such as temperature or total pressure, allowed specific processes (i.e., sidewall chemistry) to be targeted independently of other process (e.g., droplet supersaturation).

The PI’s team showed how “molecular resists” – species that adsorb on the nanowire sidewall and block deposition – can control taper and enable diameter-modulated superstructures. Nanowires with modulated diameters promise a route to selectively scatter different portions of the solar spectrum, greatly expanding opportunities for light trapping. In general, weak hydride bonds (e.g., Ge-H) lead to facile H_2 desorption from the nanowire sidewall. Rather than decomposition of growth precursors only at the catalyst, H_2 desorption opens surface sites such that semiconductor atoms can also deposit along the sidewall. This process results in marked sidewall tapering. In a separate project, the PI showed that tapering can be eliminated by increasing the coverage of surface hydrogen atoms, which can be accomplished by raising the partial pressure of GeH_4 (i.e., increasing the H delivery rate) and/or lowering the substrate temperature (i.e., reducing the H_2 desorption rate).

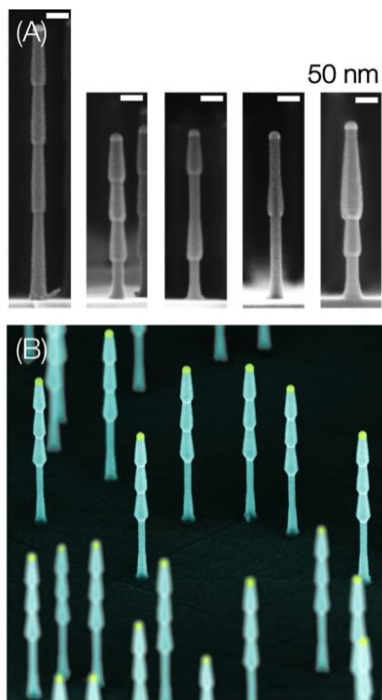


Figure #S-1.2 a) User-defined diameter-modulated superstructures, b) arrays fabricated with TMT.

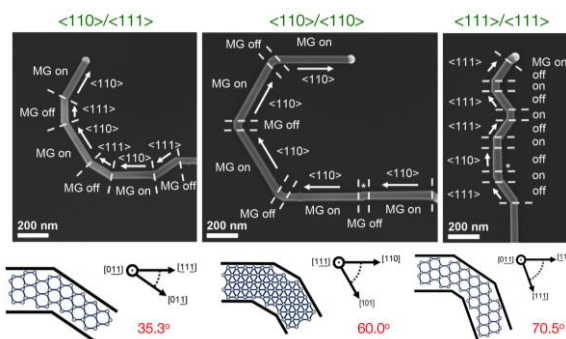


Fig. #S-1.1. Example of a diameter-modulated Ge nanowire superstructures fabricated via modulating methylgermane flow.

While diameter modulation should be possible by allowing sidewall deposition for a specified time and then changing process conditions (i.e., T and/or P) such that it ceases, hydrogen atoms are a fickle adsorbate – easily desorbing upon raising the substrate temperature or removing the process gas. This behavior leads to additional deposition on previously grown segments. To this end, the PI’s team developed a toolkit of precursor chemistries to more robustly terminate the nanowire sidewall. For example, the addition of tetramethyltin (TMT) during Ge nanowire growth blocks tapering at conditions above the H_2 desorption temperature ($\sim 300^\circ\text{C}$).

Figure #S-1.2a shows that user-definable diameter-modulated nanowires were achievable by modulating TMT partial pressure. Termination of TMT flow reinitiates radial deposition only on newly formed portions of the

nanowire, but the stability of the previously created surface layer “locks-in” the diameter on lower sections. Diameter changes exceeding 100% were achieved. **Figure #S-1.2b** confirms that excellent uniformity is possible across large substrate areas [3].

TMT simultaneously delivers (1) species to the sidewall which control radial deposition and (2) Sn atoms to the catalyst which reduces growth rate. In the ideal situation, these two effects would be independently controllable. The addition of triethylsilane (TES) provided an alternative method to control taper without impacting growth rate. Surface-bound ethyl species, likely resulting from TES decomposition, exhibit a non-zero yet short surface lifetime such that the degree of taper could be tuned simply with TES flow rate. Methylsilane provides more stable surface termination, akin to TMT, but without catalyst alloying nor changes to growth rate.

Publications:

- N. Shin, M. A. Filler, “Controlling Silicon Nanowire Growth Direction Via Surface Chemistry,” *Nano Lett.*, **12**, 2865 (2012).
- R. Musin, M. A. Filler, “Chemical Control of Semiconductor Nanowire Kinking and Superstructure,” *Nano Lett.*, **12**, 3363 (2012).
- R. Musin, D. S. Boyuk, M. A. Filler, “Surface Chemistry Controlled Diameter-Modulated Semiconductor Nanowire Superstructures,” *J. Vac. Sci. Technol. B*, **31** 020603 (2013).

Presentations (*invited):

- N. Shin, S. V. Sivaram, M. A. Filler, “In-situ Spectroscopy Investigation of Hydrogen on Si Nanowires,” Annual Meeting of the American Institute of Chemical Engineers, Salt Lake City, UT, Nov. 8-12, 2010.
- *M. A. Filler et al, “Precision Engineering of Nanowire Structure and Function,” Georgia Institute of Technology, Center for Organic Photonics and Electronics, Atlanta, GA, March 4, 2011.
- N. Shin, S. V. Sivaram, M. A. Filler, “An In-situ Chemical Study of the Influence of Hydrogen on Si Nanowire Crystal Orientation, Catalyst Diffusion, and Faceting,” Materials Research Society Spring Meeting, San Francisco, CA, April 25, 2011.
- I. Musin, M. A. Filler, “Synthesis of Single-crystal, Defect-free Group IV Alloy Nanowires with Large Carbon Concentrations,” Materials Research Society Spring Meeting, San Francisco, CA, April 25, 2011.
- *M. A. Filler, et al., “Precision Engineering of Semiconductor Nanowires,” Air Force Research Laboratory, Materials and Manufacturing Directorate, Dayton, OH, June 3, 2011.
- I. R. Musin, N. Shin, S. V. Sivaram, M. A. Filler, “Crystal Structure Engineering of Semiconductor Nanowires,” Annual Meeting of the American Institute of Chemical Engineers, Minneapolis, MN Oct. 17, 2011.
- *M. A. Filler, et al., “Precision Engineering of Semiconductor Nanowires for Advanced Photovoltaic Devices,” 58th International Symposium of the American Vacuum Society, Nashville, TN, Oct. 30, 2011.
- I. R. Musin, M. A. Filler, “Crystal Structure Engineering of Ge Nanowires,” 58th International Symposium of the American Vacuum Society, Nashville, TN, Oct. 30, 2011.

- *M. A. Filler, et al., "Rational Engineering of Nanowire Crystal Structure and Superstructure," Clemson University, Department of Chemical and Biomolecular Engineering, Clemson, SC, Dec. 1, 2011.
- *M. A. Filler, et al., "Rational Engineering of Nanowire Crystal Structure and Superstructure," University of New Mexico, Department of Chemical and Nuclear Engineering, Albuquerque, NM, Jan. 24, 2012.
- *M. A. Filler, et al., "Rational Engineering of Nanowire Crystal Structure and Superstructure," University of Georgia, Nanoscale Science and Engineering Center (NanoSEC), Athens, GA, Feb. 24, 2012.
- *M.A. Filler, et al., "Expanding the Semiconductor Nanowire Design Space," Georgia Institute of Technology, Nano@Tech, Aug. 28, 2012.
- *M. A. Filler, et al., "Expanding the Semiconductor Nanowire Design Space," Materials Research Society Fall Meeting, Boston, MA, Nov. 25, 2012.
- I. R. Musin, D. S. Boyuk, S. Chan, M. A. Filler, "Diameter-Modulated Semiconductor Nanowire Superstructures," Materials Research Society Fall Meeting, Boston, MA, Nov. 25, 2012.

Seed Grant #2: Panning for DNA Aptamer Sequences for Nano-sized Gold Particles

Georgia Tech Participants: Project PI: Prof. Valeria T. Milam; Students: Maeling Nicole Tapp, Richard S. Sullivan

AFRL Collaborators: WPAFB: Dr. Rajesh R. Naik, Dr. Patrick Dennis

Research Goals:

- Identify aptamers using a novel competition-based screening approach that avoids the sequence bias, PCR-based amplification errors, and labor intensive approach reported in the literature
- Implement this novel competition-based screening approach to identify face-specific and/or shape DNA sequences that bind in a strong, but noncovalent manner to a variety of gold-based targets

Key Achievements:

- Completed studies to evaluate the effect of incubating various nucleotide-based products with aging Au seed. We evaluated the effects using UV-Vis spectroscopy as well as select samples for TEM analysis. We investigated incubating aging Au seed with homopolymers of (A, C, G, T), mixtures of homopolymers, specific thymine and adenine-rich sequences (single-stranded and double-stranded); dNTPs, NTPs, dNMPs and a dNTP mix. Timepoints were taken at 2 hours and 7 days for UV-vis spectroscopy. Select incubation conditions were evaluated in a kinetics study to monitor shifts in plasmonic signatures over time.
- Optimized a solution Polymerase Chain Reaction (PCR)-based amplification and enzyme-based digestion of hybridization partners to prepare large sequence libraries of random, single-stranded DNA with negligible (i.e. undetectable) amounts of undesired side-products (e.g. partially elongated DNA duplexes).
- Optimized an emulsion PCR-based amplification of large sequence libraries that may enable easier incorporation of other template sequence (e.g. shorter or longer than

current 69 base-long sequences used in current work) without the need to re-optimize multiple PCR parameters (e.g. template concentration, primer concentration, dNTP concentration, number of PCR cycles, etc.)

- Implemented a novel aptamer selection approach (that we call Competition-Induced Selection of Ligands or CISL) as an alternative to conventional SELEX (Systematic Evolution of Ligands by EXponential enrichment)-based approach that has dominated the literature for over 20 years. Unlike conventional SELEX which is labor intensive and time-consuming (typically weeks), our *non*-SELEX approach for planar gold substrates requires ~1 day and eliminates intermittent PCR steps that are prone to sequence error and sequence bias (towards “early winners”).
- Used CISL and our single-stranded libraries (prepared via solution-based PCR and enzymatic digestion described previously) to identify multiple aptamers candidates from random libraries (25% A, T, C, G) and adenine-rich random libraries (40% A and 20% T, C, G) were identified for (i) polycrystalline planar gold substrates (ii) gold nanospheres and (iii) gold nanorods.
- Analyzed and compared primary structures of identified aptamer sequences using (i) Geneious to identify position-dependent matches in individual bases amongst groups of aptamer sequences and (ii) MEME software to identify position-independent consensus in segments of bases amongst groups of aptamer sequences for a given material target.
- Analyzed and compared predicted secondary structures using Zuker’s UNAFold program to classify aptamer sequences for a given target according into “structural point groups” that share identical structural features (i.e. same number of single-stranded segments, duplexes, hairpins, bulges, internal loops, and multibranch loops)
- Used Next Generation Sequencing (NGS) to rank a group of 25 aptamers for planar polycrystalline gold according to the frequency as an adsorbate species.

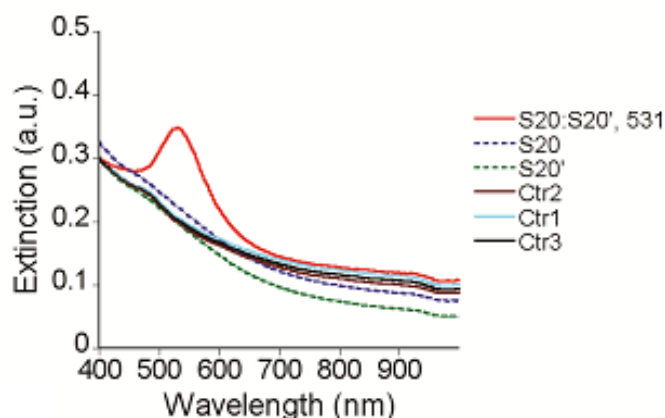


Figure #S-2.1. UV-Vis spectra of gold seeds following incubation with various complementary ssDNA alone (**S20** or **S20'**) and mixed together (**S20:S20'**) for 2 h. Three controls (Ctr1,2,3) are also shown in which DNA is absent. A noticeable 531 nm peak emerges only for seed suspensions incubated with the **S20:S20'** duplexes indicating that rapid precipitation of gold nanoparticles occurs in the presences of DNA duplexes, but not in the presence of its single-stranded components. (Taken from Tapp *et al.* accepted in *J. Mater. Res.*)

Approaches and Results:

Spectroscopic Studies

The effect of adding nucleic acids to gold seeds during the growth stage of either nanospheres or nanorods was investigated using UV-Vis spectroscopy to reveal any oligonucleotide base or structure-specific effects on nanoparticle growth kinetics or plasmonic signatures. Spectral data indicate that the presence of DNA duplexes during seed ageing drastically accelerated nanosphere growth as shown in **Figure #S-2.1** while the addition of single-stranded polyadenine at any point during seed ageing induces nanosphere aggregation. For seeds added to a gold nanorod growth solution, single-stranded polythymine induces a modest blue-shift in the longitudinal peak wavelength. Moreover, a particular sequence comprised of 50% thymine bases was found to induce a faster, more dramatic blue-shift in the longitudinal peak wavelength compared to any of the homopolymer incubation cases as shown in **Figure #S-2.2**. Monomeric forms of the nucleic acids, however, do not yield discernable spectral differences in any of the gold suspensions studied.

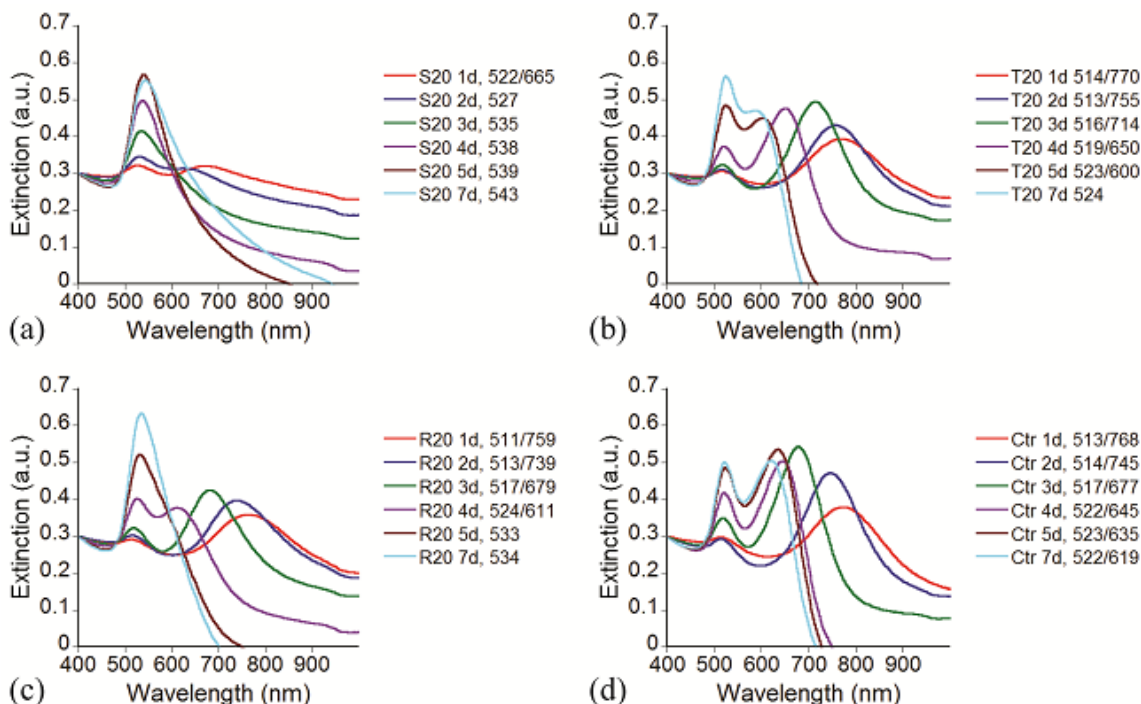


Figure #S-2.2. UV-Vis spectroscopy over the first 7 d (1-day intervals) of gold seeds in AuNR growth solution incubated with the following solution additions: (a) **S20** (b) **T20** (c) **R20** or (d) 2 μ L Tris HCl only (no DNA). The resulting peak wavelength values are included in the legend. (Taken from Tapp, *et al.* accepted in *J. Mater. Res.*)

PCR Optimization

By “tweaking” several PCR parameters (e.g. template concentration, number of PCR cycles, etc.) we were able to successfully amplify a random DNA sequence library to generate the desired double-stranded DNA (dsDNA) with no discernable side-products as shown by the clean, bright band in Lane 2 in **Figure #S-2.3**. For subsequent aptamer

selection steps, however, the next step is to dissociate and recover the amplified, single-stranded template strands. In brief, phosphorylated reverse primer is used during PCR to generate phosphorylated hybridization partners to the template strands. The exponential PCR product is precipitated (using glycogen as a carrier) and then subjected to lambda exonuclease digestion to selectively cleave the phosphorylated hybridization partner leaving behind intact, single-stranded template strands as shown in Lane 4 in **Figure #S-2.3**. We then confirmed that the lambda exonuclease digestion successfully leaves only ssDNA (and not mixtures of ssDNA + partial duplexes, etc.) using a second enzymatic digestion assay involving Exonuclease I (which selectively cleaves only ssDNA) as shown by the “bandless” Lane 5 in **Figure #S-2.3** while the dsDNA in Lane 3 remains unmodified by the presence of Exonuclease I in Lane 3.

Libraries were prepared as outlined above and then used in our CISL-based screening method to identify 20-25 aptamers for each of the gold-based targets: (i) planar gold, (ii) gold nanospheres, and (iii) nanorods. Highlights of the analysis are presented below. The alphanumeric nomenclature of the aptamers signifies the colony number (1-20) followed by the letter N (if originated from the equimolar A,T,C,G library) or A (if originated from the adenine-rich library).

Analysis of Aptamer Primary Structure to Identify Position-dependent Base Consensus

Analytical results shown in **Figure #S-2.4** show two pairs of aptamers for planar gold

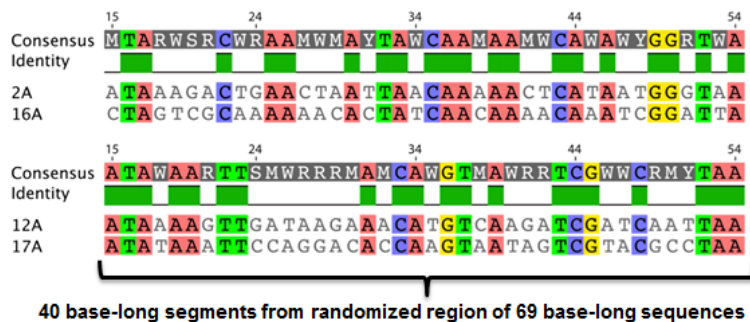


Figure #S-2.4. Geneious software analysis to identify two or more aptamer sequences for planar gold target that possess consensus in at least 50% of the bases at specific locations in the central 40 base-long segment. Here (out of 25 aptamers, two pairs of aptamers (2A & 16A; 12A & 17A) meet these consensus parameters. (Taken from Tapp, Dennis, Naik, Milam, *manuscript in preparation*)

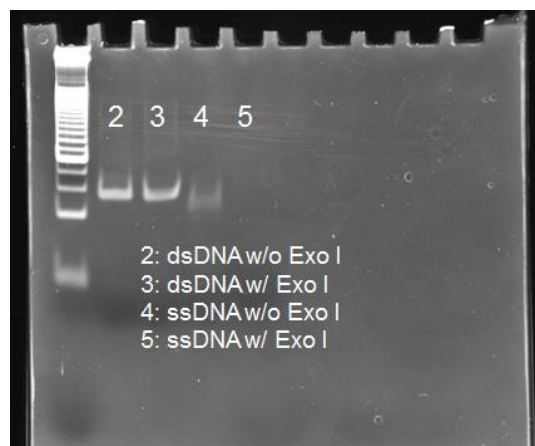


Figure #S-2.3. PAGE analysis indicating successful PCR amplification of 69 base-long ssDNA templates to form double-stranded product (Lane 2) which does not undergo enzymatic cleavage by Exonuclease I (Lane 3). In contrast, the ssDNA resulting from lambda exonuclease digestion (Lane 4) readily undergoes enzymatic cleavage by Exonuclease I leaving a “bandless” lane (Lane 5). Lane 1 is a 25 base-long ladder that is used as a calibration standard. (Taken from Tapp, Dennis, Naik, Milam, *manuscript in preparation*).

(2A & 16A; 12A & 17A) that share 50% consensus in individual bases *in the entire sequence* using a software program called Geneouis version 7.1 (created by Biomatters.) Additional Geneouis software analysis (not shown) for individual bases found in at least 50% of all aptamer sequences (regardless of the extent of overall consensus in remaining bases) indicated that all 25 aptamers identified for planar gold shared 50% consensus in 6 (out of 40) base positions.

Analytical results shown in **Figure #S-2.5** show groups of 4 aptamers for gold nanospheres (out of ~20 aptamers total) graphically depicts consensus segments of bases (**Fig. #S-2.5a**) for four aptamers, two of which (10A and 15A) are identical sequences (**Fig. #S-2.5b**).

Analysis of Predicted Secondary Structures to Identify Common Structural Features

Using predicted secondary structures from UNAFOLD analysis, Structure Point Groups were identified among 2 or more aptamer sequences out of a group of ~20 aptamers. Each Structure Point Group shares an identical number of the Secondary Structure Elements (e.g. identical number of SS, D, HP, IL, B, and MBL) defined in **Figure #S-2.6**. Notably, while predicted secondary structures are commonly reported in the aptamer literature, we expanded this analysis to assign Structure Point Groups in order to avoid any visual bias towards a specific type of Secondary Structure Element such as the commonly reported hairpin (also called a stem-loop) structure routinely highlighted in the oligonucleotide literature. As one example, 2 aptamers (1N and 10A) in the same Structure Point Group (2SS, 3D, 2HP, 2IL, 0B, and 1MBL) are shown in **Figure #S-2.7**.

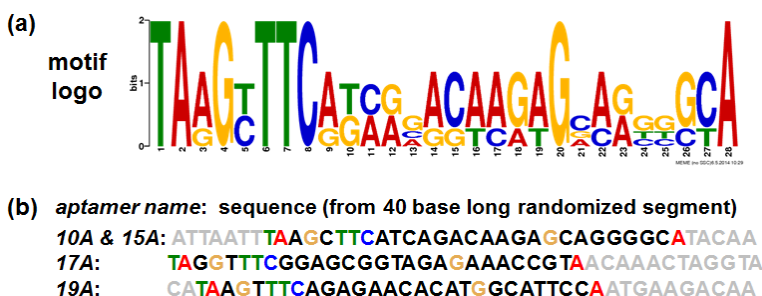


Figure #S-2.5. Four representative DNA aptamers (out of ~20) for gold nanospheres identified from Milam's *non-SELEX*-based screening approach. Sequence analysis to identify (a) statistically significant (E-value = $2E-4$) consensus motifs via MEME software in which the identified motifs are 28 bases (shown in color or black) in length (out of 40 bases total in the original randomized library) and (b) aptamer sequences identified from various clones. Notably, aptamer sequences 10A and 15A are identical though they each originated from different colonies following bacterial transformation.

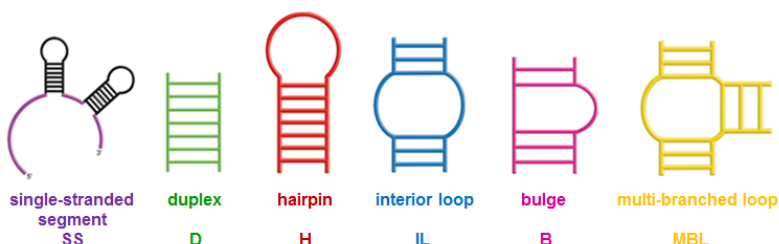


Figure #S-2.6. Schematics of all Secondary Structure Elements used in analysis of shared structural features across aptamer candidates based on their predicted secondary structures (Taken from Tapp, Dennis, Naik, Milam, *manuscript in preparation*).

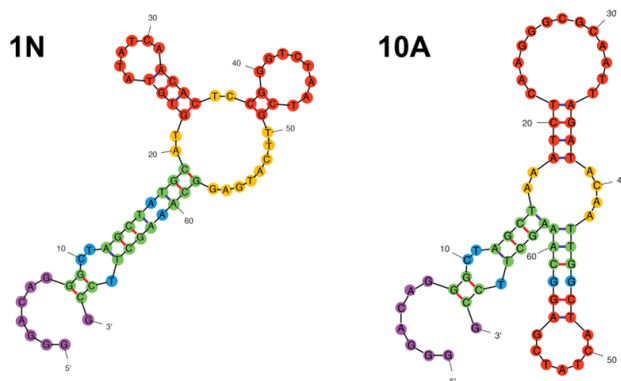


Figure #S-2.7. Two DNA aptamers, **1N** and **10A**, (out of ~20) for planar gold that belong to the same Structure Point Group (2SS, 3D, 2HP, 2IL, 0B, and 1MBL). (Taken from Tapp, Dennis, Naik, Milam, *manuscript in preparation*).

Analysis of Frequency of Aptamer as an Adsorbate Species Using Next Generation Sequencing

In order to “rank” aptamers in terms of their frequency as bound species for a chosen target (here, planar gold) a key experiment involved incubating the gold target with an equimolar concentration of all aptamer sequences, removing all unbound strands, then identifying all bound sequences (identified through high throughput, Next Generation Sequencing) in order to rank all 25 sequences in terms of their frequency as adsorbate species. The frequency ranking results shown in **Figure #S-2.8** depict one particular aptamer (**1N**) with significant counts ($\sim 2 \times 10^6$ counts) compared to all 24 other aptamer sequences with at least one order fewer counts than **1N** ($\sim 3 \times 10^5$ counts or less).

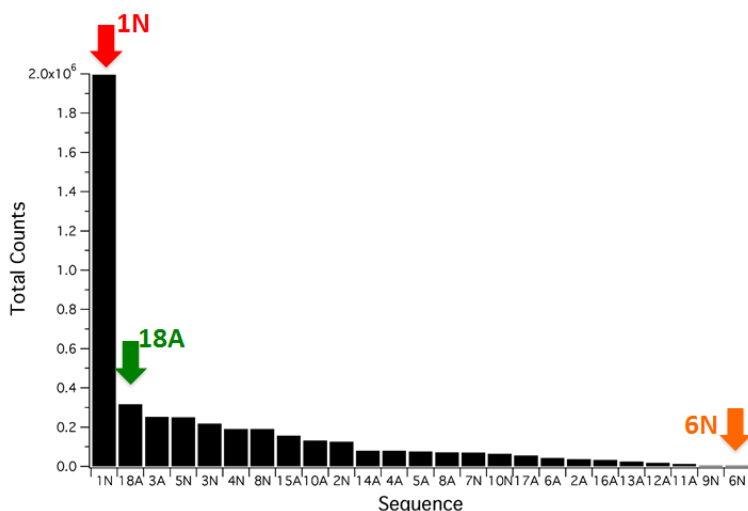


Figure #S-2.8. Histogram of counts associated with a candidate aptamer sequence as a bound species to its target (planar gold) determined via next generation sequencing. The number-letter nomenclature for the aptamers is based on the colony number and the ratios of nucleotides in the original library (**N** represents sequences with 25% A, T, G, C and **A** represents adenine-rich sequences with 40% A, and 20% T, G, C. The choice to employ adenine-rich libraries was based on separate spectroscopic studies (Tapp *et al. accepted to J. Mater. Res.*) that indicated strong affinity of polyadenine for gold targets.

Interactions with AFRL:

- While much of the research efforts physically occurred at Georgia Tech, these research efforts were based entirely on a collaborative research approach between Milam and Naik and their respective group members. Several proposals (e.g., NSF, DARPA) have been submitted by Milam with Naik as a collaborator.
- Valeria Milam spent 9 weeks in 2009 as a Summer Faculty Fellow in the laboratory of Rajesh Naik to initiate their collaborative efforts on aptamer research. She worked closely with Pat Dennis and Matt Dickerson. She visited AFRL for one-two days at various points between 2010-2014 to confer with Rajesh and his group on research progress.
- Between 2010-2013, both Maeling Tapp and Rick Sullivan spent several weeks during the fall and summer terms in the laboratory of Rajesh Naik learning and refining various technical aspects and undertaking experiments for aptamer-related research endeavors.
- Regular teleconferences (typically at least monthly) occurred between the Milam and Naik groups to provide updates and get input on the collaborative research efforts

Former BIONIC Students at AFRL:

None to date

Publications:

- M. N. Tapp, R. Sullivan, P. B. Dennis, R. R. Naik, V. T. Milam, "Effects of nucleic acid additions on seed-mediated growth of gold nanoparticles," *accepted for publication in J. Mater. Res.*
- Several manuscripts are currently in preparation.

Presentations (*invited):

- M. N. Tapp, P. B. Dennis, R. R. Naik, V. T. Milam, 2012 Spring Materials Research Society Meeting "Screening for DNA aptamers that bind to gold substrates," San Francisco, CA, April 2012.
- R. Sullivan, M. N. Tapp, R. R. Naik, V. T. Milam, Poster presentation at 2012 Spring Materials Research Society Meeting "The effects of CTAB on single-stranded DNA binding to gold nanorods," San Francisco, CA, April 2012. (*One of four posters in symposium to receive an award*)
- M. Tapp, P. Dennis, R. Naik, V. T. Milam, "Exploring the effects of incubating gold nanoparticle seeds with nucleotides and oligonucleotides" Graduate and Postdoc (GaP) seminar, Georgia Tech, April 2013.
- R. Sullivan, M. Tapp, P. Dennis, R. R. Naik, V. T. Milam, "Effects of DNA on Gold Nanorod Growth" Sound bite presentation at 7th Southeast Workshop on Soft Materials, Atlanta, GA, May 2013.
- M. Tapp, P. Dennis, R. Naik, V.T. Milam "Exploring the effects of incubating gold nanoparticle seeds with nucleotides and oligonucleotides" Sound bite presentation at 7th Southeast Workshop on Soft Materials, Atlanta, GA, May 2013.
- R. Sullivan, M. N. Tapp, P. Dennis, R. Naik, V. T. Milam, 88th American Chemical Society Colloid & Surface Science Symposium, "Effects of nucleic additions on plasmonic signatures of gold nanoparticles," Philadelphia, PA, June 2014.

- M. N. Tapp, R. Sullivan, P. B. Dennis, R. R. Naik, V. Milam, 88th American Chemical Society Colloid & Surface Science Symposium, "NonSELEX approach to identify DNA aptamers for gold substrates," Philadelphia, PA, June 2014.
- *V. T. Milam, "Implementing a non-SELEX route to select DNA aptamers for material targets" Colloquium talk presented at Penn State University, University Park, PA, October 9, 2014.
- *V. T. Milam, "Competition-induced selection of aptamers for non-nucleotide targets," Colloquium talk presented at University of Minnesota, Minneapolis, MN, Oct. 14, 2014.
- *V. T. Milam, "Rapid interrogation and identification of DNA aptamers for material targets," Colloquium talk presented at University of Florida, Gainesville, FL, Nov. 25, 2014.
- *V. T. Milam, M. N. Tapp, R. Sullivan, P. B. Dennis, R. R. Naik, "Implementing a *non*-SELEX aptamer screening approach for material targets," 2014 Fall MRS Meeting, Boston, MA, Dec. 2014.
- *V. T. Milam, UIUC, "Panning against gold," Champaign-Urbana, IL *to be given February 5, 2015, Invited Seminar*
- *V. T. Milam, Boise State University, "Competition-Induced Selection of DNA aptamers for material targets," Boise, ID *to be given February 20, 2015, Invited Seminar*
- *V. T. Milam, R. Sullivan, M. N. Tapp, P. Dennis, R. R. Naik, "Shape-Specific DNA Aptamers for Colloidal Gold," *To be presented* at 2015 Spring MRS Meeting, San Francisco, CA, April 2015.

Seed Grant #3: Functional Bionanocomposites based on Photopatterning of Protein Aggregates, Fluoropolymers, and Hydrogels

Georgia Tech Participants: Project PI: Prof. Joseph Perry; Students: Jeannie Yom; Post-docs/Research Scientists: Simon Dunham, Vincent Chen

AFRL Collaborators: WPAFB: Dr. Rajesh R. Naik, Dr. Patrick B. Dennis, Dr. Matthew Dickerson

University Collaborators: Georgia Tech: Prof. Kenneth H. Sandhage, Dr. Yunnan Fang; Scripps Institution of Oceanography: Dr. Dimitri Deheyn

Research Goals:

- Development of functional bionanocomposites based on photopatterning of protein aggregates
- Formation of ferroelectric polymer actuators via two-photon 3D-microfabrication
- Develop understanding of how to create electro-active structures based on ionic liquid containing hydrogels

Key Achievements:

- Demonstrated 3D patterning of ferroelectric polymer (PVDF-TrFE)
- Constructed electroactive structure based on visco-hyperelastic elastomer and ionic liquid hydrogel electrodes
- Formed protein-based breath figure dispersive structure and pH responsive protein microstructures

- Demonstration of all-protein microlaser based on BSA and green fluorescent protein composites

Approaches and Results:

Functional Bionanocomposites based on Patterning of Protein Aggregates

We have investigated the formation of dispersive optical structures based upon solution processing of thin films of proteins, specifically sheep derived *a*-keratins. Initially, we intended to pursue the formation of 3D-grating structures of reflectin proteins via two-photon 3D-lithography, building on the work previously done at AFRL by Naik and collaborators. Unfortunately, we were not able to obtain sufficient amounts of reflectin protein to pursue 3D fabrication of reflectin aggregate structures. Therefore, we changed the target protein to commercially-available, sheep-derived *a*-keratins.

Our initial plan was to determine whether the sheep derived *a*-keratins would form protein aggregate grating structures upon shear processing from solution as was reported previously for *b*-reflectin. The *a*-keratin protein was processed by blade casting from hexafluoroisopropanol with a concentration of 40 mg/mL. We observed that the *a*-keratin films showed some color dispersion, as was observed by Naik, et al. for *b*-reflectin containing films. However, the character of the color dispersion was somewhat irregular and appeared to vary across the film. We performed optical imaging of the surface texture of the *a*-keratin films, which revealed micro-scale rings of various sizes with heights of 10 to 20 nm, that were reminiscent of the so-called breath figures which are formed on films during processing while being subjected to humid air (breath), as shown in **Figure #S-3.1**.

It is apparent that increasing numbers of breath treatments generates an increasing number of microrings, (**Figure #S-3.2 middle**) which is consistent with the deposition of increasing numbers of microscale water droplets. Furthermore, for a given breath treatment, the droplets undergo some reorganization with the smaller droplets diminishing in number and the larger droplets increasing in size. SEM imaging reveals details of the evolution of the microrings as a function of breath treatments and time as shown in **Figure #S-3.2 top**. Starting with the as cast film, the surface topography is relatively smooth, whereas there is considerable “catering” that occurs with increasing breath treatments. However, after sitting for two weeks the outline of the “craters” is still visible but the microstructure is dominated by sub-micrometer features on the order of 250 nm. We also compare the surface microstructure of breath figures formed in *a*-keratin films processed at AFRL and Georgia Tech, as well as samples of *b*-reflectin and poly(styrene-co-acrylonitrile) (PSAN) treated with breaths, shown in **Figure #S-3.2 bottom**. While the breath figures in the films of *a*-keratin processed at the different locations show varying different amounts of small pores, the larger pores appear to be of the same order in length. The breath figure in the *b*-reflectin film also shows microscale and sub-microscale features. On the other hand, the breath figure in the PSAN film show microscale pores but relatively little in the way of submicrometer pores, which may be due to surface energy differences that may confine the breath droplets from spreading and redistributing the droplets in smaller features.

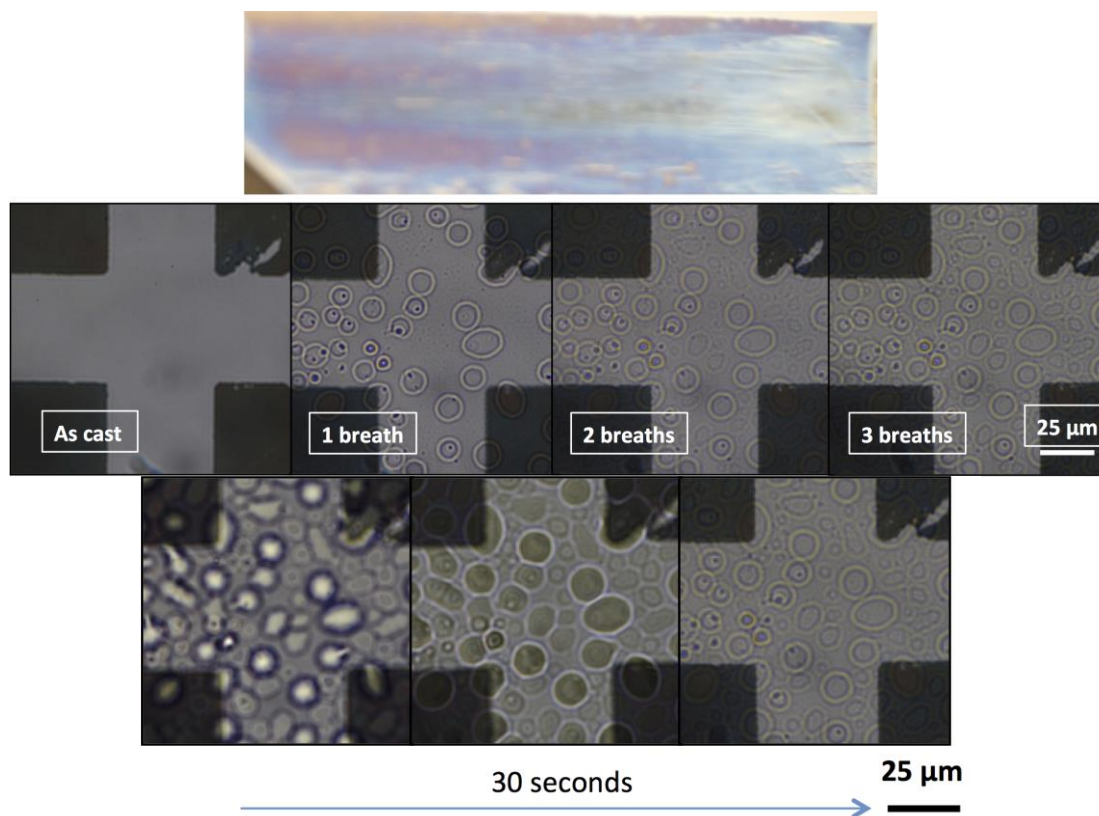


Figure #S-3.1 Top) Color image of scattered color from breath figures on α -keratin films. Middle) Optical images of the development of breath-figures on films of α -keratin films for increasing numbers of breath treatments. Bottom) Optical images of development of breath figures on α -keratin over time.

Ferroelectric polymer actuators via microfabrication

Materials and processing methods have been developed that allow for multiphoton lithography of PVDF-TrFE and conductive ionic liquid hydrogels. We have characterized the resulting materials and performed demonstration of their functionality in several applications. We have implemented multiphoton lithography in attempts to form advanced soft actuators.

Ionic liquid hydrogel transmission line studies

Previous experiments with ionic liquid/hydrogel samples, which were fabricated by molding and photoexposure (**Figure #S-3.3**, left), demonstrated that the ferroelectric polymer material has sufficient conductivity to be used as a dielectric-elastomer-actuator electrode material (with a resistivity of $\sim 1 \Omega\text{m}$). However, tests are still needed to show that materials patterned by multiphoton lithography also possess similar properties as those prepared by molding. Here, transmission line studies, whereby arrays of two terminal resistive devices are patterned and characterized with varying length and width, allow for deconvolution of bulk and contact effects without complex four terminal electrode designs.

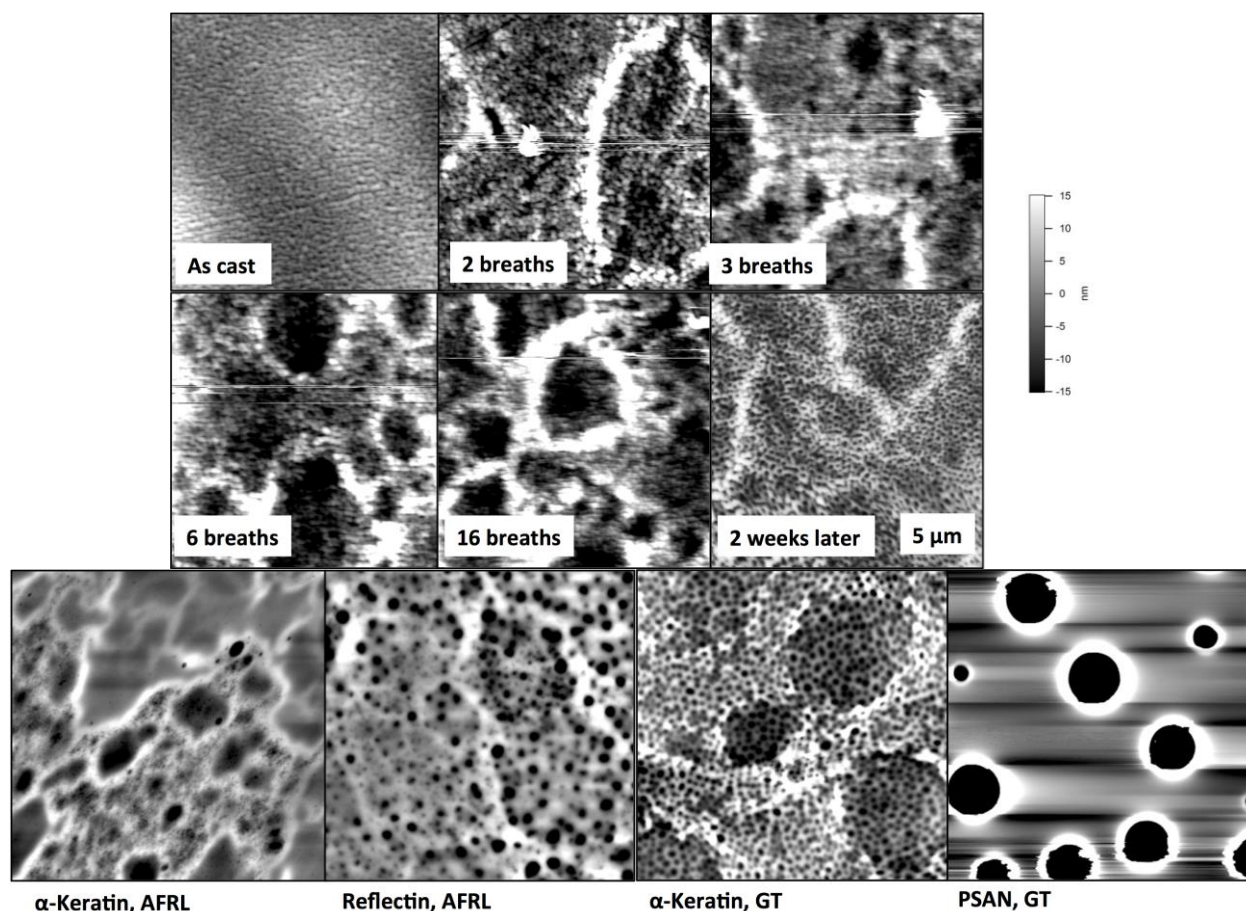


Figure #S-3.2. Top) SEM images of the development of breath-figures on films of α -keratin films for increasing numbers of breath treatments. Bottom) SEM images of breath figures formed on different protein and polymer surfaces.

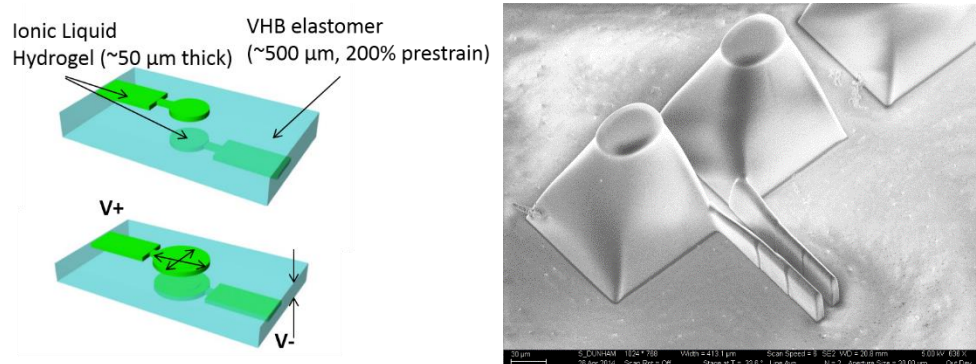


Figure #S-3.3. Schematic of UV patterned hydrogel actuator (left) and multiphoton patterned hydrogel microactuator (right).

Microscale dielectric elastomer actuator demonstration

Previous experiments demonstrated the potential for using ionic liquid hydrogels as electrodes for large (mm scale) dielectric elastomer actuators. Furthermore, multiphoton patterning of these materials allows for precise placement and geometry at μm size scales. Demonstrations of microscale dielectric-elastomer-actuators provide evidence of

the utility of this approach. Here, a soft dielectric material (PDMS or some other soft silicone such as locktite) can be patterned and cured into a small thin cube (~10-30 μm tall, 2-5 μm thick, and 50-200 μm long) utilizing PDMS micromolding with a fluorinated stamp. Then, multiphoton lithography could be used to pattern electrodes making electric contact on either side of the soft dielectric feature (such that the 2-5 μm thick dimension becomes the dielectric thickness) and connection to large probe pads (100x100 μm) so that the device could be characterized using a conventional probe station (**Figure #S-3.3**, right).

Multiphoton fabrication of microstructures in P(VDF-TrFE)

We have developed processes and protocols for multiphoton lithography based on crosslinking of poly[(vinylidene fluoride-co-trifluoroethylene) [P(VDF-TrFE)] using 2,6-Bis(4-azidobenzylidene)-4-methylcyclohexanone (BA) as the photoinitiator. Here, the photoactive BA yields nitrene radicals upon exposure to UV light (350 nm). These radicals can undergo insertion reactions with C-H groups in the PVDF polymer chain forming crosslinking in the linear chains of P(VDF-TrFE) (**Figure #S-3.4a**). After photocrosslinking solvents such as acetone or DMF can be used to remove uncrosslinked material.

P(VDF-TrFE) photoresists with 2-5 wt% of BA were blade cast from 20 wt% solutions of methyl ethyl ketone (MEK) and softbaked at 60°C for 2 min and dried in a vacuum oven at room temperature for 12 hours. Film thicknesses can be achieved up to 30 μm without loss of optical quality in the resist. The solvent system and processing conditions were carefully optimized to prevent scattering in the resists. However, the addition of BA to the solid resist yielded films with less transparency (**Figure #S-3.4b**). No change in the phase of the material (no change in PVDF peaks of FTIR upon addition of BA) was observed, most likely due to changes in crystallite size and/or low levels of aggregation of BA.

The solid resist also allows for control of the phase and crystallinity of the P(VDF-TrFE) based on the processing conditions used to create the resist, which are unchanged upon UV exposure. **Figure #S-3.4c** shows FTIR spectra for the P(VDF-TrFE) resist as cast. The peaks at 1431 and 1279 cm^{-1} are characteristic of the ferroelectric beta phase. Additionally the high ratio of the 841 to 881 cm^{-1} peaks provide further proof of the presence of beta phase, while the lack of a 615 cm^{-1} peak suggests there is no alpha phase present.

Multiphoton lithography was used to create a variety of fine featured structures (down to ~2 μm). **Figure #S-3.5** shows a variety of structures written in this manner and illustrates the versatility of this approach. **Figure #S-3.5a,b** show SEM of a dose array of cubes and a woodpile respectively. MPL can also be used to add to or modify existing structures. **Figure #S-3.5c,d** show microscope images and colorized SEM of SU8 structures (fabricated via traditional lithography) which were then modified or added to via P(VDF-TrFE) MPL. The yellow color in the optical micrographs is associated with the absorbance of the BA in the P(VDF-TrFE) resist and is a clear indicator of the difference in materials. **Figure #S-3.5c** shows the case of a thin membrane of P(VDF-TrFE), which has been created to span two SU8 beams. It also suggests how this approach could be used to modify the surface of existing structures even those with complex structure. Furthermore, these structures have shown good adhesion to underlying substrates or in this case the underlying SU8 structures, most

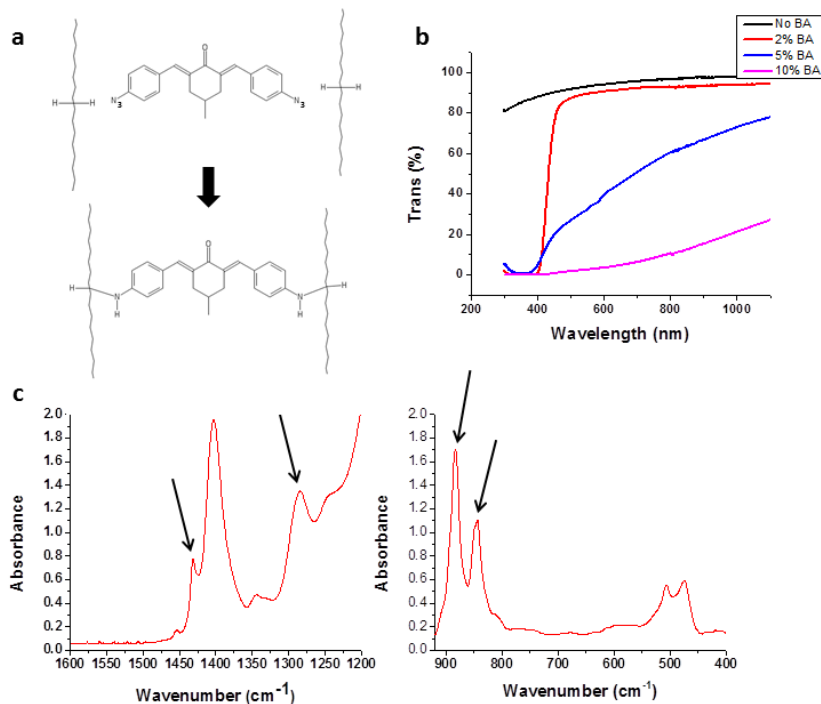


Figure #S-3.4. a) chemistry of BA reaction with P(VDF-TrFE) backbone to yield crosslinked polymer. b) UV-vis transmission spectra of P(VDF-TrFE) resists based on BA content. Increased BA content yields scattering and degrades optical quality of resist making it unsuitable for MPL. c) FTIR of P(VDF-TrFE) resist. Highlighted peaks indicate the presence of the ferroelectric beta phase.

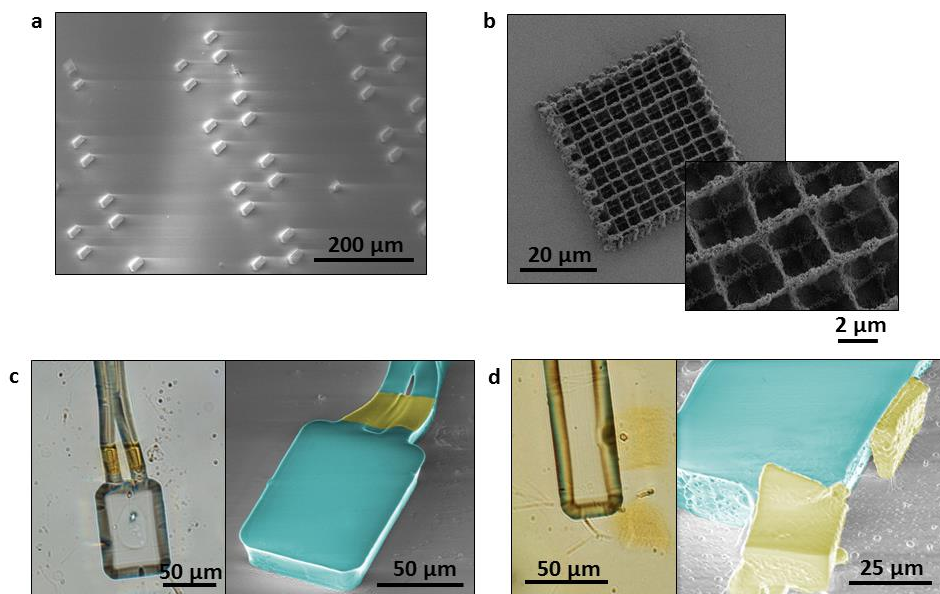


Figure #S-3.5. a,b) SEM of dose array of P(VDF-TrFE) cubes and woodpile structures respectively. c) Optical micrograph and colorized SEM of P(VDF-TrFE) membrane spanning two prefabricated (traditional lithography) SU8 beams. The yellow color is associated with the presence of the BAC in the P(VDF-TrFE) membrane. d) Optical micrograph and colorized SEM of P(VDF-TrFE) cubes attached to the side of a prefabricated SU8 beam.

likely based on crosslinking between the substrate and the P(VDF-TrFE) (due to the BA). **Figure #S-3.5d**, shows the case where an additional structure has been written in contact with an existing one. These two cases illustrate the ability to both modify and add to existing structures in complex ways via P(VDF-TrFE) MPL.

Once the functionality of multiphoton lithography is demonstrated for μ -scale sensors and actuators, its versatility can be utilized to design and fabricate more advanced piezoelectric or dielectric elastomer sensors or actuators such as sensors or actuators with arbitrary geometries and small features. Some examples include fiber array sensors, whereby compression of the fiber array results in buckling of individual fibers yielding an enhance pressure response. Other examples also include actuators which mimic simple biological systems, such as artificial cilia, providing a test case to gain insight into the operation of this type of system.

All-protein microlaser with green fluorescent protein

Extending our work on microlasers based on organic dye-doped polymer resonators, we have investigated the possibility of the fabrication and use of all-protein based microlaser and microresonators. In the all-protein based system, both the emissive material and the resonator materials are comprised solely of biomaterials/proteins.

In preliminary work, we have used GFP (green fluorescent protein) as an emissive to coat hydrogel resonators fabricated using two-photon induced direct writing process. The hydrogel resonator was fabricated using the hydrogel resin comprised of HEMA (hydroxyethylmethacrylate), n-vinylpyrrolidone and tetraethyleneglycol-diacrylate. The feasibility of using super-GFP as a gain medium has been shown by application of a concentrated super GFP (12 μ g/10 μ L) to hydrogel resonators. In this approach, a GFP thin film coating on the resonator resulted from the incubation of the GFP solution with the resonator followed by a drying process. Confocal microscopy revealed GFP penetration into the hydrogel resonator was very minimal (**Figure #S-3.6**, right), which is likely caused by poor swelling of the hydrogel material. Although little penetration was observed on the resonator structures, areas of dried GFP films showed amplified spontaneous emission, as evidenced by the band narrowing under optical pumping (488 nm), with a distinct lasing threshold (**Figure #S-3.6**, left).

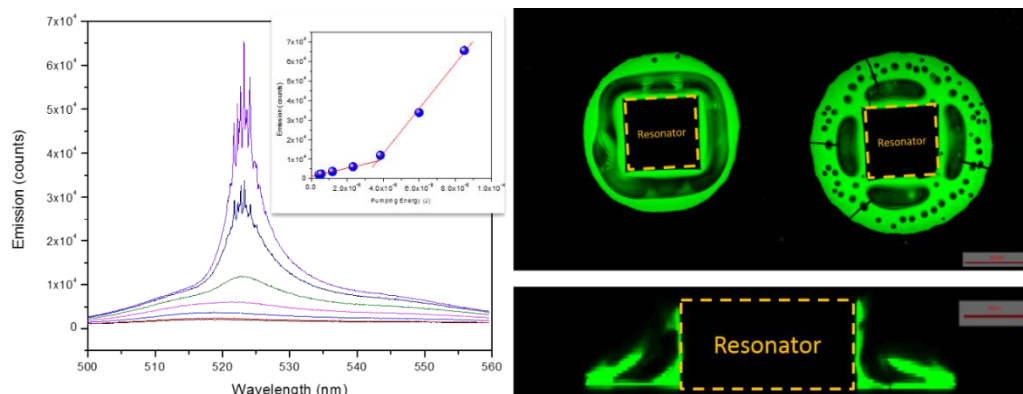


Figure #S-3.6. Evolution of emission spectrum of GFP film excited with increasing energy (left) and the lasing threshold (inset). Confocal image ($\lambda_{\text{ex}}=488$ nm) of the microresonator incubated with GFP solution overnight followed by drying (right).

In addition to the above demonstration, we have also successfully fabricated microresonators and photonic crystal structures using the protein precursor, bovine serum albumin (BSA) and methylene blue as a two-photon initiator at 800 nm (**Figure #S-3.7**). As a continuation of this work, in future work we will investigate different methods to incorporate GFP into the BSA based microresonators to fabricate an all-protein based microlaser. In addition to characterizing the photo-stability of GFP under multiphoton irradiation, we will perform experiments to determine approaches to maximize the photo-stability of GFP. Additionally, we have investigated the effect of pH as shown in **Figure #S-3.7** to dynamically control the swelling and deswelling of the microlasers, which should provide the ability to sense changes in pH, for example, by monitoring the wavelength shift of the microlaser.

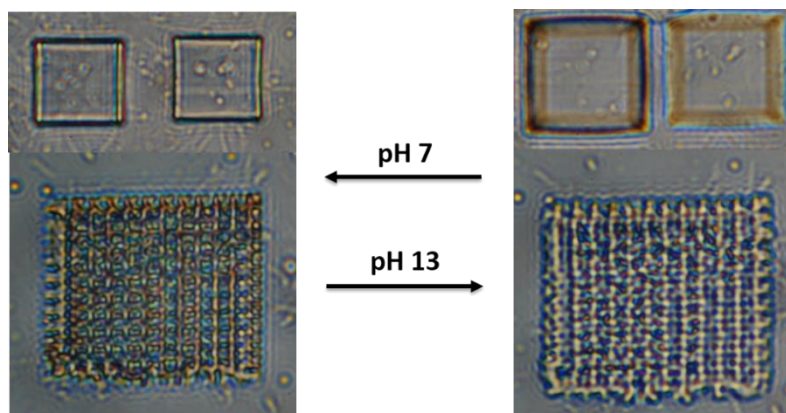


Figure #S-3.7. Image of resonator cuboids fabricated using multiphoton induced writing on BSA precursor using methylene blue two-photon initiator.

Interactions with AFRL:

- Simon Dunham visited AFRL for flow-coating work with the Naik group.

Former BIONIC Students at AFRL:

None to date

Publications:

- Y. Fang, V. W. Chen, Y. Cai, J. D. Berrigan, S. R. Marder, J. W. Perry, K. H. Sandhage, "Biologically-Enabled Syntheses of Freestanding Metallic Structures Possessing Subwavelength Pore Arrays for Extraordinary (Surface Plasmon-Mediated) Infrared Transmission," *Adv. Funct. Mat.*, **22** (12) 2550–2559 (2012).

Presentations (*invited):

- J. W. Perry, V. W. Chen, K. H. Sandhage, Y. Fang, Y. Cai, "Optical Properties of Plasmonic Structures Based on Biological and Synthetically Fabricated Templates," Photonic and Phononic Properties of Engineered Nanostructures" conference in Optoelectronics 2012 Symposium, Photonics West, San Francisco, CA, Jan, 2012.
- J. W. Perry, "Laser Based 3D Microfabrication via Two-Photon Excitation and Surface Modification of Oxide Particles," Dental School, Medical College of Georgia, Georgia Regents University, Augusta, GA, Jan. 17, 2013.

- J. W. Perry, "Bio-enabled and Synthetic Microresonators for Plasmonics and Photonics," Ecole Normale Supérieure de Cachan, Cachan, France (May 31, 2013).
- J. W. Perry, "Organic Materials for All-Optical Switching," Ecole Normale Supérieure de Lyon, Lyon, France, June 7, 2013.
- J. W. Perry, "Three Dimensional Organic Microlasers Fabricated by Multiphoton Lithography," Novel Optical Materials and Applications (NOMA) Cetraro, Italy, June 10, 2013.
- J. W. Perry, "Nanocomposite and Hybrid Sol-Gel Materials for High Energy Density Capacitors," First Annual Southeast Regional Energy Symposium (SERES), Georgia Institute of Technology, July 15, 2013.
- J. W. Perry, "Bio-enabled and Synthetic Microresonators for Plasmonics and Photonics," CIC biomaGUNE, Parque Tecnológico de San Sebastián, San Sebastián, Guipúzcoa, Spain, Oct. 31, 2013.
- J. W. Perry, "Bio-enabled and Synthetic Microresonators for Plasmonics and Photonics," International Workshop on Nano- and Bio-Photonics (FUNMOOD), Domaine de Françon, Biarritz, France, Nov. 4, 2013.
- J. W. Perry, "Nanocomposite and Hybrid Materials for Efficient High Energy Density Capacitors," Electronic Materials and Applications 2014, The American Ceramics Society Meeting, Orlando, FL, Jan. 22, 2014.
- J. W. Perry, Y. Kim, Y. Park, M. Kathaperumal, "Organically Modified Silica Hybrid Sol-gel Capacitors with High Energy Density and Efficiency," The American Ceramic Society Meeting, Orlando, FL, Jan. 21, 2015.

Interdisciplinary Research Group (IRG) #2: Adaptive Nanocomposites
IRG Leader: Vladimir V. Tsukruk

Project IRG #2-1: Responsive 1-Dimensional Metal/Polymer Nanostructures

Georgia Tech Participants: Project PI: Dr. Vladimir V. Tsukruk; Students: Maneesh K. Gupta, Ren Geryak; Post-docs/Research Scientists: Dr. Tobias Konig

AFRL Collaborators: Dr. Richard Vaia, Dr. Rajesh Naik, Dr. Lawrence Drummy, Dr. Dhriti Nepal, Sushmita A. Biswas

Research Goals:

The overall goal of 2-1 research is to develop an understanding for the pairing of stimuli responsive engineered polymer matrices (as signal transduction pathways) with noble metal nanoparticles (as optical reporters) for the design of active plasmonic nanostructured materials with tunable properties. In order to design efficient hybrid plasmonic structures, we will address two general fundamental questions.

- How do interfacial effects between metal and polymer and nanoscale confinement effects impact the responsive nature (occurrence, amplitude and kinetics) of the responsive polymer matrix?
- How can stimuli-responsive polymers and noble metals nanoparticles be paired so that the isotropic swelling of the polymer drives large well defined directional changes in particle coupling and a corresponding stimulus-specific colorimetric response?

Key Achievements:

- Developed and tested an extension of a field-directed self-assembly system in which external magnetic fields could be used to control the orientation and scattering spectrum of nanorods in a fast, tunable, and reversible manner.
- Developed method to deposit an ordered monolayer of functionalized nickel nanorods onto a substrate and a strategy to control the position, spacing, and arrangement of the structures in situ and performed simulations to obtain predicted optical properties of segmented nanorods;
- Developed procedures to transfer linear arrays of gold nanorods to functionalized substrates in large quantity while maintaining fidelity of the linear array structure enabling thorough optical analysis of gold nanorod dimers.

Approaches and Results:

Assembly and Tuning of Magnetic Nanorods Arrays

Fabrication of Segmented Rods

A template-based synthesis approach has been developed to fabricate one-dimensional segmented metallic nanorods that can be paired with responsive polymer systems to yield large and well characterized shifts in the LSPR. Porous anodic alumina membranes are used as templates for electrodeposition of segmented metal nanorods. Alumina membranes are fabricated through conventional two-step anodization methods utilizing phosphoric acid (250-350 nm diameter pores) and oxalic acid (40-80 nm diameter pores) as electrolytes. Freestanding and through-hole membranes are obtained by first dissolving the underlying aluminum substrate and then selective etching of the membrane backside in 5 wt% phosphoric acid solution. Further pore widening in phosphoric acid solution can then be used to increase the pore diameters within the ranges mentioned above.

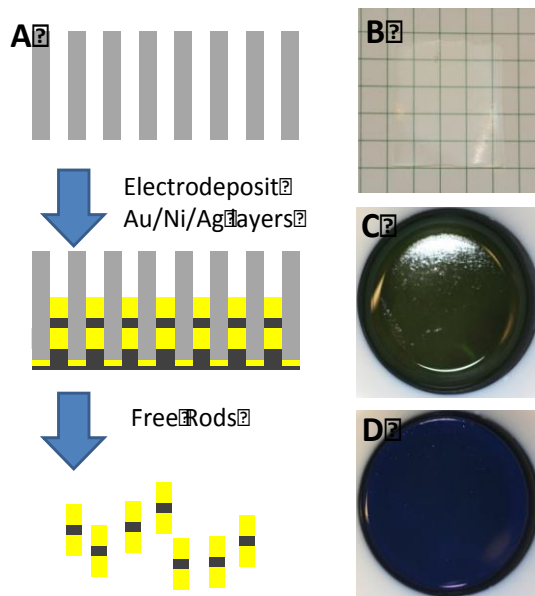


Figure S#2-1.1. a) Schematic of fabrication strategy of segmented nanorods; b) optical photograph of pristine alumina membrane with 50 nm pores (grid line spacing – 0.25 inch); c and d) optical photographs of alumina membrane after electrodeposition of Au and Ag respectively (1 inch diameter)

commercially available solutions at constant voltage conditions against a saturated calomel electrode and platinum foil as counter electrode. **Figure #2-1.1b** is an optical photograph of a pristine alumina membrane with 50 nm pore diameters (gridlines are at 0.25 inch spacing), and **Figures #2-1.1c and #2-1.1d** are optical photographs of the alumina membrane after electrodeposition of gold and silver respectively.

Upon completion of the electrodepositions, the sacrificial nickel electrode is dissolved in concentrated HCl and then the alumina template is dissolved in 1 M NaOH in order to free the segmented rods. The wires are purified by centrifugation to remove the bulk of the NaOH and dissolved alumina, followed by extensive dialysis against water to remove any trace salts. **Figure #2-1.2** shows secondary electron microscopy (SEM) images of segmented rods fabricated in 250 nm diameter pores (a and b) and in 50 nm diameter pores (c and d).

Figure #2-1.1a depicts a brief schematic for the fabrication strategy of the segmented nanorods using alumina templates. First, a thin gold film electrode (50 nm) is sputtered on the topside of the alumina membrane. Using the thin gold film as a working electrode a thicker sacrificial nickel layer is then deposited on the backside of the membrane to provide a robust working electrode for the remaining depositions within the pore. Next, the membrane is mounted in a custom electrochemical cell and gold, silver, and nickel layers can be deposited sequentially using

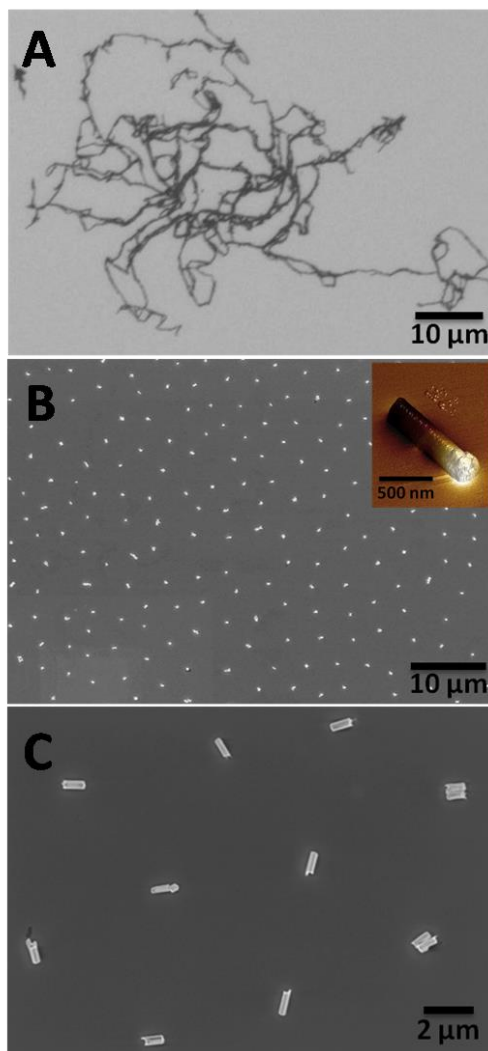


Figure #2-2.2. a) SEM image of chain like aggregates, b) low magnification SEM image of ordered assemblies with MFM image inset, c) high magnification SEM image of rod assembly

Figures 2a and 2c show cross-sections of the segmented rods within the alumina membrane, and **Figures 2b and 2d** show the freed nanorods which were dropcast onto silicon substrates.

Fabrication of One-dimensional Dimer Arrays

In order to determine the optimal geometry of segmented nanorods for tunable plasmonic systems, a preliminary study was undertaken to fabricate one-dimensional arrays of gold nanorod dimers with varying gap distance. **Figure #2-1.3** shows the fabrication one-dimensional arrays of gold nanorod dimers with nickel as a sacrificial metal. After fabricating the rods as described above, the nanorods are thermally embedded in thin polystyrene films to provide mechanical support for the rods. Finally, the nickel sacrificial layers are etched away leaving behind only the gold dimers.

Figure #2-1.4 shows an SEM image of a segmented rod embedded in a polystyrene film after selective etching of the nickel segments (note that the trench in polystyrene film where the nickel segment was is visible). This fabrication method provides a strategy to fabricated metallic dimer arrays on flat substrates with arbitrary rod length, diameter, and gap distance. This method can even be used to fabricate heterodimers with multiple metals which currently is difficult to do with lithographic methods. This array has a gold rod diameter of 50 nm and length of 100 nm. The gap between the rods in the dimers was varied and is approximately 50 nm, 25 nm and 5 nm. **Figure #2-1.4b** is a darkfield optical micrograph of the dimer arrays. It can be clearly seen that there are several dimer arrays each containing three bright spots. The colors of the spots shift from green to orange to red as the gap in the dimer decreases. This shift in color is caused by increased coupling in the longitudinal LSPR. The corresponding shift is also evident in the UV-Vis spectra captured for the dimer array outlined in the white ellipse. It is clear that the maximum absorption shifts for approximately 590 nm for the largest separation to approximately 640 nm for the smallest separation. This study will be completed in an upcoming visit to WPAFB and will provide us with a basis to design dimers that will be utilized in future studies.

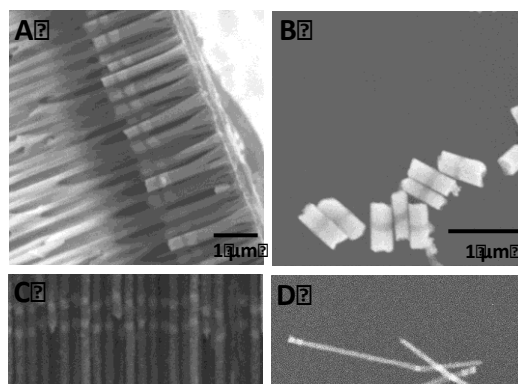


Figure #2-1.3. SEM images of Au/Ni segmented nanorods (brighter metal is Au and darker metal is Ni); **a and c**) cross-sections in alumina membranes; **b and d**) freed nanorods dropcast on silicon

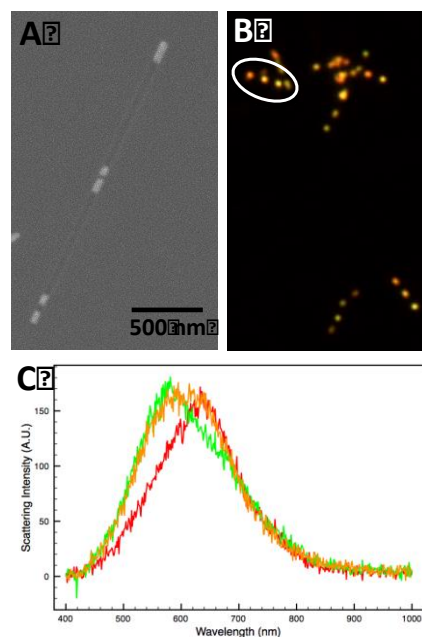


Figure #2-1.1 a) SEM image of 3 Au dimer array embedded in polystyrene; **b)** Darkfield optical images of dimer arrays; **c)** UV-Vis spectra from dimer array outlined in white ellipse.

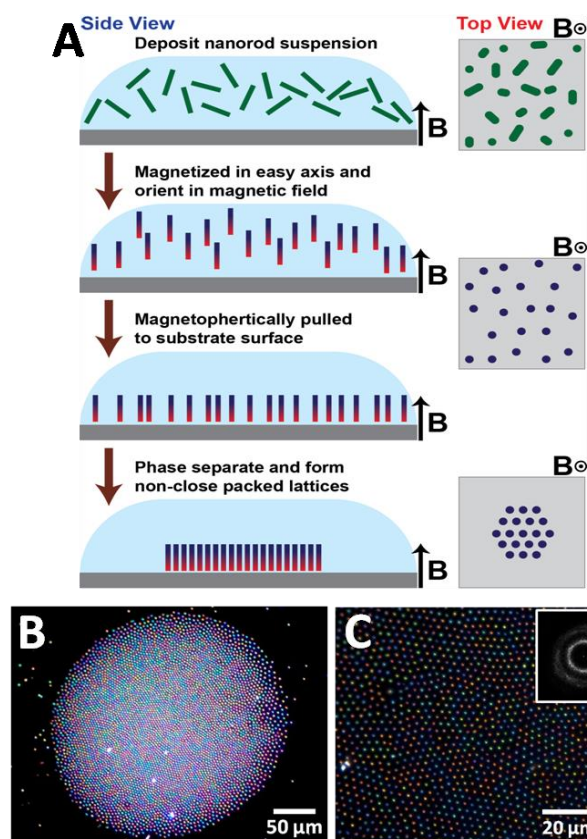


Figure #2-1.2. a) Representative schematic of rod assembly process, b) low magnification image of assembly, c) high magnification of rod assembly with FFT inset.

Perhaps even more intriguing were the possibilities that emerged when the rods were tethered to the surface as previously described. **Figure #2-1.6d** shows the ability to “print” two rod assemblies in arbitrary positions. In this instance, the assemblies shown were composed of rods with two different lengths (400 and 1600 nm, from left to right), demonstrated the versatility of this printing technique. Additionally, as shown in **Figure #2-1.6e**, the tethered rods could be actuated by an external magnetic field such that the rods could move from a nearly horizontal position (left image) to an upright position (right) and any intermediate position, simply by controlling the orientation of the magnetic field.

The ordering of the rods could be preserved by tethering the rods to the silicon substrate (**Figure #2-1.5**). This was accomplished in number of ways: adding a dilute salt solution or using layer-by-layer deposition of complementary polymer pairs (PVPon/PMAA, PAH/PSS, etc.). Because the rods were composed of a ferromagnetic material (nickel) the rods maintained a persistent magnetic dipole.

The rod assemblies were found to be extremely amenable to altering their size, position, and the internal ordering of the rods. As **Figure #2-1.6a** shows, the lattice spacing of the rod assemblies was shown to have a linear relationship with the strength of the external magnetic field. This allows for the possibility of assemblies with essentially arbitrary spacings that can be adjusted in situ. Further, a tilted magnetic field was observed to change the space (or wallpaper) group of the rod ordering from a hexagonal ordering (group p6m), seen in **Figure #2-1.6b**, to a nearly rhombic ordering (group cmm), seen in **Figure #2-1.6c**, as the net external field is gradually tilted.

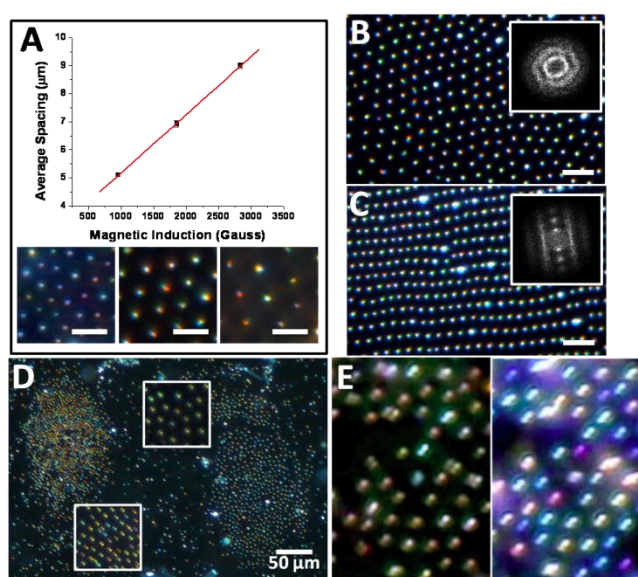


Figure #2-1.6. a) Graph of rod spacing vs. magnetic field with inset images of data points b) assembly with hexagonal ordering with inset FFT, c) assembly with rhombic ordering with inset FFT, d) two “printed” assemblies separated by about 150 μm, e) side-by-side comparison of non-actuated and actuated rod assemblies.

Interactions with AFRL:

- See summary at end of project #2-2.

Former BIONIC Students at AFRL:

- See summary at end of project #2-2.

Publications:

- See summary at end of project #2-2.

Presentations (*invited):

- See summary at end of project #2-2.

Project IRG #2-2: Encapsulation of Living Cells For Cell-Based Sensors

Georgia Tech Participants: Project PI: Dr. Vladimir V. Tsukruk; Students: Irina Drachuk; Post-docs/Research Scientists: Dr. Olga Shchepelina

AFRL Collaborators: Dr. Svetlana Harbaugh, Dr. Nancy Kelley-Loughnane, Dr. Morley Stone, Dr. Rajesh Naik

Research Goals:

This 2-2 project is focused on the development of cyto-compatible, non-ionic layer-by-layer (LbL) shells for developing responsive cell-based sensors. The LbL-derived shells should result in nanocoatings responsive under physiologically relevant conditions without interfering with cell function. *Saccharomyces cerevisiae* yeast cells with incorporated yEGFP reporters were used as the model cells due to the ease in handling the cells and the quick rising fluorescence from the GFP in response to a certain inducer. Specific objectives are:

- Develop a responsive (pH or/and temperature, light) multilayer polymer system for individual encapsulation of cells.
- Optimize the processing conditions for cell encapsulation which would not be deleterious to living cells, with no constrain to the metabolic processes, and prolong the living cycle of cells (Yeast and *E. coli*).
- Demonstrate the ability of the artificial shell applied onto yeast or *E. coli* cells to regulate the cell live cycle (ability to grow) without interfering the cell function (yEGFP expression).

Key Achievements:

- Designed and fabricated a prototype version of multiplexing cell-based biosensor arrays that can be in-printed on silk templated arrays using inkjet technology with preserved sensitivity of cells to detect target analytes even after long-term storage.
- Single cell encapsulation of microbial cells (*S. cerevisiae* yeast cells, *E. coli* and *B. subtilis* bacterial cells) was performed with ionomeric silk fibroin modified with polyLys and polyGlu side chains and the viability of encapsulated yeast cells was evaluated around 95%;
- Encapsulation of yeast cells with PMAA-co-NH₂ pH-sensitive shells resulted in controlled cell reproduction, when increased ionization of shell causes effective uptake of amino acids and hence delay in reproductive activity of cells.

- Robust and stable silk ionomer microcapsules with pH-triggered permeability were fabricated by combining ionic pairing and covalent crosslinking of functionalized groups. The capsules showed significant and reversible pH responsive behavior at pH below 2.0 and above 11.0, the maximum volume swelling reaching 800%.
- Biocompatible, ultrathin, highly porous silk microcapsules were produced using one-component “silk-on-silk” LbL technique. The silk microcapsules demonstrated controlled permeability and facilitated high cell viability.

Approaches and Results:

Bioenabled Coatings

The bio-molecule depositions have successfully deposited the amino acids tyrosine and histidine onto different surfaces which could then be modified through nanoparticle reduction. Gold nanoparticles were reduced from solution on the tyrosine films and titania nanoparticles were reduced on the histidine films. These coatings could be applied to a complex surface as well such as 3D microtrusses and could serve as a method of modifying complex shapes embedded in different systems. Patterning of the PECVD films also allows for the directed placement of these particles on the surface. One example shown with the tyrosine/gold system highlights the scale on which this process is capable where large substrates can be easily coated with gold particles which is visibly evident through a significant color change (**Figure #2-2.1**). As a natural evolution of amino acid depositions, short sequences of peptides have become a new area of focus. A three amino acid peptide of glutathione has been deposited on a silicon substrate as a test case, proving the viability of this technique. This represents a first test of this type of deposition and will require further exploration and characterization. This will also be adapted to other peptides as the study progresses.

Responsive coatings deposited by PECVD have been a second area of interest. The primary focus has been to adapt responsive materials such as pNIPAAm for optical applications. One method that is under investigation is the co-polymerization of pNIPAAm with titania isopropoxide which introduces a high refractive index component into a responsive system. The responses are studied using spectroscopic ellipsometry under different humidity conditions as well as temperatures. The plasma deposited films only show a modest response to moisture on the order of around 10% which is much lower than previously reported values of 200-300%. This is likely a result of the high degree of crosslinking occurring during the deposition and is an issue that is being addressed. It is of interest to further study the internal crosslinking structure of these films and we hope to be able to do this via neutron reflectivity. Another responsive system into which an investigation is just beginning is the light responsive azobenzene

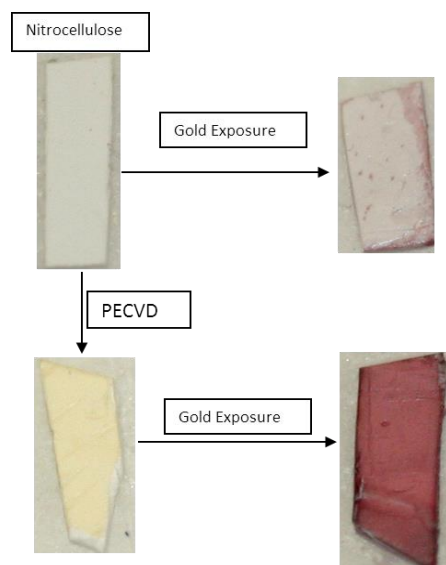


Figure #2-2.1. PECVD of tyrosine (top) and titania (bottom). Copolymerization of the two polymers shows the formation of a unique needle-like structure.

system. Different azo containing monomer can be deposited via sublimation PECVD and adhere well to surfaces. To test the light responsiveness of the material, the monomer will be coated onto a microcantilever and exposed 440 nm laser light. Creating light responsive surfaces this way with PECVD has a wide range of applications which will be the subjects of further study.

Janus particles are systems which exhibit dual surface chemistries. In this case, half of a solid microparticle is coated via PECVD with a polymeric material. Previous studies have confirmed our method of creating particles in this way and we are now focusing on the utilization of responsive coatings on the surfaces of these particles. pNIPAAm, pHEMA and P2VP are all monomers which were plasma deposited onto silica microparticles and are currently being investigated for their responsive and controlled assembly properties (**Figure #2-2.2**). By controlling how these particles assemble in a system, we hope to be able to demonstrate the viability of PECVD coating as a facile synthesis method for a large number of these particles which can then be applied to numerous systems. These solid particles are embedded in a sacrificial layer (typically polystyrene) and coated via the normal PECVD coating methods. The polystyrene layer is dissolved, releasing the particles which then are free with the attached coating on the surface. No surface modification is needed as the exposure to the argon plasma generates radical sites on the monomer and the surface simultaneously activating it to firmly attach the film as it forms. This provides a facile method for creating half coated particles of almost any type of material rapidly and in a one step process with the need for minimal wet chemistry.

Lastly, co-polymerization of biomolecules (amino acids) and traditional polymers (acrylonitrile, HEMA) has been demonstrated and studied. This is a unique method of integrating biologic and biocompatible materials and helps to create an interfacial film between two dissimilar materials in a facile and stable manner (**Figure #2-2.3**). By studying the chemistry and morphology of these films, it is seen that the two

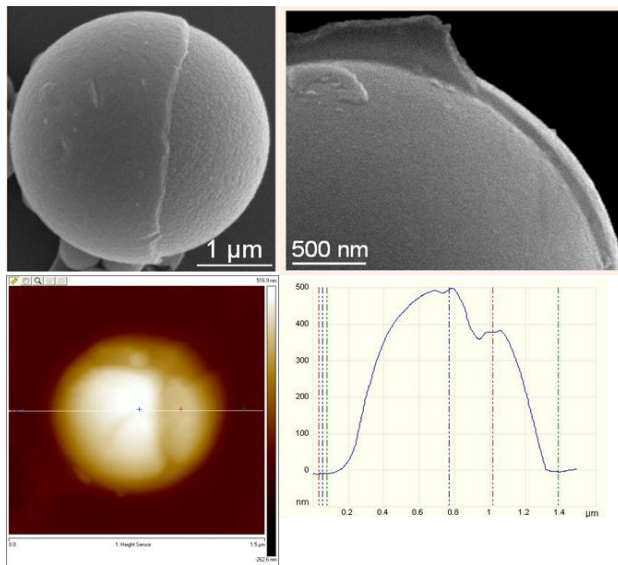


Figure #2-2.2. SEM of plasma coatings of responsive polymer NIPAAm (top left) and HEMA (top right) on silica microspheres. Height of the NIPAAm film is measured at 100 nm by AFM.

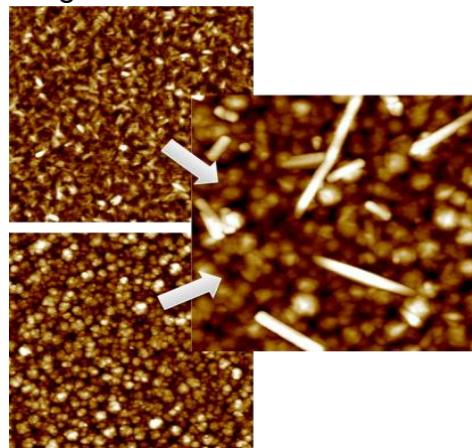


Figure #2-2.3. PECVD of tyrosine (top) and titania (bottom). Copolymerization of the two polymers shows the formation of a unique needle-like structure.

monomer deposit well together into an integrated film showing characteristic of both components as well as indicators of the crosslinking occurring. This demonstrates a very promising technique in the realm of bio applications for PECVD and is deserving of further study as a method to create interfacial coatings which will be capable of integrating biological systems with inorganic ones. In addition to mixed composition bio materials films, free standing plasma deposited films are also being studied. To date free standing films of pNIPAAm and PP-Tyrosine have been observed. Testing is underway to determine the chemical characteristics and responsiveness of these films and also the potential to create bio-material interfacial freestanding films.

Cell Coatings

By eliminating cationic prelayer in polymeric shells, increased viability and unaltered functionality of expressing the biomarker (yEGFP) was achieved. In comparison to cells that have been encapsulated with PEI-primed shells, the viability of cells encapsulated with true hydrogen-bonded shells ranged within 94%-86% depending on number of bilayers applied (**Figure #2-2.4**). In addition to high viability,

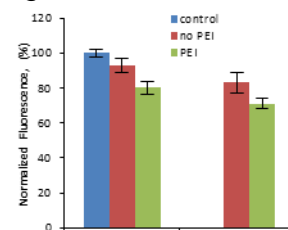


Figure #2-2.4. Viability of cells encapsulated with 2 and 4 bilayers of TA/PVPON

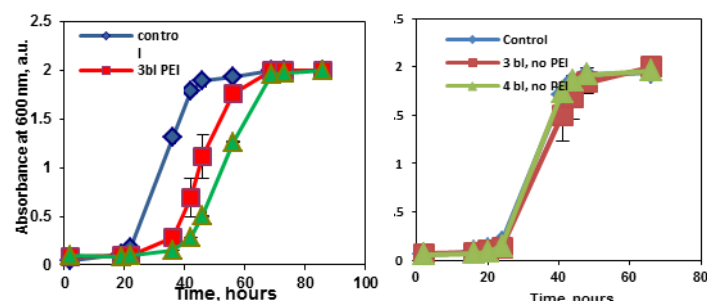


Figure #2-2.5. Growth kinetics of yeast cells encapsulated with 3 and 4 bilayers of TA/PVPON.

the growth kinetics of encapsulated cells with 3 and 4 bilayer structures was matching the growth kinetics of control, non-treated cells, showing no delay in cell reproduction unlike PEI-primed encapsulated cells in which live cycle was delayed by approximately 10 hours with every one bilayer deposited on cell membrane (**Figure #2-2.5**).

Expression of yEGFP was also unaltered reaching the maximum intensity at the middle of log phase. High cyto-compatibility of pure hydrogen-bonded shells versus PEI-primed shells is based on the nature of weak H-bonded interactions capable of easy degradation and 25-30% thinner shells compared to PEI-primed ones.

The other type of reversibly swollen/shrunk artificial membranes based on PMAA (so called elastic bags) was fabricated as the model for providing the storage container for reproducible yeast cells. By adjusting the pH of the solution these elastic bags were expanding in volume by the factor of 30 which might provide necessary space to accommodate several cells within such bag (**Figure #2-2.6**).

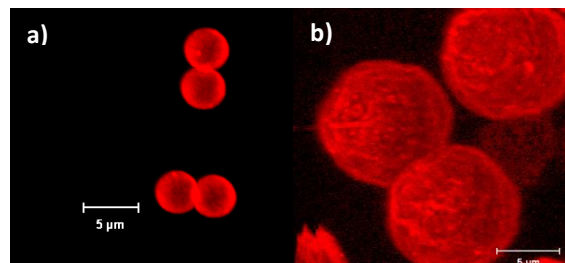


Figure #2-2.6. Reconstructed 3D confocal images of PMAA-co-NH₂ capsules in shrunken (a) and swelled (b) conditions at pH 3.5 and pH 7 respectively.

Formation of model shells produced by layer-by-layer deposition of amine-functionalized polymethacrylic acid (PMAA-co-NH₂) followed by cross-linking with 1-ethyl-3-(dimethylaminopropyl) carbodiimide hydrochloride (EDC) showed ability to create pH-triggered responsive systems with volumetrical, conformational and elastic changes (**Figure #2-2.6**). Below pH 5.5 shells were $\sim 3.5\ \mu\text{m}$ in size, having Young's modulus of $\sim 3.2 \pm 0.8\ \text{MPa}$ and surface potential of $+12 \pm 1.6\ \text{mV}$, whereas above pH 5.5 shells increased in size by more than 300% reaching diameter of $10.5 \pm 0.2\ \mu\text{m}$ with decreased Young's modulus to 20 kPa and switched to the negative value of surface potential to $-68 \pm 1.2\ \text{mV}$. All these changes (decreased stiffness, increased swelling and drop in ζ -potential) are associated with deprotonation of the acidic groups within PMAA polymer chains and repulsive charge-charge interactions that have been balanced by crosslinking points of entanglements. We showed that for stable capsules made from amine-functionalized PMAA (with 17% content of NH₂) capable of high ratio of reversible swelling/shrinking, the maximum number of monomeric units between the crosslinks should not exceed 99. By adjusting incubation time with EDC, the model capsules can reach an expansion ration more than 3 (at neutral pH) compared to the original size (at slightly acidic conditions).

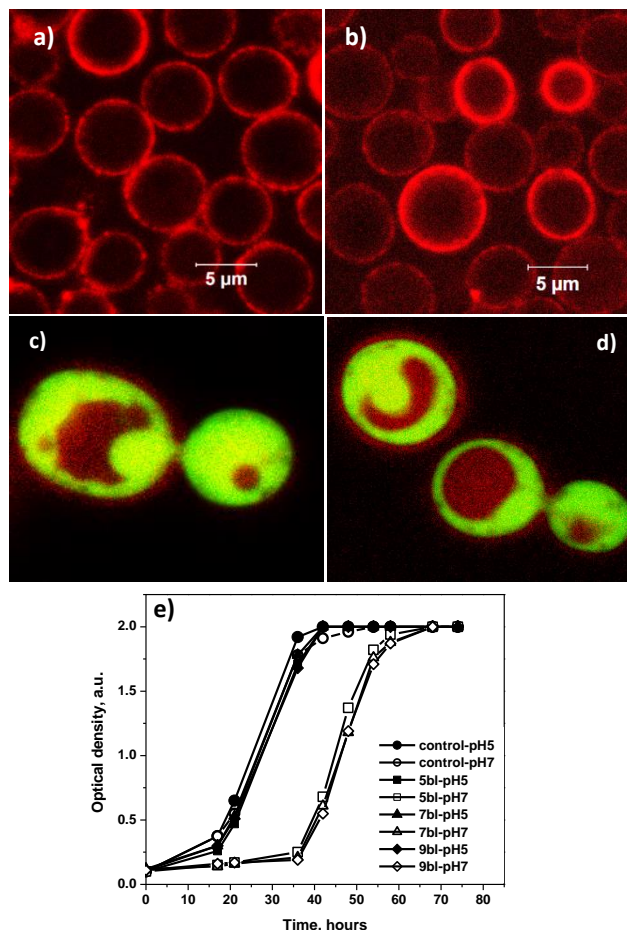


Figure #2-2.7. Confocal images of yeast cells encapsulated in PMAA-co-NH₂ shells and kept at media adjusted to pH 5 (a) and pH 7 (b). Encapsulated yeast cells expressing GFP reporter while being kept in media adjusted to pH 5 (c) and pH 7 (d). Growth kinetics of cells encapsulated with different number of bilayers grown at pH 6 and pH 7 respectively (e).

Yeast cells encapsulated with pH-responsive synthetic nano-shells from crosslinked polymethacrylic acid (PMAA-co-NH₂) showed a high viability rate of 90% indicating high bio-compatibility of the synthetic pH-responsive shells. In comparison to the hollow capsules, shells assembled on cell surfaces were strongly tethered to the membrane proteins during chemical crosslinking and failed to form free-standing elastic bags with change in pH (**Figures #2-2.7a and b**). Polymeric shell did not show any constrain to the cell growth when encapsulated cells were placed at pH 5. In contrary, by keeping encapsulated cells at pH 7, or above of the isoelectric point of the polymer shell, a significant delay in growth

rate has been observed (~22-24 hours) (**Figure #2-2.7e**). However, this delay did not affect the onset of expression of green fluorescent protein (GFP), which indicates intact bio-sensing responsiveness (**Figures #2-2.7c and d**).

Progressive ionization and charge accumulation within the synthetic shells evoked a structural change of the polymer chains leading to the increased shell thickness and shielding of essential nutrients from diffusing through the shell. Another explanation could be associated with repulsive shielding of amino acids by highly negatively charged (-68 mV) polymer shell due to progressive deprotonation of carboxylic groups in PMAA above pH 6. The ability to manipulate perceptible response from the cells by keeping them in “dormant” conditions (constrained replication) for extended time can be rewarding for biosensing applications when the early onset of cell growth can compromise the long-term performance.

We estimated permeability and mechanical properties of LbL capsules assembled from ionomeric silk fibroin as alternative model capsules for responsive shells. At extremely acidic and basic conditions (below pH 2 and above pH 11.5) capsules swell and expand in volume by more than 900%. Accordingly, diffusion coefficients increased by 2 orders of magnitude from 8.5×10^{-12} (between pH 2 and pH 11) to 3.4×10^{-10} (below pH 2) and $1.8 \times 10^{-10} \text{ cm}^2/\text{s}$ (above pH 11.5) (assuming the same composition of capsules) (**Figure #2-2.8**). With increasing number of layers diffusion coefficient also

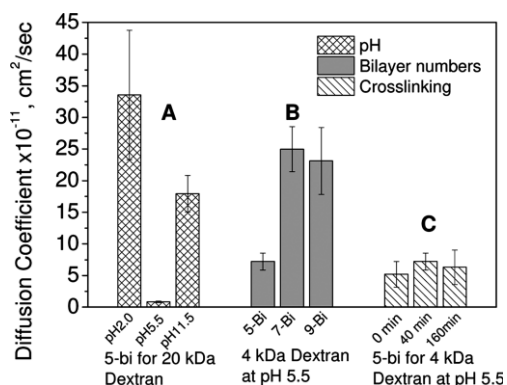


Figure #2-2.8. Diffusion coefficients of silk ionomeric capsules as a function of pH (a), number of bilayers (b) and crosslinking time (c).

softening and swelling of the silk capsules at extremely acidic and basic conditions is associated with balance of protonated and deprotonated carboxyl-terminated groups or amine-terminated groups on the backbone of the silk fibroin.

increased due to weighting of shell thickness from 7.2×10^{-11} to $2.3 \times 10^{-10} \text{ cm}^2/\text{s}$ (**Figure #2-2.8b**). Elastic stiffness of the silk shells was also affected by variations in pH. As was measured by nano-indentation approach using standard AFM probe tips, Young's modulus of silk capsules in liquid state was estimated to be $\sim 6.5 \pm 2 \text{ MPa}$ for pH between 3.5 and 7.5 (**Figure #2-2.9**). Below pH 2 or above pH 9, capsules stiffness decreased to $\sim 0.6 \text{ MPa}$ or $\sim 0.4 \text{ MPa}$ respectively. Increased

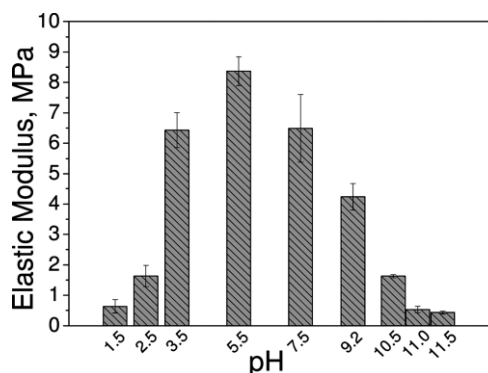


Figure #2-2.9. pH-induced variations of Young's modulus of silk ionomeric capsules.

Interactions with AFRL:

- 10 student internships (K. Anderson, J. Carter, I. Drachuk, M. Gupta, K. Marczewski)
- Regular teleconferences and discussions held with R. Vaia, T. Bunning, R. Naik, L. Drummy, N. Kelley-Loughnane to update on progress, discuss technical issues, and plan future experiments.
- Dr. T. Bunning served as a co-Advisor of the Ph.D. thesis committees of Kyle Anderson and Kamil Marczewski.
- Dr. N. Kelley-Loughnane (AFRL) served as a co-Advisor of the Ph.D. thesis committee of Irina Drachuk.
- Dr. R. Naik served as a co-Advisor of the Ph.D. thesis committee of M Gupta.
- Visits by Dr. J. Chavez, Dr. S. Harbaugh, Dr. R. R. Naik, Dr. T. Bunning of AFRL (Wright-Patterson Air Force Base) to Georgia Tech
- Sabbatical by T. Bunning (AFRL) at Georgia Tech (Jan. to May, 2011)

Manpower Development/Transitions (Former BIONIC Students at AFRL):

- Dr. Michael McConney.(now AFRL staff researcher)
- Dr. Irina Drachuk (Post-Doctoral Fellow in Kelley-Loughnane group)
- Dr. Maneesh Gupta

Publications:

- C. Ye, V. V. Tsukruk, "Materials Springing into Three-dimensional Shape," *Science*, 2015, in print
- R. D. Geryak, V. V. Tsukruk, "Reconfigurable and Actuating Structures from Soft Materials," *Soft Matter*, **10**, 1246-1263 (2014).
- C. Ye, D. D. Kulkarni, H. Dai, V. V. Tsukruk, "Programmable Arrays of "Micro-bubble" Constructs via Self-Encapsulation," *Adv. Funct. Mater.*, **24**, 4364-4373 (2014).
- R. Suntivich, I. Drachuk, R. Calabrese, D. L. Kaplan, V. V. Tsukruk, "Inkjet printing of silk nest arrays for cell hosting," *Biomacromolecules*, **15**, 1428-1435 (2014).
- P. A. Ledin, I. Tkachenko, W. Xu, I. Choi, V. Shevchenko, V. V. Tsukruk, "Star-Shaped Molecules with POSS Core and Azobenzene Dye Arms," *Langmuir*, **30**, 8856-8865 (2014).
- S. Kim, D. Kulkarni, R. Davis, S. Kim, A. Voevodin, S. Jang, V. V. Tsukruk, A. G. Fedorov, "Controlling Physicochemical State of Carbon on Graphene Using Focused Electron Beam Induced Deposition," *ACS Nano*, **8**, 6805-6813 (2014).
- I. Drachuk, M. K. Gupta, V. V. Tsukruk, "Biomimetic coatings to control cellular function through cell surface engineering," *Adv. Funct. Mater.*, **23**, 4437-4453 (2013).
- M. C. Vasudev, K. D. Anderson, V. V. Tsukruk, T. J. Bunning, R. R. Naik, "Exploration of Plasma-Enhanced Chemical Vapor Deposition as a Method for Thin Film Fabrication with Biological Applications," *ACS Appl. Mater. Interfaces*, **5**, 3983-3994 (2013).
- M. K. Gupta, D. D. Kulkarni, R. Geryak, S. Naik, V. V. Tsukruk, "A robust and facile approach to assembling mobile and highly-open unfrustrated triangular lattices from ferromagnetic nanorods." *Nano Lett.*, **13**, 36-42 (2013).
- M. K. Gupta, T. Konig, R. Near, D. Nepal, L. F. Drummy, S. Biswas, S. Naik, R. A. Vaia, M. A. El-Sayed, V. V. Tsukruk, "Surface Assembly and Plasmonic Properties in Strongly Coupled Segmented Gold Nanorods," *Small*, **9**, 2979-2990 (2013).

- Drachuk, I., O. Shchepelina, S. Harbaugh, N. Kelley-Loughnane, M. Stone, V. V. Tsukruk, "Cell Surface Engineering with Edible Protein Nanoshells," *Small*, **9**, 3128-3137 (2013).
- Z. A. Combs, S. T. Malak, T. König, M. A. Mahmoud, J. L. Chávez, M. A. El-Sayed, N. Kelley-Loughnane, V. V. Tsukruk, "Aptamer-Assisted Assembly of Gold Nanoframe Dimers," *Particle*, **30**, 1071-1078 (2013).
- K. D. Anderson, S. L. Young, H. Jiang, R. Jakubiak, T. J. Bunning, R. R. Naik, V. V. Tsukruk, "Plasma Enhanced Co-Polymerization of Amino Acid and Synthetic Monomers," *Langmuir*, **28**, 1833-1845 (2012).
- M. E. McConney, D. Kulkarni, H. Jiang, T. J. Bunning, V. V. Tsukruk, "A New Twist on Scanning Thermal Microscopy," *Nano Lett.*, **12**, 1218-1223 (2012).
- Anderson, D. M.; Gupta, M. K.; Voevodin, A. A.; Hunter, C. N.; Tsukruk, V. V., Fedorov, A. A., "Using Amphiphilic Nanostructures to Enable Long-Range Ensemble Coalescence and Surface Rejuvenation in Dropwise Condensation," *ACS Nano*, **6**, 3262-3268 (2012).
- Drachuk, I.; O. Shchepelina, M. Lisunova, S. Harbaugh, N. Kelley-Loughnane, M. Stone, V. V. Tsukruk, "pH-Responsive LbL Nanoshells for Direct Regulation of Cell Activity," *ACS Nano*, **6**, 4266-4278 (2012).
- B. Wallet, E. Kharlampieva, K. Campbell-Proszowska, V. Kozlovskaya, S. Malak, J. F. Ankner, D. L. Kaplan, V. V. Tsukruk, "Silk Layering as Studied with Neutron Reflectivity," *Langmuir*, **28**, 11481-11489 (2012).
- K. D. Anderson, R. B. Weber, M. E. McConney, H. Jiang, T. J. Bunning, V. V. Tsukruk, "Responsive Plasma Polymerized Ultrathin Nanocomposite Films," *Polymer*, **53**, 4686-4693 (2012).
- S. L. Young, M. Gupta, C. Hanske, A. Fery, T. Scheibel, V. V. Tsukruk, "Utilizing Conformational Changes for Patterning Thin Films of Recombinant Spider Silk Proteins," *Biomacromolecules*, **13**, 3189-3199 (2012).
- V. Kozlovskaya, S. Harbaugh, I. Drachuk, O. Shchepelina, N. Kelley-Loughnane, M. Stone, V. V. Tsukruk, "Hydrogen-bonded Shells for Living Cell Surface Engineering," *Soft Matter*, **7**, 2364-2372 (2011).
- Z. A. Combs, S. Chang, T. Clark, S. Singamaneni, K. D. Anderson, V. V. Tsukruk, "Label-free Raman mapping of surface distribution of protein A and IgG biomolecules," *Langmuir*, **27**, 3198-3205 (2011).
- M. K. Gupta, S. Chang, S. Singamaneni, L. F. Drummy, R. Gunawidjaja, R. R. Naik, V. V. Tsukruk, "pH Triggered SERS via Modulated Plasmonic Coupling in Individual Bimetallic Nanocobs," *Small*, **7**, 1192-1198 (2011).
- J. L. Carter, I. Drachuk, S. Harbaugh, N. Kelley-Loughnane, M. Stone, V. V. Tsukruk, "Truly Non-Ionic Polymer Shells for Encapsulation of Living Cells," *Macromol. Bioscience*, **11**, 1244-1253 (2011).
- Lisunova, M. O., Drachuk, I.; Shchepelina, O. A.; Anderson, K.; Tsukruk, V. V., "Direct probing of micromechanical properties of hydrogen-bonded LbL microcapsule shells with different chemical compositions," *Langmuir*, **2011**, **27**, 11157-11165 (2011).
- Shchepelina, O.; Drachuk, I.; Gupta, M. K.; Lin, J.; Tsukruk, V. V. "Silk-on-Silk LbL Microcapsules," *Adv. Mater.*, **23**, 4655-4660 (2011).

- Kodiyath, R., Wang, J.; Combs, Z. A.; Chang, S.; Gupta, M. K.; Anderson, K. D.; Brown, R. J. C.; Tsukruk, V. V., "SERS Effects in Silver-decorated Cylindrical Nanopores," *Small*, **7**, 3452-3457 (2011).
- C. Ye, O. Shchepelina, R. Calabrese, I. Drachuk, D. L. Kaplan, V. V. Tsukruk, "Robust and Responsive Silk Ionomer Microcapsules," *Biomacromolecules*, **12**, 4319-4325 (2011).
- Stuart, M. C.; Huck, W.; Genzer, J.; Müller, M.; Ober, C.; Stamm, M.; Sukhorukov, G.; Szleifer, I.; Tsukruk, V. V.; Urban, M.; Winnik, F.; Zauscher, S.; Luzinov, I.; Minko, S. "Emerging Applications of Stimuli-responsive Polymer Materials." *Nat. Mater.*, **9**, 101-113 (2010).
- M. E. McConney, S. Singamaneni, V. V. Tsukruk, "Probing Soft Matter with the Atomic Force Microscope: Force-spectroscopy and Beyond," *Polym. Rev.*, **50**, 235-286 (2010).
- M. K. Gupta, S. Singamaneni, M. McConney, L. F. Drummy, R. R. Naik, V. V. Tsukruk, "A Facile Fabrication Strategy for Patterning Protein Chain Conformation in Silk Materials," *Adv. Mater.*, **22**, 115-119 (2010).
- E. Kharlampieva, V. Kozlovskaya, R. Gunawidjaja, V. V. Shevchenko, R. Vaia, R. R. Naik, D. L. Kaplan, V. V. Tsukruk, "Flexible Silk-Inorganic Nanocomposites With Transparent to Mirror-like Optical Properties," *Adv. Funct. Mater.*, **20**, 840-846 (2010).
- E. Kharlampieva, V. Kozlovskaya, O. Zavgorodnya, G. D. Lilly, N. A. Kotov, V. V. Tsukruk, "pH-Responsive Photoluminescent LbL Hydrogels with Confined Quantum Dots," *Soft Matter*, **6**, 800-807 (2010).
- K. D. Anderson, M. Luo, R. Jakubiak, R. R. Naik, T. J. Bunning, V. V. Tsukruk, "Robust Plasma Polymerized-Titania/Silica Janus Microparticles," *Chem Mater.*, **22**, 3259-3264 (2010).
- E. Kharlampieva, C. M. Jung, V. Kozlovskaya, V. V. Tsukruk, "Secondary Structure of silaffin at interfaces and titania formation," *J. Mater. Chem.*, **20**, 5242-5250 (2010).
- K. D. Anderson, K. Marczewski, S. Singamaneni, J. M. Slocik, R. Jakubiak, R. R. Naik, T. J. Bunning, V. V. Tsukruk, "Plasma Amino Acid Coatings for a Conformal Growth of Titania Nanoparticles," *ACS Appl. Mater. Interfaces*, **2**, 2269-2281 (2010).
- E. Kharlampieva, V. Kozlovskaya, B. Wallet, V. V. Shevchenko, R. R. Naik, R. Vaia, D. L. Kaplan, V. V. Tsukruk, "Co-crosslinking silk matrices with silica nanostructures for robust ultrathin nanocomposites," *ACS Nano*, **4**, 7053-7063 (2010).
- M. E. McConney, K. D. Anderson, L. L. Brott, R. R. Naik, V. V. Tsukruk, "Bioinspired Material Approaches to Sensing," *Adv. Funct. Mater.*, **19**, 2527-2544 (2009).
- E. Kharlampieva, V. Kozlovskaya, J. Chan, J. F. Ankner, V. V. Tsukruk, "Spin-Assisted Layer-by-Layer Assembly: Variation of Stratification as Studied with Neutron Reflectivity," *Langmuir*, **25**, 14017-14024 (2009).

Presentations (*invited):

- About 40 presentations at national and international conferences and seminars (ACS, MRS, and others)

Project IRG #2-3: Modeling and Study of Coupling Phenomena and Transient Optical Properties of Organic-Inorganic Adaptive Nanocomposites

Georgia Tech Participants: Project PI: Dr. Mostafa El-Sayed, Students: Chris Tabor (now Dr. Tabor), Rachel Near, J. Bordley, N. Hooshmand

AFRL Collaborators: Dr. Augustine Urbas, Dr. Ruth Pachter

Research Goals:

The goal of project 2-3 was to qualitatively and quantitatively study the plasmonic coupling between nanoparticles in a system composed of either two or more particles and its effect on both optical and electrical field properties of the system.

Key Achievements:

- Design and fabrication of metal nanostructure arrays on silicon nitride membrane substrates using electron beam lithography with precisely controlled shape, spacing and orientation for testing coupling phenomena.
- DDA simulations were carried out to determine the contribution of absorbance to the optical spectra and electric field enhancement of single gold nanorods with varying aspect ratios.
- DDA simulations were carried out in order to determine a theoretical approach for determining the extinction coefficient of gold nanospheres and gold nanorods.
- DDA simulations were carried out to theoretically determine the dependence of the plasmon resonance wavelength and extinction intensity on the aspect ratio and diameter of gold nanorods.
- DDA simulations were carried out to understand the relationship between the optical spectra and electric field enhancement of a random array of gold nanorods with varying aspect ratios. These results will be compared to live cell SERS experiments in order to elucidate the dependence of Raman enhancement on nanorod aspect ratio.
- DDA simulations were carried out to understand the dependence of hot spot formation between a nanocube dimer (Au-Au and Ag-Ag) on the separation distance of the nanocubes.

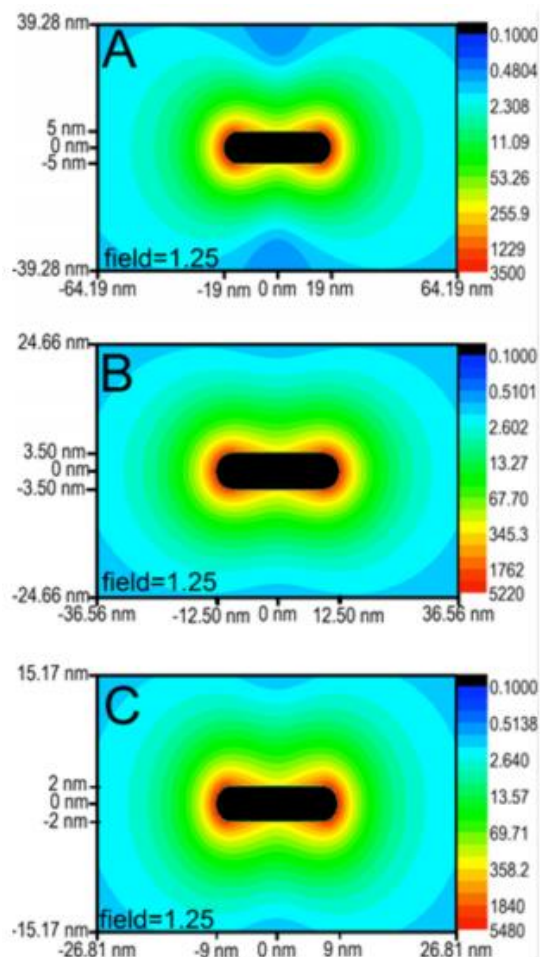


Figure #2-3.1. Field contour plots for the longitudinal mode of the different AuNRs, with particle dimensions indicated and the field decaying to 1.25 at the extremities of each plot. (A) The field maximum of the 38×10 nm AuNR (calculated at 804 nm) is 3500. (B) The field maximum of the 25×7 nm AuNR (calculated at 761 nm) is 5220. (C) The field maximum of the 18×4 nm AuNR (calculated at 875 nm) is 5480.

Approaches and Results:

The extinction spectrum and electric field enhancement was calculated for Au nanorods (AuNR) with varying dimensions (38x10, 25x7, and 18x4nm) in order to correlate the optical spectra and electric field enhancement of these structures to their effectiveness as photothermal contrast agents. Each AuNR was excited off resonance in order to mimic experimental conditions (**Figure #S-3.1**); and interestingly it was found that the effectiveness of a AuNR towards producing heat when excited with light was not related to the maximum electric field enhancement. Instead, when both experimental and theoretical results were combined, it was found that both the absolute electric field enhancement and the distance at which the field begins to decay are important in determining an effective photothermal contrast agent.

A combination of published extinction coefficient values and theoretically determined extinction intensities for Au nanospheres (AuNS) and AuNR were used to derive a novel conversion which can now be used to theoretically determine the extinction coefficients of AuNS and AuNR of any size. **Figure #2-3.2** shows the overlap of the published and theoretically determined extinction coefficients (using our determined conversion) of AuNS and AuNR of various sizes. The general conversion was found to be: $\epsilon_{theoretical} = TEI \times 10^{-24} \times N_A \times f(x)$ where, TEI is the theoretically determined extinction intensity, N_A is Avogadro's number, and $f(x)$ is a shape dependent conversion factor (different for either a sphere or rod).

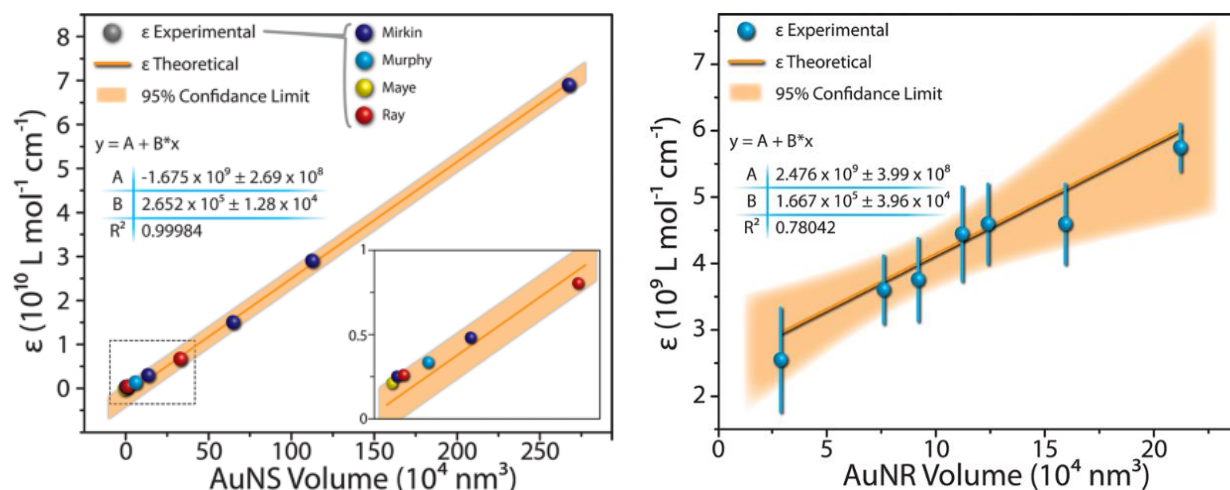


Figure #2-3.2. Plot of ϵ_{theor} against Au nanoparticle volume (orange line) with ϵ_{exper} overlain in spheres. Within error, the experimental data points fall within the relation derived theoretically for both AuNS (left) and AuNR (right), indicating good agreement.

Development of the colloidal synthesis of AuNR has led to an increase in the variety of sizes and aspect ratios available for various applications. As a result, the dependence of the plasmon resonance wavelength and the extinction intensity (of the longitudinal mode) on the particle aspect ratio and volume were thoroughly investigated by DDA. As seen in **Figure #2-3.3**, the extinction spectra of 25 AuNR of varying dimensions were calculated. We found that there was a modified linear relationship between the LSPR peak position and the aspect ratio of the particle. Also, there was a

linear relationship between the particle diameter (particle volume) and the calculated extinction intensity. Thus, the extinction intensity of nanorods at a specific LSPR peak position can be linearly increased simply by increasing the nanorod diameter. This will be highly valuable for future experimental work.

The electric field enhancement for a pair of (Au-Au or Ag-Ag) 42nm cubes was calculated at separation distances of 2, 3, and 4nm. It was found that there is a strong dependence on the location of hot spots in the region between the two cubes of the dimer (**Figure #2-3.4**). Interestingly, it was also shown that when a dimer was excited off resonance there is an indication of mixed plasmonic bands within the extinction spectrum of the dimer (**Figure #2-3.5**). It was found that at short separation distances e.g. 2 nm, high fields and hot spots are formed between the facing facets of the neighboring particles in the dimer. At 3 nm, there is a competition between the formation of hot spots between the centers of the facing facets and between the corners of the adjacent facets. When the separation distance is 4 nm, the high fields are located

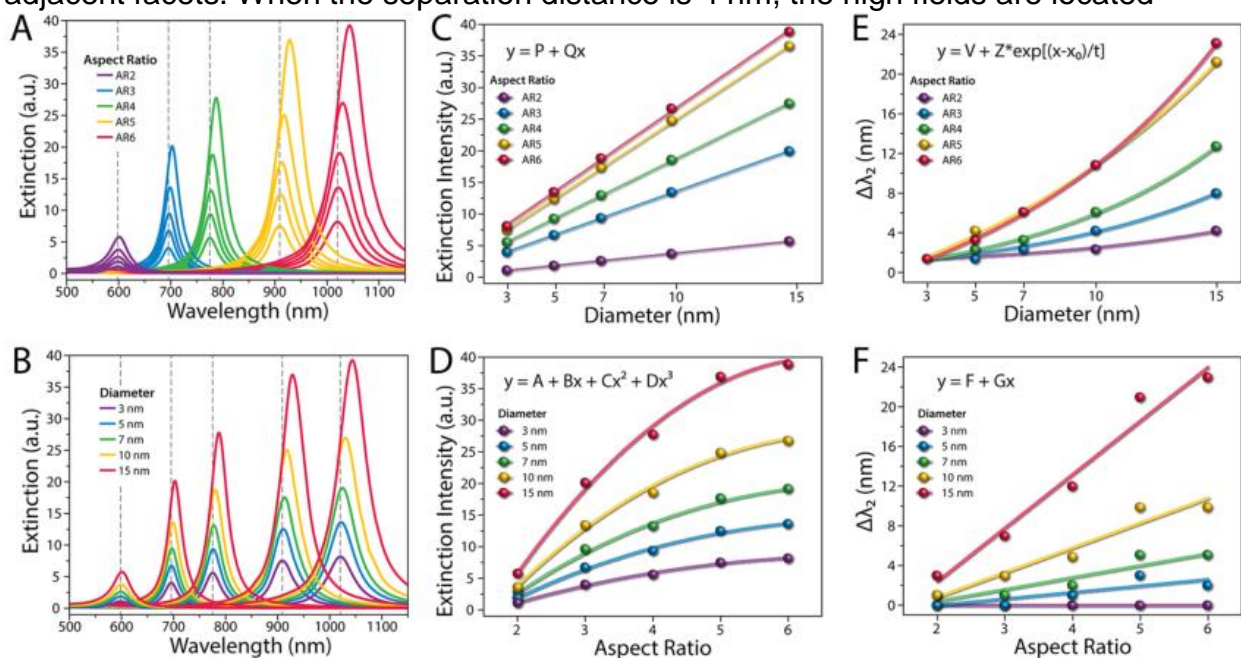


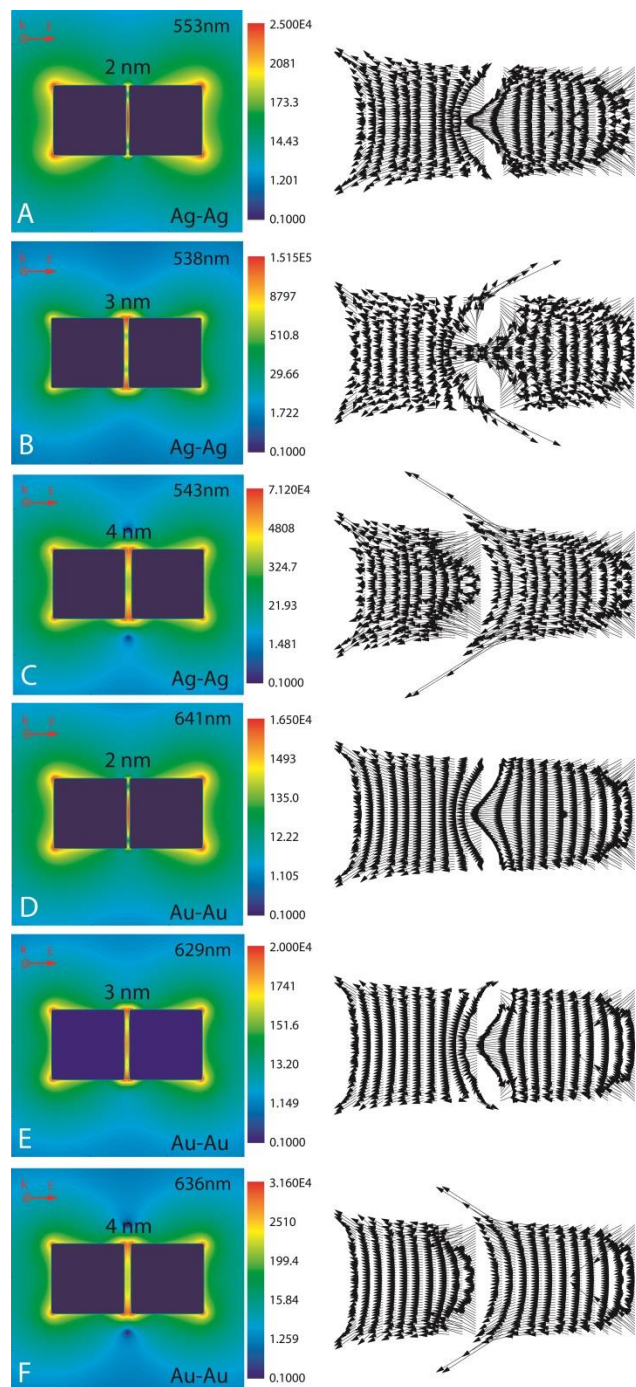
Figure #2-3.3. DDA extinction spectra for 25 individual AuNRs of varying dimensions in water, where the spectra have been grouped by (A) AR and (B) diameter, as indicated by color. Extinction intensity trends (C) linearly with diameter when grouped by AR and (D) cubically with AR when grouped by diameter, emphasizing the role of cubic volume. The change in the longitudinal plasmon wavelength is (E) exponential with diameter when grouped by AR from electromagnetic retardation effects in large nanoparticles and (F) linear with AR when grouped by diameter, indicating a dependence on anisotropy.

mostly around the facing corners. Also, a pure single plasmonic band gives the same structure of the hot spot and is independent of the wavelength used for excitation. Plasmonic bands that show different hot spot structures at different wavelengths must have mixed plasmonic origin.

DDA simulations were carried out in order to elucidate the dependence of live cell SERS on the aspect ratio of AuNR. The novel method used for simulating

nanostructures previously developed by Rachel Near was used to simulate the exact shape and size of colloidal AuNS and three different AuNR with aspect ratios of roughly 2, 3, and 4. The scattering to absorption ratio was calculated for each particle system at varying inter-particle separations (**Figure #2-3.6**) and the electric field enhancement is currently being calculated. Both the scattering to absorption ratio and the electric field enhancement will be used to correlate effective live cell SERS with AuNR aspect ratio.

DDA simulations were carried out in order to elucidate the dependence of live cell SERS on the aspect ratio of AuNR. The novel method used for simulating nanostructures previously developed by Rachel Near was used to simulate the exact shape and size of colloidal AuNS and three different AuNR with aspect ratios of roughly



2, 3, and 4. The scattering to absorption ratio was calculated for each particle system at varying inter-particle separations (**Figure #2-3.6**) and the electric field enhancement is currently being calculated. Both the scattering to absorption ratio and the electric field enhancement will be used to correlate effective live cell SERS with AuNR aspect ratio.

Figure #2-3.4. The effect of increasing the inter-particle separation from 2 nm to 4 nm on the shape and mechanism of hot spot formation for excitation of the lowest energy plasmonic band of Ag-Ag and Au-Au dimers. For both Ag-Ag and Au-Au dimers, formation of hot spots and the overlap of the polarization vector distribution on the facing facets occur at the center of the facing facets (A and D) for short separation distances (2 nm) and at the corners of the facing facets of the dimer (C and F) for the large inter-particle separation of 4 nm. Formation at both the center and the corners seems to take place at the intermediate separation distance of 3 nm (B and E). All results shown are for the top plane of the homo dimer system.

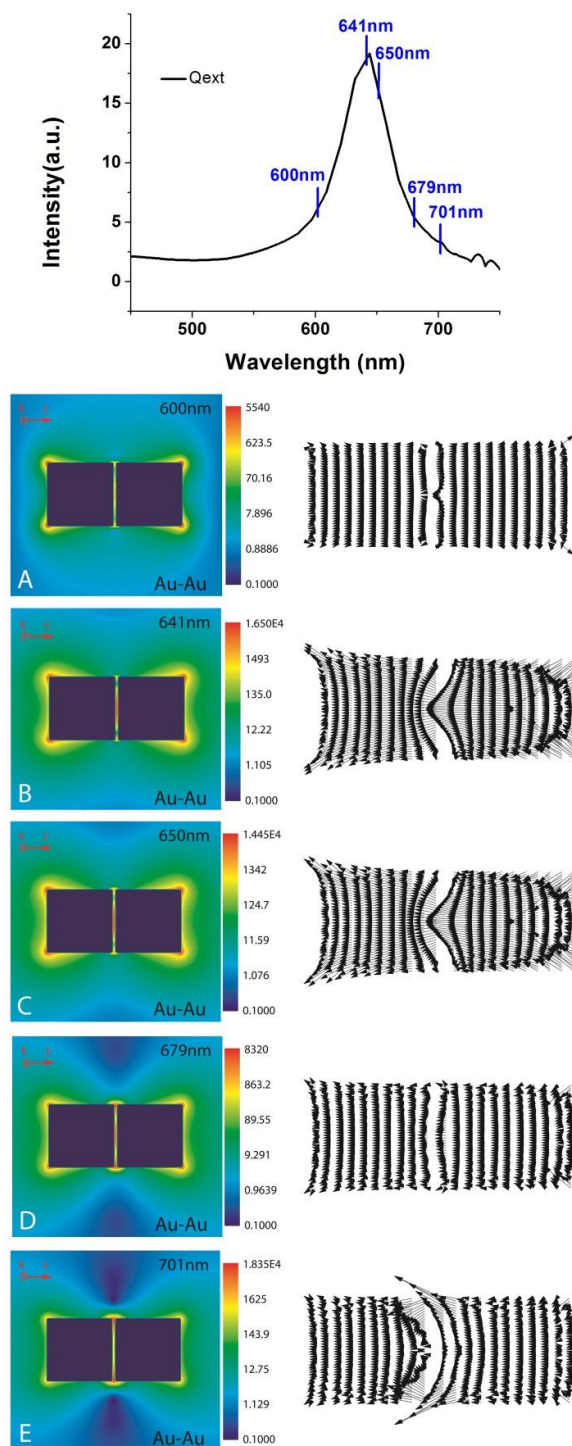


Figure #2-3.5. The change in the shape of the hot spots and the polarization vector distribution with respect to the change in the wavelength of excitation gives an indication of a mixed surface plasmon extinction spectral band.

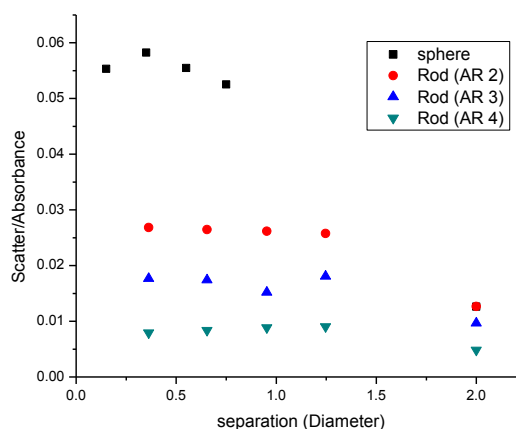


Figure #2-3.6 The ratio of the calculated scattering to absorption intensity as a function of both aspect ratio and separation distance of five randomly oriented AuNS or AuNR. The scattering and absorption spectra was calculated for a Au nanosphere (black) and three Au nanorods with an aspect ratio of 2 (red), 3 (blue), and 4 (green). It is evident that regardless of shape, there is an increase in the scattering to absorption ratio as the particles cluster together.

AFRL/Georgia Tech Interactions:

- Teleconference and electronic correspondence with Augustine Urbas, Ruth Pachter and Chris Tabor.
- Exchange of samples and results with AFRL

Manpower Development/Transitions (Former BIONIC Students at AFRL):

- Dr. Christopher Tabor.

Publications:

- Near, R.; Tabor, C.; Duan, J. S.; Pachter, R.; El-Sayed, M., "Pronounced Effects of anisotropy on Plasmonic Properties of Nanorings Fabricated by Electron Beam Lithography," *Nano Lett.*, **12**, 2158-2164 (2012)
- Near, R.; Hayden, S.; El-Sayed, M., "Extinction vs Absorption: Which is the Indicator of Plasmonic Field Strength for Silver Nanocubes?," *J. Phys. Chem C*, **116** (43), 23019-23026 (2012).
- Near, R; Hayden, SC; El-Sayed, MA. "Thin to Thick, Short to Long: Spectral Properties of Gold Nanorods by Theoretical Modeling," *J. Phys. Chem. C*, **117**, 18653-18656 (2013).
- Hayden, SC; Austin, LA; Near, RD; Ozturk, R; El-Sayed, MA. "Plasmonic Enhancement of Photodynamic Cancer Therapy," *J. Photochem. Photobiol., A*, **269**, 34-41 (2013).
- Near, R; Hayden, SC; Hunter, RE; Thackston, D; El-Sayed, MA. "Rapid and Efficient Prediction of Optical Extinction Coefficients for Gold Nanospheres and Gold Nanorods," *J. Phys. Chem. C*, **117**, 23950-23955 (2013).
- Hooshmand, N; Bordley, JA; El-Sayed, MA. "Are Hot Spots between Two Plasmonic Nanoparticles of Silver or Gold Formed between Adjacent Corners or Facets? A DDA Examination," *J. Phys. Chem. Lett.*, **5** (13), 2229-2234.(2014).
- Makcey, MA; Ali, MRK; Austin, LA; Near, R; El-Sayed, MA, "The Most Effective Gold Nanorod Size for Plasmonic Photothermal Therapy: Theory and In Vitro Experiments," *J. Phys. Chem. B*, **118**, 1319-1326 (2014).
- Malak, ST; Koenig, T; Near, R; Combs, ZA; El-Sayed, MA; Tsukruk, VV, "Stacked Gold Nanorectangles with Higher Order Plasmonic Modes and Top-Down Plasmonic Coupling," *J. Phys. Chem. C*, **118**, 5453-5462 (2014).

Project IRG #2-4: Dynamically Adaptive Hybrid Micro/Nano-structured Surfaces for Critical Thermal and Moisture Management Applications & Graphene Nanoelectronics Platform for Bio-sensing Applications

Project Participants: Project PI: Professor Andrei G. Fedorov; Students: David Anderson, James Silva, Drew Loney, Songkil Kim; Post-docs/Research Scientists: Dr. Peter Kottke (Senior Research Engineer, School of Mechanical Engineering, US Citizen).

Air Force Collaborators: WPAFB: Dr. Andrey Voevodin, Dr. Rajesh Naik (AFRL)

University Collaborators: Prof. Vladimir Tsukruk

Research Goals:

- Development of self-assembled amphiphilic (*i.e.*, mixed hydrophilic-hydrophobic) nano-interfaces, including hybrid (bio)organic-inorganic surfaces, for moisture management including controlled wetting/de-wetting and fully passive motion of droplets and thin liquid films.
- Environmental scanning electron microscopy (ESEM) characterization of surface wetting of engineered interfaces on the nano/microscale, including dynamic aspects in response to thermo-mechanical stimuli.
- Development of a new approach for Focused Electron Beam Induced Processing (FEBIP) of metal-graphene contact interfaces via formation of a graphitic interlayer, which is instrumental to making the low-resistance Ohmic electrical contacts to graphene-based nanoelectronic devices.
- Development of a methodology for forming the microscopic poly(*N*-isopropylacrylamide) (PNIPAM) hydrogel films confined within microcapillaries, which enabled a gated control of fluid flow in response to environmental temperature/moisture changes for applications for smart microfluidic devices for biosensing.

Key Achievements:

- Performed ESEM experiments which clearly established the development of a liquid sublayer in the hydrophilic region of an amphiphilic nanowire array and proposed a new mechanism of droplet coalescence.
- Developed a transport model based on proposed coalescence mechanism to design a surface which utilizes this phenomenon to promote fully passive motion of thin liquid film.
- Utilized ESEM imaging capability to collaborate with IRG1 researchers assessing the impact of surface wettability on the osseo-integration of titanium implants.
- Developed the fabrication protocol for making 3-D, topologically-complex arrays of twisting nano-structures in silicon using metal-assisted chemical etching (MaCE) as a novel substrate for moisture management on nanoscale.
- Developed a new method for Focused Electron Beam Induced Processing (FEBIP) of metal-graphene contact interfaces via formation of a graphitic interlayer, which is instrumental to making the low-resistance Ohmic electrical contacts to graphene-based nanoelectronic devices.

- Performed comprehensive characterization and optimization of different graphene transfer techniques from the fabrication (copper) substrate to device (Si/SiO₂) support, focusing on achieving the highest quality, pristine graphene films via minimization of defects/cracks, wrinkles/folding and residual PMMA associated with the transfer process.
- Developed a methodology for forming the microscopic poly(*N*-isopropylacrylamide) (PNIPAM) hydrogel films confined within microcapillaries, which enabled a gated control of fluid flow in response to environmental temperature/moisture changes.
- Developed a theoretical framework based on the Biot's theory of poroelasticity for predicting the dynamics of PNIPAM swelling in a confined micro/nanofluidic environment, including comparison with experiments.
- Developed a novel scalable procedure for fabricating nanostructured PNIPAM surfaces via porous alumina sacrificial templates and theoretically predicted its behavior to amplify the natural hydrophilicity from the hydrophilic state when PNIPAM is below its lower critical solution temperature (LCST) to the hydrophobic state at temperatures above LCST.

Approaches and Results:

Amphiphilic Nanostructures for Condensation Control.

Amphiphilic closely-packed vertically aligned nanowires were fabricated and tested for moisture management applications, including preferential droplet nucleation and collective non-direct contact coalescence over large droplet ensembles. The nanowire arrays, consisting of intrinsically hydrophilic gold with tips coated by a hydrophobic fluoropolymer, exhibited long-range multi-droplet coalescence events which continually freed up surface area for the highly efficient droplet nucleation/early growth stages during moisture condensation.

Additional ESEM experiments performed this year suggest that the long-range coalescences are induced by the existence of a liquid sublayer located in the hydrophilic regions of the nanowires that fluidically links the individual droplets on top of the surface. **Figure #2-4.1** shows the development of the wetted sublayer due to preferential nucleation in the hydrophilic region, followed by emergence of droplets which are initially suspended on the nanowire tips but eventually become connected to the sublayer due to perturbation during coalescence. These observations, in concert with macro-scale condensation experiments, allow us to propose a mechanism of

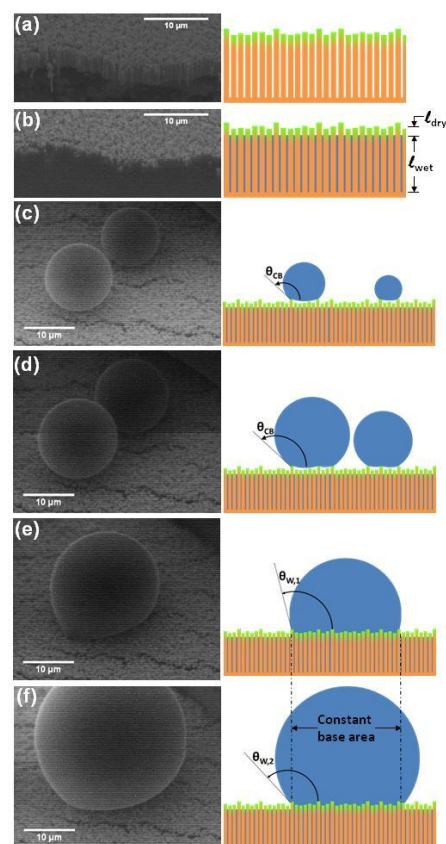


Figure #2-4.1. ESEM images of condensation wetting stages. (a) Dry amphiphilic surface. (b) Subcooling leads to nucleation at base. (c) Formation and (d) constant contact angle growth of Cassie droplets suspended on the nanowire tips. (e) Contact-based coalescence of Cassie drops. (f) Growth of resulting Wenzel drop connected to the wetted layer.

coalescence driven by the difference in Laplace pressure between adjacent droplets of different radii of curvature. This proposed mechanism is shown schematically in **Figure #2-4.2**.

An investigation into alternative amphiphilic surfaces was commenced based on insights gained from the amphiphilic closely-packed vertically aligned nanowires study. This investigation embodies a more general approach to minimizing liquid conduction thermal resistance in condensation by developing surfaces which passively remove condensed liquid from the heat transfer surface, thus minimizing the length of the thermal conduction path. Our strategy is still broadly one of passive control of liquid behavior using surfaces exploiting interconnected hydrophilic sublayers adjacent to the substrate, topped by hydrophobic superstructures. Now, however, we are developing surfaces in which well-defined liquid collection lanes act as a reservoir for the pumped away liquid. This is in contrast with a mainstream approach of relying on dropwise condensation. The first such conceptualization, based on exploiting induced Laplace pressure gradients to control liquid film thickness, uses a close-packed array of hydrophobic microspheres on a hydrophilic substrate (**Figure #2-4.3**).

We have developed a theoretical model describing the condensation process on these surfaces, which enables prediction of effects of surface energy and feature geometries on obtainable condensation rates. This description, based on an integral form of equations enforcing mass, momentum and energy conservation, enables improved surface design and yields a better understanding of the process in general. A key insight gained from the model is that as microsphere size increases, although maximum capillary pressure drops, flow resistance drops more rapidly, enabling larger inter-reservoir spacing. However, the film thermal resistance increases with microsphere size also, thus a tradeoff exists. The model guides design in that it enables setting a target condensation rate, and

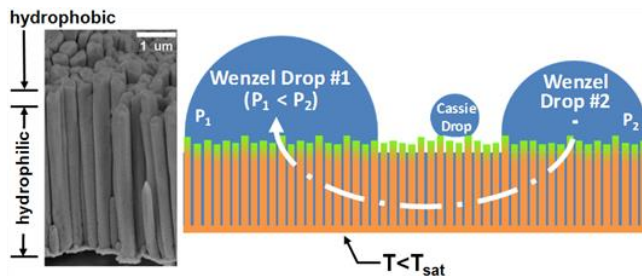


Figure #2-4.2. Proposed mechanism of long-range coalescence between adjacent droplets.

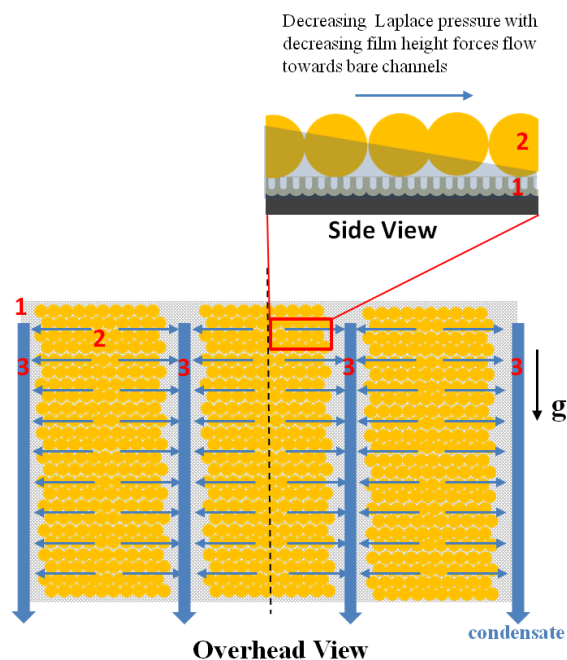


Figure #2-4.3. Schematic depiction of the strategy of patterned microstructured amphiphilic surfaces for condensation enhancement. The strategy is based on surfaces that have (1) an underlying hydrophilic substrate with low energy barrier for nucleation and high roughness, (2) a hydrophobic or amphiphilic superstructure consisting of tightly packed spheres, and (3) regularly spaced reservoirs for liquid collection and removal.

obtaining maximum allowable microsphere diameter, and hence also reservoir spacing.

We are developing an experimental demonstration capability in order to validate the concept depicted schematically in **Figure #2-4.3**. The *sine qua non* of the approach is controlled deposition of a close packed monolayer of spheres on selected areas of a surface. We are currently optimizing a methodology based on electrophoretically induced self-assembly of colloidal crystals in a monolayer on patterned substrates (**Figure #2-4.4**).

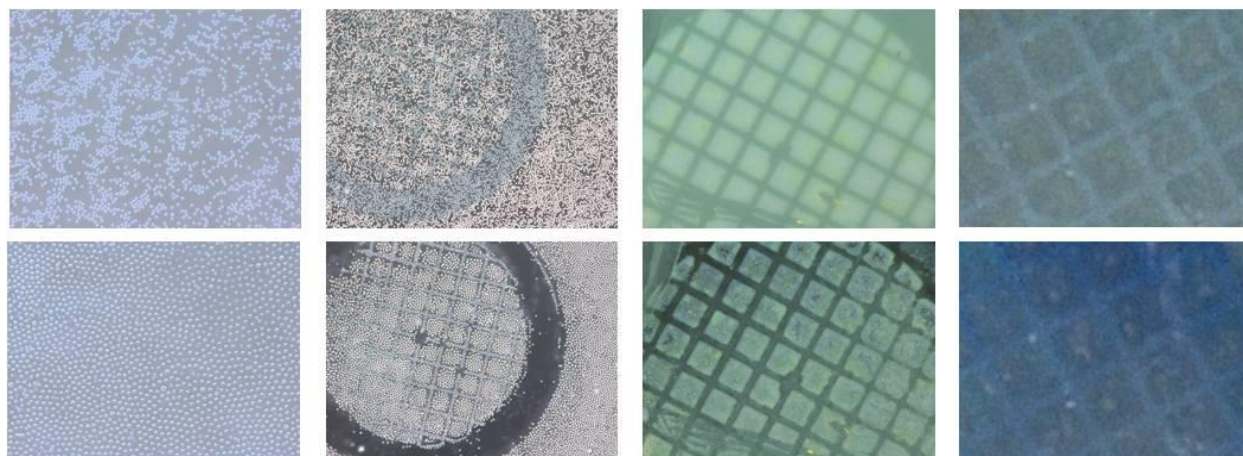


Figure #2-4.4 Progress towards fabrication of patterned amphiphilic surfaces using electrophoretic deposition of microspheres. The top row for each pair of images is prior to electrophoretic assembly. The left most panel shows a solution of 20 micron diameter spheres which are caused to assemble into a hexagonal nearly close packed monolayer on an indium tin oxide substrate. In the second panel, the deposition is spatially controlled by first patterning the substrate with a gold layer through a TEM grid mask. In the third panel, the spatial control is demonstrated with 1.8 micron diameter silica particles, and in the last panel, evidence of the success of efforts to improve the quality of the colloidal assembly with submicron silica particles is the resulting blue color due to diffraction in a close packed ordered monolayer.

Condensation of water vapor with microscale ESEM resolution was also utilized to better characterize the impact of wettability on osseointegration of titanium implants with different surface topographies. The results of this work are shown in **Figure #2-4.5**. Sandblasted-large-grit-acid-etched (SLA) surfaces with microscale roughness and nano-modified SLA (NMSLA) surfaces were initially shown to be hydrophobic using the sessile drop technique, with contact angles of 157° and 131° , respectively. Condensed droplets, however, studied with microscale resolution in the ESEM, exhibited hydrophilic behavior with droplets having contact angles less than 50° on both the SLA and NMSLA surfaces. The ESEM condensation results suggest that the

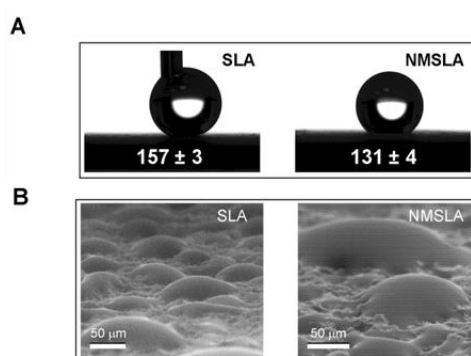


Figure #2-4.5. Wettability of titanium implants shown by the (a) sessile drop technique and (b) ESEM condensation experiments.

titanium implants are not truly hydrophobic, as was previously thought; rather, the hydrophobic behavior displayed by the deposited droplets is caused by trapped air between the roughness features. Condensed droplets nucleate at a length scale smaller than the surface roughness, and as such are able to fill in the space between roughness features and create a homogeneous interface between the liquid droplet and the surface.

“Smart” Microfluidics via Stimuli-Responsive Hydrogel Coated Microcapillaries

Hydrogels are cross-linked polymer networks capable of imbibing and releasing anywhere from 2 to 500 times their weight in water, and these materials have become ubiquitous across a wide range of research applications including drug delivery, microfluidics, and agriculture. Understanding hydrogel surface properties has important implications to interface manipulation with implication to control of fluid behavior. In particular interest to microfluidic applications, hydrogel wettability changes due to swelling and interactions with aqueous solutions, and can be modulated by external stimuli in the case of smart polymer hydrogels.

We have developed a novel process for making hydrogel coated glass capillaries to explore the opportunities for dynamic flow control by external stimuli. By controlling the amount of NIPAM in the stock solution, it is possible to control the thickness of the resultant polymer layer coating (**Figures #2-4.6a-d**). For polymer layers synthesized in 750 μm ID capillaries with equivalent amounts of MBA and TEMED, precursor solution with 1.93 g NIPAM gives a coating thickness of $42 \pm 8 \mu\text{m}$ (**Figure #2-4.6a**), while solution with 0.59g NIPAM gives $13 \pm 2 \mu\text{m}$ (**Figure #2-4.6c**). Film thickness measurements were taken for multiple samples, and error is reported with a 95% confidence interval. While thinner coatings (10-20 μm) synthesized per this procedure take only 1-2 seconds to reach equilibrium (**Figure #2-4.6b**), they do not completely fill the capillary cross-section in their swollen state. Thicker coating (40-50 μm), however, takes a longer time to reach equilibrium (~ 30 s), by completely seal the capillary (**Figure #2-4.6d**). Thus, hydrogel thickness could be tuned to meet the needs of a target application. Using optical visualization of water penetration into the hydrogel-coated capillaries (**Figure #2-4.6e**), we have discovered a novel stick-slip behaviour during capillary-pressure driven filling of hydrogel coated micro capillaries (**Figure #2-4.6f**). As a result of complex interactions resulting from mass exchange between the water/gas/hydrogel at their contact line, water penetration into glass capillaries coated with hydrogel (poly(*N*-isopropylacrylamide, i.e., PNIPAM) layers synthesized along the inner diameter takes 1000 times longer than the time for water to wick through the same length of bare capillary. In this work, we experimentally demonstrate how contact line phenomena on the swelling hydrogel surface results in “stop-and-go” motion during capillary pressure driven flow. We developed a theoretical framework to model the pinning and unpinning of the contact line, the dynamics of which determines the rate of liquid filling, and used complementary first-principles analysis to successfully predict the time required for water to penetrate hydrogel-coated micro capillaries. Collectively, these fabrication, experimental characterization and modelling tools provide unique capabilities for design of

“smart” microfluidic structures and devices, which are especially useful for lab-on-a-chip biochemical analysis applications.

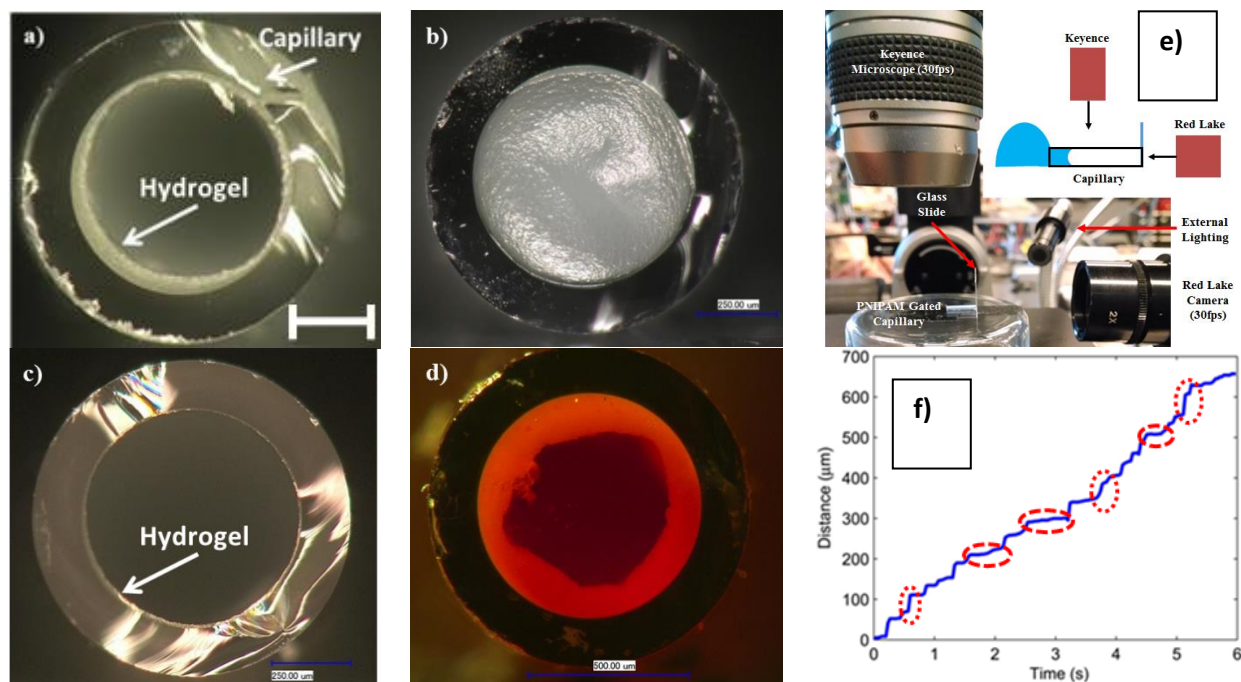


Figure #2-4.6. 750 μm ID capillary with 42±8 μm coating of PNIPAM hydrogel (a) swells to fill the capillary cross-section (b), while a 13±2 μm coating (c) swells to only partially seal the cross-section (d). Scale bar in a) indicates 250 μm for all figures. Hydrogel in d) appears red due to added coloring from food dye to improve contrast. (e) Experimental setup for simultaneous capture of meniscus position and swelling kinetics during capillary filling. (f) Meniscus profile at 200x magnification for a 750 μm ID gated capillary. Stick periods (long dashes) and slip periods (short dashes) are indicated.

Graphene Nanoelectronics Platform Development Using Focused Electron Beam Deposition

Focused electron beam induced processing (FEBIP), a resist-free nanomanufacturing technique, is an emerging method for “direct-write” processing of a wide range of structural and functional nanomaterials, with pattern resolution of ~2-3 nanometers and high degree of spatial and time-domain control down to sub-nanometer scale for atomically-thin suspended substrates. Among FEBIP methods, the electron beam induced deposition (EBID) has some unique aspects that are fundamentally not possible to accomplish using any other conventional fabrication and materials processing techniques, especially when dealing with interfaces between compositionally and structurally dissimilar materials. In particular, an ability to modify the “buried” interfaces, which are externally inaccessible, via the penetrating electrons of appropriately tuned beam energy, to form the imbedded atomically-thin deposits acting as an interfacial “molecular glue” with tunable electrical/thermal/mechanical properties (e.g., poorly conducting but highly compliant amorphous carbon vs. graphitic carbon with its superior electrical and thermal conductivity) provide intriguing opportunities to

enable unique applications for functional nano-electro-mechanical systems and devices and hybrid integration of dissimilar materials.

The fabrication protocols for two graphene device structures are shown in **Figure #2-4.7**. In both cases, at the targeted graphene regions (red box), metal electrodes were fabricated using e-beam lithography followed by Au(20 nm)/Cr(10 nm) deposition and lift-off procedure (this is the conventional approach to making graphene-metal contact, and will be referred to as “standard contact” in subsequent electrical characterization plots shown in **Figure #2-4.8**). An AFM image shows formation of the FEBIP carbon interface to mechanically exfoliated multilayer graphene with thickness of ~7 nm, corresponding to ~21 layers of graphene. **Figure #2-4.7a** shows the fabrication protocol of a graphene-metal interconnect with ‘post-deposited’ FEBIP interlayer. In this case, after fabrication of metal electrodes, the focused electron beam with spot size 3(~ 30 pA) and beam energy of 25 keV was exposed on top of graphene-metal contact areas, which resulted in partial penetration of electrons through metal layer with carefully optimized energy loss to achieve a desired ~10-100eV level required for forming an atomically thin FEBIP carbon interlayer (molecular glue!) using e-beam activated decomposition of entrapped hydrocarbon contaminations as precursor molecules.

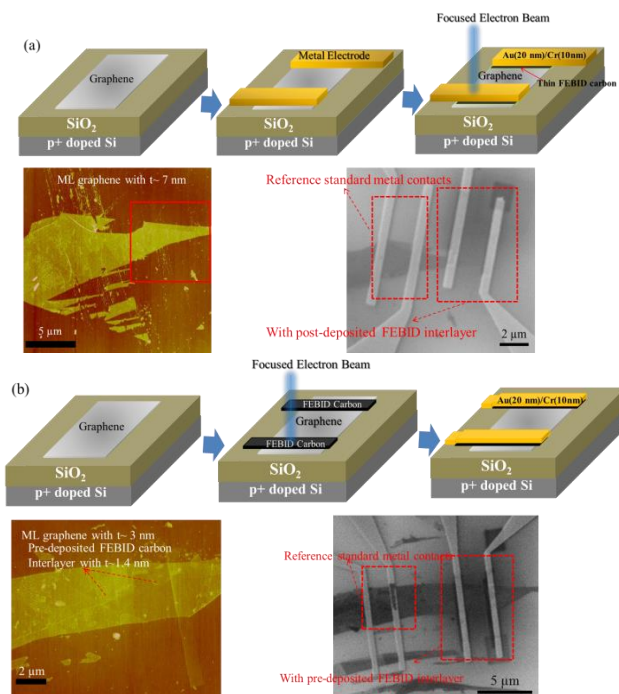


Figure #2-4.7. Schematics and the corresponding AFM and SEM images for mechanically exfoliated multilayer (ML) graphene devices with (a) post-deposited “interlayer”/molecular glue and (b) pre-deposited FEBIP coupling carbon film, aiming to improve intrinsic interfacial properties at the graphene-metal contacts.

For comparison purposed, an alternative device structure described in **Figure #2-4.7b** was fabricated by firstly depositing a thin (but not atomically thin!) FEBIP carbon coupling layer (thickness~1.4 nm) on graphene (thickness~3 nm) followed by Au (20 nm)/Cr (10 nm) deposition on top of FEBIP carbon layer. While a complete, uniform surface coverage with FEBIP carbon layer can be guaranteed in this device structure,

interfacial binding between graphene and metal (through deposited carbon film) is expected to be worse than that for a ‘post-deposited’ FEBIP interlayer in the device structure shown in **Figure #2-4.7a**. This is because metal deposition on a ‘pre-deposited’ FEBIP coupling layer would result in a weak binding (physical interaction) similar to the standard metal contact to graphene (confirmed via DFT). In order to enhance the interfacial property between FEBIP carbon layer and metal, we scanned the top of metal-FEBIP interlayer-graphene contact areas by the focused electron beam, attempting to improve interfacial binding similar to the device structure with the “post-deposited” carbon interlayer/molecular glue. Lastly, for each graphene sample, reference “standard” metal contacts were also fabricated for side-by-side comparison of electrical performance. For all devices, thermal annealing in vacuum was performed to access its impact on interface stability and improvement of electrical properties (e.g., contact resistance and linearity of response/Ohmic behavior).

Figure #2-4.8 shows the source-to-drain two-terminal electrical I_{ds} - V_{ds} measurements for all devices at zero back-gate voltage. **Figures #2-4.8a and b** are for the devices with post-deposited and pre-deposited FEBIP carbon interlayer, respectively, while **Figures #2-4.8c and d** are for the devices with a “standard metal” contact only for comparison. Focused electron beam scanning over the metal contact area, hereafter defined as “post-deposition” FEBIP interlayer (molecular glue), improved the electrical conductivity of a device with the pre-deposited FEBIP carbon layer (**Figure #2-4.8b**), while it does not appear to make any significant contribution to the device with the “post-deposited” FEBIP interlayer (**Figure #2-4.8a**). As expected, one finds that the devices with “pre-deposited” FEBIP carbon coupling layers exhibit an improved electrical conductivity upon thermal annealing in vacuum due to graphitization of as-deposited amorphous carbon film. However, for the devices with “post-deposited” atomically-thin molecular glue carbon interlayer, additional thermal annealing has little effect on electrical performance, likely due to the fact that as-deposited the carbon “interlayer” immediately assumes a thermodynamically stable nanocrystalline graphitic arrangement due to atomically-confined deposition zone at the interface between the metal and graphene. On the other hand, annealing of “standard” metal contacts does degrade performance (**Figures #2-4.8c and d**), due to interfacial breakdown.

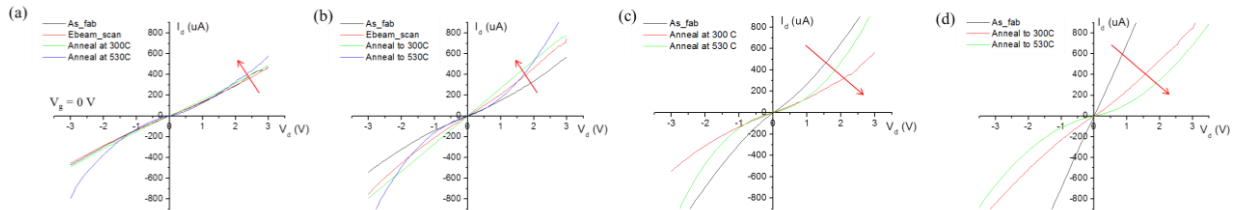


Figure #2-4.8. Electrical measurements for devices with (a) post-deposited FEBIP carbon ‘interlayer’/molecular glue, (b) pre-deposited FEBIP carbon coupling ‘layer’, (c) and (d) “standard” metal contacts only. All measurements were performed at $V_g=0V$ using two-terminal method, and thermal annealing was performed in vacuum, $P\sim 10^{-5}$ Torr.

AFRL/Georgia Tech Interactions:

- one student internship in the Summer of 2012.

Manpower Development/Transitions (Former BIONIC Students at AFRL):

- None.

Publications:

- Anderson, D.M., Gupta, M.K., Voevodin, A.A., Hunter, C.N., Putnam, S.A., Tsukruk, V.V., Fedorov, A.G., "Using amphiphilic nanostructures to enable long-range ensemble coalescence and surface rejuvenation in dropwise condensation," *ACS Nano*, **6** (4), 3262-3268 (2012).
- Gittens, R.A., Olivares-Navarrete, R., Cheng, A., Anderson, D., McLachlan, T., Stephan, I., Fedorov, A., Rupp, F., Geis-Gerstorfer, J., Sandhage, K.H., Boyan, B.D., Schwartz, Z., "The role of titanium surface micro/nanotopography and wettability on the differential response of human osteoblast lineage cells," *Acta Biomater.*, **9**, 6268-6277 (2013).
- Hildreth, O., Rykaczewski, K., Fedorov, A., Wong, C. P., "A DLVO model for catalyst motion in Metal-assisted Chemical Etching based upon controlled out-of-plane rotational etching and force-displacement measurements," *Nanoscale*, **5**, 961-970 (2013).
- Hildreth, O., Fedorov, A., Wong, C. P., "3-D spirals with controlled chirality fabricated using metal-assisted chemical etching of silicon," *ACS Nano*, **6** (11), 10004-10012 (2012).
- Fedorov, A., Kim, S., Henry, M., Kulkarni, D., Tsukruk, V. V., "Focused electron beam induced processing (FEBIP) for emerging applications in carbon nanoelectronics," *Appl. Phys. A – Mat. Sci. & Proc.*, **117** (4), 1659-1674 (2014) **invited**.
- Kim, S., Kulkarni, D., Davis, M., Kim, S., Naik, R., Voevodin, A. A., Jang, S., Tsukruk, V. V. Fedorov, A., "Controlling physicochemical state of carbon on graphene using Focused Electron Beam Induced Deposition," *ACS Nano*, **8** (7), 6805–6813 (2014).
- Kim, S., Russell, M., Henry, M., Kim, S., Naik, R., Voevodin, A. A., Jang, S., Tsukruk, V. V. Fedorov, A., "Controlling local electronic properties of graphene by carbon doping using Focused Electron Beam Induced Deposition," *Phys. Rev. Lett.*, in review (November 2014).
- Kim, S., Kulkarni, D., Henry, M., Jang, S., Tsukruk, V. V. Fedorov, A., "New route to reduction of graphene oxide using Focused Electron Beam Induced Deposition," *Appl. Phys. Lett.*, in preparation (December 2014).
- Silva, J., Geryak, R., Loney, D., Kottke, P.A., Naik, R., Voevodin, Tsukruk, V. V., Fedorov, A., "Stick-slip water penetration into capillaries coated with swelling hydrogel," *Soft Matter*, in preparation (December 2014).

Presentations:

- Anderson, D.M., Gupta, M.K., Voevodin, A.A., Hunter, C.N., Putnam, S.A., Tsukruk, V.V., and Fedorov, A.G., Controlling water condensation in energy systems using nanostructured surfaces. *4th International Forum on Multidisciplinary Research and Education in Energy Sciences*, Honolulu, HI, December 17-22, 2011 (**best presentation award**).

- Anderson, D.M., Gupta, M.K., Voevodin, A.A., Hunter, C.N., Putnam, S.A., Tsukruk, V.V., and Fedorov, A.G., Mechanisms of condensation on amphiphilic nanostructured surfaces. *3rd ASME Micro/Nanoscale Heat & Mass Transfer International Conference*, Atlanta, GA, March 3-6, 2012.
- Kottke, P.A., Anderson, D.M., and Fedorov, A., Condensation enhancement with micro- and nano-structured amphiphilic surfaces, *2012 Power MEMS workshop*, Atlanta, GA, December 2-5, 2012.
- Kottke, P.A., Fedorov, A.G., Thin film evaporative cooling of hot spots, *2013 Power MEMS workshop*, London, UK, December 3-6, 2013.
- Silva, J., Geryak, R., Kottke, P.A., Anderson, D.M., Tsukruk, V. V., Naik, R. and Fedorov, A., "Thermomechanical behavior of a constrained gel interface for heat and moisture management," *International Mechanical Engineering Congress & Exposition IMECE'13*, San Diego, CA, November 15-21, 2013.
- Fedorov, A., Exploiting Nanoscale Confinement for Design of Optimal Evaporation/Condensation Interface, *Invited seminar at the Department of Mechanical Engineering, University of Nevada*, Las Vegas, USA (September 23, 2013).
- Fedorov, A., Focused Electron Beam Induced Processing (FEBIP) for Emerging Carbon-Based Electronic Nanomaterials. *Invited presentation at the Intel/SRC Symposium and Executive Review*, Hillsboro, Oregon, USA (September 5, 2013).
- Fedorov, A., Thin Film Evaporation – Overview: Focusing on Micro/Nano Structures for Phase-Change Heat Transfer. *Invited lecture at the NSF/DARPA/ONR/ARPA-E International Workshop on "Micro and Nano Structures for Phase Change Heat Transfer"*, MIT, Boston, Massachusetts, USA (April 22-23, 2013).
- Kim, S., Kulkarni, D., David, R., Henry, M., Voevodin, A. A., Kim, S., Pacley, S., Jang, S., Tsukruk, V. V., and Fedorov, A., Engineering graphene-metal interface with Focused Electron Beam Induced Deposition (FEBID) of graphitic nanojoints, *Materials Research Society (MRS) Spring 2014 Meeting*, San Francisco, California, April 21-25, 2014.
- Kim, S., Russell, M., Kulkarni, D., Chyasnavichyus, M., Henry, M., Kim, S., Naik, R., Voevodin, A. A., Jang, S., Tsukruk, V. V., and Fedorov, A., Enhanced interfacial properties of graphene-metal junctions with Focused Electron Beam Induced Deposition (FEBID) of graphitic interlayer, *Materials Research Society (MRS) Spring 2015 Meeting*, San Francisco, California, April 6-10, 2015.
- Silva, J., Geryak, R., Kottke, P.A., Naik, R., Voevodin, Tsukruk, V. V., and Fedorov, A., Unusual stick-slip contact line motion in PNIPAM gated micro capillaries for lab-on-a-chip applications, *Materials Research Society (MRS) Spring 2015 Meeting*, San Francisco, California, April 6-10, 2015.

Seed Grant #1: Novel Organic-Inorganic Nanocomposites Composed of Magnetic Nano-Particles Intimately and Permanently Connected with Nematic Liquid Crystal Hosts and Chiral Azo Dopants

Project Participants: Project PI: Professor Zhiquan Lin; Students: James Iocozzia

Air Force Collaborators: WPAFB: Dr. Timothy Bunning, Dr. Timothy White

Research Goals:

- Synthesize liquid crystal-like small molecule capping species end-functionalized with alkyne functional group
- Synthesize star-like poly(acrylic acid)-b-polystyrene block copolymer template based on β -cyclodextrin end-functionalized with azide functional group
- synthesize inorganic core in inner block of template
- Characterize click-functionality, solubility in liquid crystal media (5CB)
- Characterize water soluble poly(ethylene oxide) capped gold nanoparticles
- Model plasmonic properties of gold nanoparticles

Key Achievements:

- Produced novel starlike promesogen-capped polymer for incorporation into liquid crystal
- Synthesized novel, alkyne-capped promesogen small molecule
- Demonstrated successful synthesis of promesogen-capped iron oxide nanoparticles
- Demonstrated successful synthesis of core@shell gold@iron oxide nanoparticles capped with poly(ethylene oxide)
- Successfully modeled plasmonic behavior of synthesized materials

Approaches and Results:

Promesogen-capped Iron oxide nanoparticles via star-like polymer template and click chemistry

The goal of this SEED project was to investigate methods of improving the solubility of nanoparticles in liquid crystal media and modeling core@shell nanoparticle plasmonic properties. The first part was investigated by using a nanoreactor approach to synthesize nanoparticles functionalized with active materials (promesogenic) for improving solubility in liquid crystal media. The details of the reaction setup are shown in **Figure #S-1.1**. The synthesis relies on two techniques; atom transfer radical polymerization (ATRP) and click chemistry. The inner poly(tert-butyl acrylate) core is hydrolyzed to yield poly(acrylic acid). This is essential in forming the inorganic cores as PAA will selectively coordinate with inorganic precursors. ATRP ensures a highly uniform polymerization which affords uniformly-sized polymer arms. This translates into uniformly-sized particles.

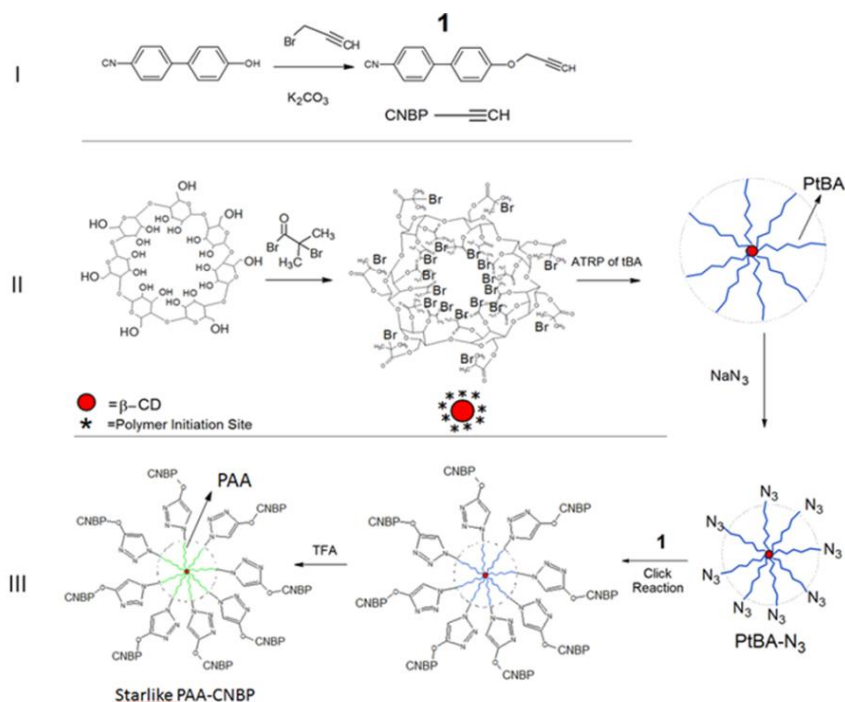


Figure #S-1.1. Synthesis route for star-like PAA-b-CNBP (promesogenic) nanoparticle template

This is evident by the additive nature of spectra A and B in the final product spectra C (left panel). In order to ensure that it is not a simple mixture, FTIR was also used to show the disappearance of the azide peak at 2100 cm^{-1} . This indicates successful click reaction (right panel). Nothing else changes in either techniques indicated only the click reaction occurs with minima side reactions present. In the left panel of **Figure #S-1.3**, one can see the successful formation of the inner superparamagnetic iron oxide

The success of the synthesis of the star-like template, click reaction and resulting particle synthesis were verified by various techniques including HNMR, FTIR (**Figure #S-1.2**), and TEM (**Figure #S-1.3**). The first two techniques verify the polymerization from the core and the near quantitative reaction of the click components respectively. It can be seen in **Figure #S-1.2**, that the promesogenic molecule has been successfully attached to the star template.

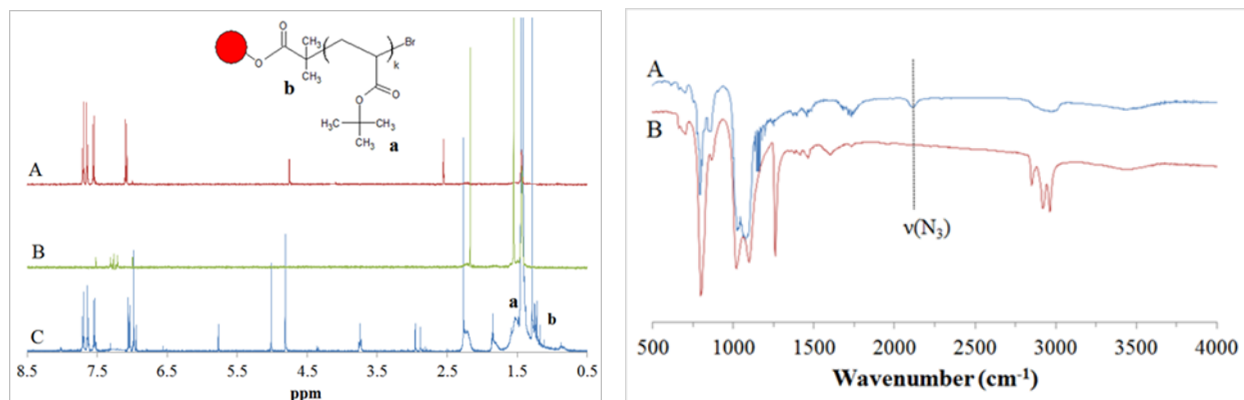


Figure #S-1.2. HNMR (left) and FTIR (right) verifying the successful promesogenic capping of the star-like polymer template via click reaction

nanoparticle (SPION) core. Notice that the particles are of regular size and shape. It should be noted that the reproducibility of these results was quite low. More typically there was heavy aggregation due to the small size of the capping species on the outside of the nanoparticle as shown in the right panel in **Figure #S-1.3**. In order to

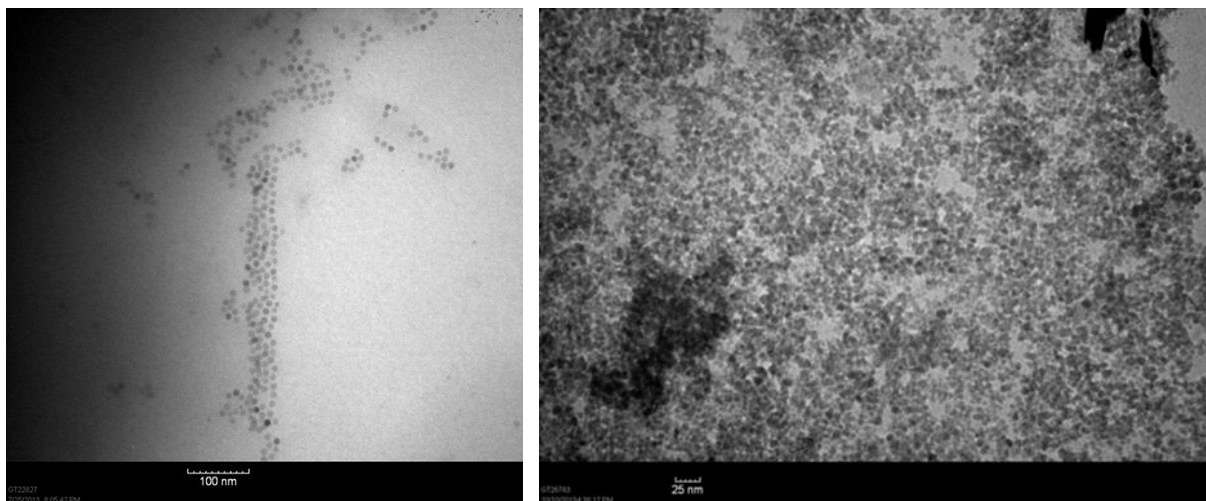


Figure #S-1.3. TEM images of the promesogen-capped iron oxide nanoparticles. The left panel shows distinct particles. The right panel shows aggregated particles (typical)

improve repeatability, future efforts will incorporate a second polymer to the star-like template to provide better control of the shape and size as well as improve dispersion and minimize aggregation. This strategy is useful because the procedure can be easily modified to change the type of polymer and the type of inorganic core present. Furthermore it can also be used to functionalize several additional click-modified species because the terminal bromine atoms on the polymer template can always be converted to azide group. In the second part of the study, a similar star-like template is used. However, an extra polymer layer is used to improve dispersion and ease of purification.

Core@Shell nanocomposites via star-like polymer template—synthesis and simulation

In the second part of the project, similar techniques (ATRP, click chemistry) are used to craft core@shell iron oxide@ gold nanoparticles capped with poly(ethylene oxide) (PEO). In this study, a systematic variation in the thickness (5, 10, 20 nm) of the core (at fixed shell thickness) and a systematic variation of the thickness (10, 20 nm) of the shell (at fixed core thickness) were investigated. The unique size-dependency of the plasmonic band is investigated and finite element modeling is used to simulate and generate calculated spectra for comparison. The variations in the shell thickness can be seen in **Figure #S-1.4**. It should be noted that the core is fixed in all three particle sizes. This size of the shell was controlled by systematically varying the second polymer block of the star-like triblock copolymer template. The inner block corresponds to the core and the outermost block corresponds to the capping polymer (i.e., PEO). The advantage of the technique is thus evident: many different systems can be produced by only varying the molecular weight of the appropriate polymer block.

In addition to core@shell nanocomposites with fixed core and variable shell, variable core and fixed shell nanocomposites were also synthesized in a slightly modified procedure. In both case, x-ray diffraction was used to verify the presence of a distinct core and shell of iron oxide and gold respectively. The details of the core@shell nanocomposite synthesis can be found in **Figure #S-1.5**.

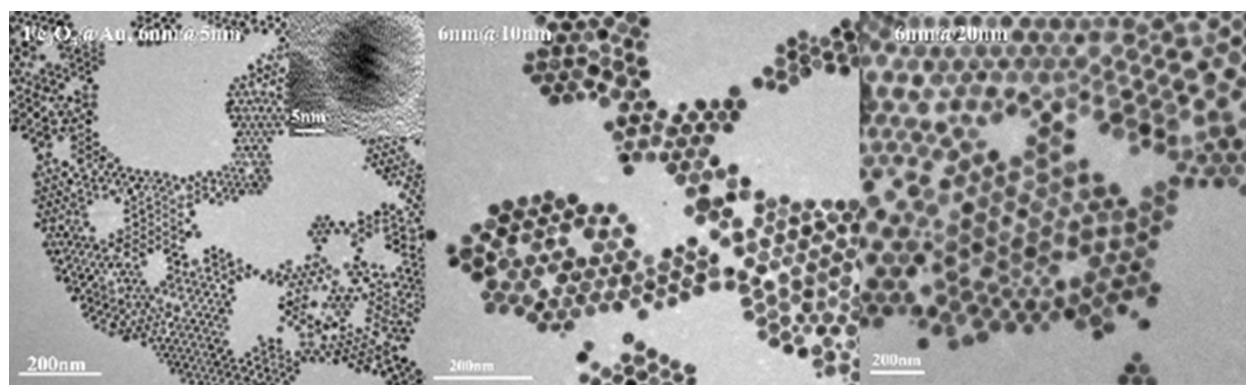


Figure #S-1.3. Core@shell nanoparticles that contain an iron oxide core and a gold shell. The core diameter is fixed and the shell thickness has values of 5, 10 and 20 nanometers.

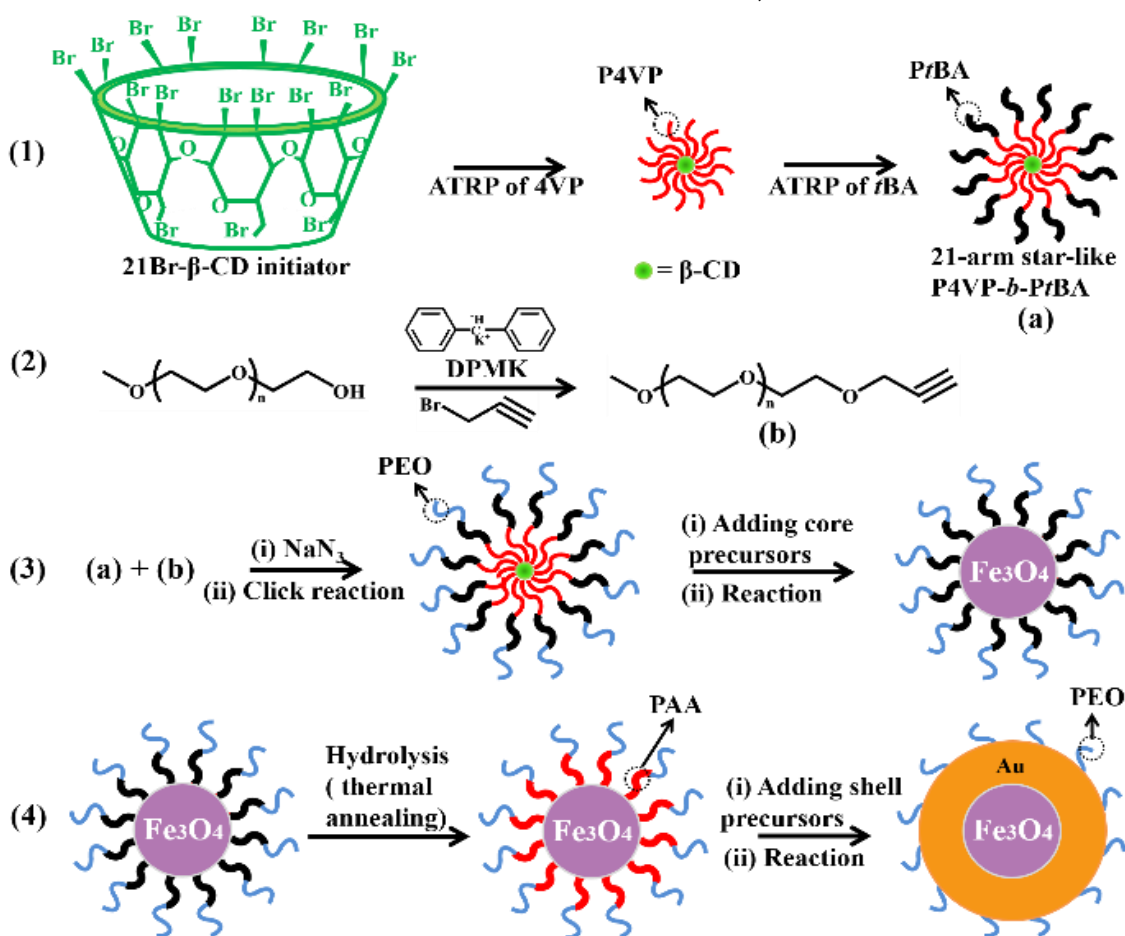


Figure #S-1.5. Procedure detailing the synthesis of a star-like block copolymer (triblock) used to craft core@shell nanocomposites.

Variation of the molecular weight of the poly(4-vinyl pyridine) inner block controls the diameter of the iron oxide core. Whereas variation of the molecular weight of the outer poly(tert-butyl acrylate) block controls the thickness of the gold shell. The outermost polymer block poly(ethylene oxide) serves to stabilize and solubilize the

nanocomposites in water and other polar solvents. Further note that the solubility of the nanocomposites can be tuned by changing which polymer is attached to the star-like polymer template. In this case, PEO was used to enable water soluble nanocomposites. If solubility in organic solvents is desired, hydrophilic polymers can be attached in the same way.

The resulting nanocomposite structures were characterized by UV-Vis spectroscopy to investigate how the plasmonic peak shifts in position and/or changes in intensity as a function of different core and shell thicknesses. It can be seen in **Figure #S-1.6** that the experimental and simulated spectra are in good agreement both in terms of peak position and intensity. Additional simulations and explanations can be found in the second publication listed.

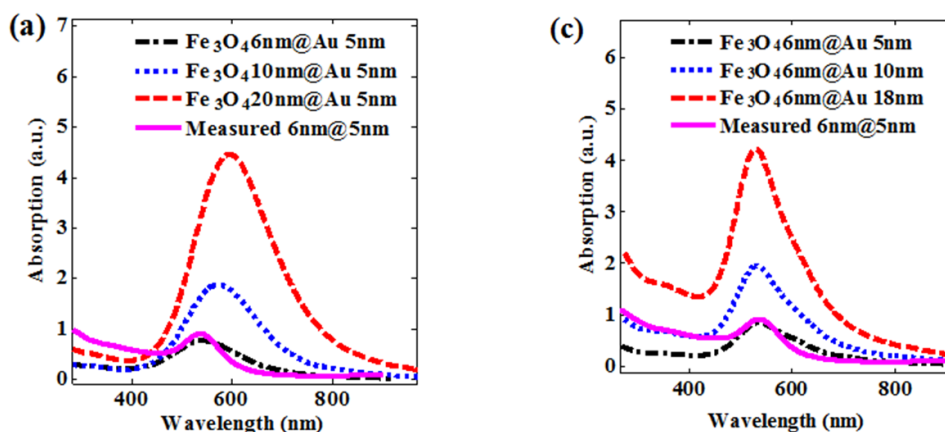


Figure #S-1.4. Experimental and simulated results for core@shell nanocomposites composed of an iron oxide core and gold shell. The left panel addresses fixed shell nanocomposites and the right panel address fixed core nanocomposites

In summary, this BIONIC seed grant has led to a novel, generalizable synthetic route for producing variously-capped nanocomposites of many different compositions (metallic, semiconducting, magnetic), sizes and structures (core, core@shell and hollow).

Interactions with AFRL:

During the summer of 2013, graduate student James Iocozzia visited Wright Patterson Airforce Base near Dayton, Ohio for a week. During this visit, James presented his research and that of the group and attended presentations by students in Dr. Timothy White and Dr. Timothy Bunnings' groups. James learned techniques in preparation of liquid crystal cells and other aspects of applied liquid crystals research. Furthermore, well-defined core@shell structures have been crafted by this new techniques, characterized and simulated. The experimental and simulated procedures are in good agreement with each other. Further work will aim at investigating large size variations of the core and shell, different compositions and different geometries including hollow, rod and tube structures.

Manpower Development/Transitions (Former BIONIC Students at AFRL):

- None.

Publications:

- J. Iocozzia, H. Xu, X. Pang, H. Xia, T. Bunning, T. White*, Z. Lin*, “Star-like polymer click-functionalized with small capping molecules: an initial investigation into properties and improving solubility in liquid crystals,” *RSC Advances*, **4**, 50212-50219 (2014).
- D. Yang, X. Pang, J. Iocozzia, T. Bunning, T. White, Z. Lin*, “Size-tunable plasmonic/magnetic core/shell nanoparticles and enhanced optical response” *Nature Communications* (in preparation)

Presentations:

- None.

Interdisciplinary Research Group (IRG) #3: Cognitive Enhancement
IRG Leader: Eric Schumacher

Project IRG #3-1: Moderate Amounts of Attentional Control of Working Memory (WM) Training to Increase Warfighter Real-time Reasoning and Decision Making Skills with and without Negative Emotional Stress.

Project Participants: Project PIs: Prof. Eric Schumacher, Prof. Shella Keilholz; Students: Savannah Cookson, Erin Lightman, Zain Sultan, Joyce Wong

Air Force Collaborators: WPAFB: Dr. Regina Shia

Research Goals:

To understand the neural mechanisms underlying the regulation of negative emotions and how these emotions and the regulation of them interacts with complex cognition in order to maximize its beneficial effects for real-time war-fighter performance and extend those benefits to decision making under emotional stress.

Key Achievements:

- Demonstration that different emotional control strategies result in unique neural profiles
- Development and pilot testing of follow up experiment investigating how emotion and emotion control interact with cognition
- Presentation of emotion control research at annual meeting of the Cognitive Neuroscience Society

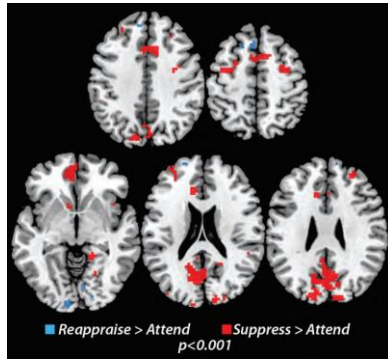
Approaches:

Twenty volunteers were scanned as they completed an emotional control task. At the beginning of each trial subjects viewed a negative picture taken from the International Affective Picture System (IAPS). Immediately after viewing the picture, subjects were instructed to follow one of three directions: the word “Attend” instructed the volunteer to continue thinking about the picture, the word “Suppress” instructed the volunteer to suppress thoughts of the picture, and the word “Reappraise” instructed the volunteer to reinterpret the situation depicted in the picture in a way that no longer elicited a negative reaction.

A follow up study investigating the role of unconscious emotional control on cognitive processes including working memory and attention has also been developed. In each trial of this experiment, volunteers’ memory is tested for both negative and neutral photographs. They are shown either a set of negative photographs or a set of neutral ones. Following a delay, they are presented a single photograph and must determine whether it was in the set shown before the delay. Prior to each trial, subjects’ self-report assessment of the difficulty of the upcoming task and their preparation for it will be collected. With these data we will be able to investigate how brain systems for distinct sub-processes of working memory (i.e., encoding, maintenance, and retrieval) are affected by emotional stress and how individual differences in coping with emotional stress interact with cognition. Behavioral pilot testing is underway to identify efficient behavioral parameters prior to MRI data collection.

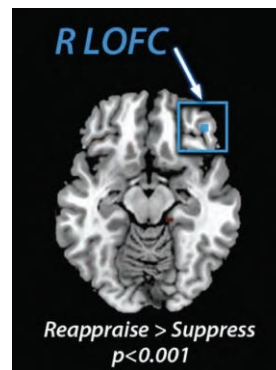
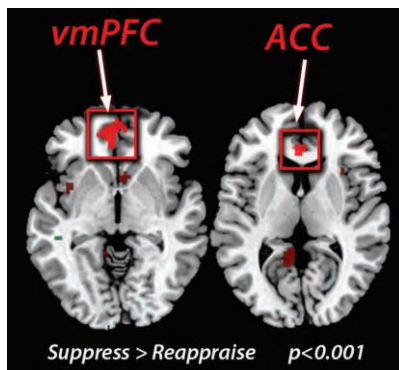
Results:

Consciously implementing suppression and reappraisal control strategies while viewing negative stimuli significantly reduced volunteers’ self-reported negative affective



states. There was no difference in effectiveness of reducing negative affective states between the two control strategies. Volunteers also reported being less successful in following “Suppress” and “Reappraise” instructions compared to the “Attend” instruction. Imaging data suggests that Suppression elicits greater overall neural activity than Reappraisal. Regions common to both strategies include calcarine sulcus and prefrontal cortex. Regions uniquely involved in Suppression include left and right lateral prefrontal cortex as well as bilateral

ventromedial prefrontal cortex and anterior cingulate cortex. Regions uniquely involved in Reappraisal include bilateral medial pre-frontal cortex and right lateral orbito-frontal cortex.



AFRL/Georgia Tech Interactions:

- Design of appropriate assessment tasks (Schumacher (GA Tech), Shia (AFRL)).
- Design of protocol to investigate the effects of automatic emotion regulation on task performance, subjective affective state, and brain activity (Schumacher (GA Tech), Shia (AFRL)).

Manpower Development/Transitions (Former BIONIC Students at AFRL):

- None.

Publications:

- H. Schwarb, J. Nail, A. McKinley, E. H. Schumacher, “Moderate Amounts of Spatial and Verbal N-Back Training Improves Working Memory Capacity As Measured by Untrained Working Memory Tasks, (manuscript under review).
- Z. Sultan, E. Lightman, R. Shia, J. Wong, E. H. Schumacher, “Emotion control mechanisms: underlying neural architecture of suppression and reappraisal” (manuscript in preparation).

Presentations:

- Z. Sultan E. Lightman, R. Schmidt, J. Wong, E. H. Schumacher, “Emotion control mechanisms: underlying neural architecture of suppression and reappraisal.” Poster presented at the 19th annual meeting of the Cognitive Neuroscience Society, April, 2012.

Project IRG #3-2: Functional connectivity and dynamic network analysis for targeted intervention in brain network activity

Project Participants: Project PIs: Prof. Shella Keilholz, Prof. Eric Schumacher; Students: Garth Thompson, Matthew Magnuson, Hillary Schwarb, Brian Roberts, Wenju Pan, Mac Merritt

Air Force Collaborators: WPAFB: Dr. Andy McKinley, Dr. Lloyd Tripp

Research Goals:

To understand the relationship between functional brain connectivity and cognitive task performance. One idea that is gaining traction in the psychology and neuroscience communities is that memory, attention and control cognitive functions, rather than being primarily mediated by particular areas, are dependent upon carefully coordinated spontaneous interactions between functional networks in the brain. One of the most interesting findings in recent functional connectivity studies using MRI is that two of the networks commonly observed in normal volunteers seem to be related to the attentional focus of the subject. The first is the so-called “default mode” network, a group of brain areas (including the precuneus and posterior cingulate cortex) whose activity decreases when the subject is asked to perform a task and increases during quiet relaxation. The second network is the task-positive network, sometimes called the executive attention network, a group of areas (e.g., prefrontal and parietal cortices) whose activity increases during a wide variety of cognitive tasks (Fox et al., 2005). The goal of Project #3-2 is to develop dynamic analysis techniques to examine the relationship between these two networks as a function of time, and to test the performance of these techniques in the context of predicting task performance both intra- and inter-individual.

Key Achievements:

- Previously found that steady state functional connectivity is a relatively stable trait linked to performance on multiple cognitive tasks (manuscript under revision), while network dynamics can be used to predict performance on a trial-by-trial basis (manuscript published in Human Brain Mapping journal)
- Designed new protocols to examine whether network dynamics can predict performance on more complex tasks involving working memory
- Acquired a new multi-band EPI sequence that allows the whole brain to be imaged in less than 1 second, a significant improvement over previous temporal resolution that will increase sensitivity for dynamic analysis
- Tested the new multi-band sequence, assessed signal-to-noise ratio and artifacts, and determined optimal parameters for further studies
- Tested the use of ICA for network definition; results validated previous work with seed-based correlation
- Presented findings at international and national meetings (Human Brain Mapping, Cognitive Neuroscience, Biomedical Engineering Society)

Approaches and Results:

Twenty subjects were asked to perform a vigilance task (e.g., press a button whenever a small circle on the projection infrequently changed color from blue to purple) while functional connectivity MRI data was collected. Dynamic analysis

techniques were developed at Georgia Tech and used to map times when the default mode network or the task-positive network were dominant. For intra-individual analysis, sliding time windows ranging from 12 seconds before the task to 12 s after the task were examined. The level of correlation between the default mode network and the task positive network for each time window were calculated and examined for a relationship with task performance. Strong anti-correlation between these two networks over a period of 12 seconds prior to a detection event proved predictive of a fast response time. For inter-individual analysis, correlation within each network and between the two networks was plotted against performance on a battery of standard cognitive tasks. The results showed that performance on a wide variety of tasks was linearly related to measurements of coherence within and between networks. Based on these results, we implemented a method of voxel-based morphometry, which was used to compare the anatomical scans of good performers to poor performers and identify regions in which grey or white matter volume was significantly increased (**Figure #3-2.1**). Several regions were detected and will be used in future connectivity analyses. In another effort parallel to our initial dynamic analysis of connectivity, maps of the default mode and task positive networks were created from 12 s windows prior to task performance. The networks were clearly distinguishable even with such short periods due to the high temporal resolution of the data. Differences in networks between good and poor performers can be identified (**Figure #3-2.2**). We also implemented a better statistical testing method for multiple comparisons based on bootstrapping.

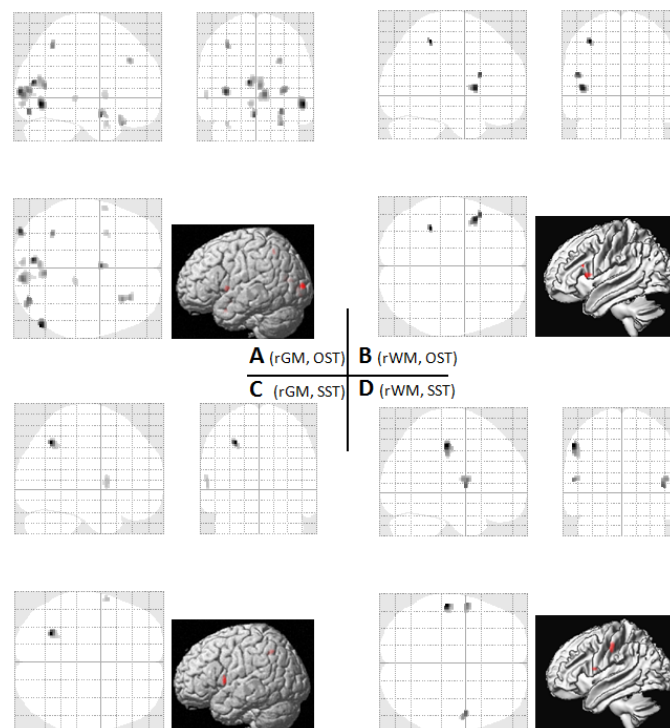


Figure #3-2.1. Voxel based morphometry results. A) Regions where grey matter volume is linked to performance on the Ospan task. B) Regions where white matter volume is linked to performance on the Ospan task. C) Regions where grey matter volume is linked to performance on the symmetry span task. D) Regions where white matter volume is linked to performance on the symmetry span task.

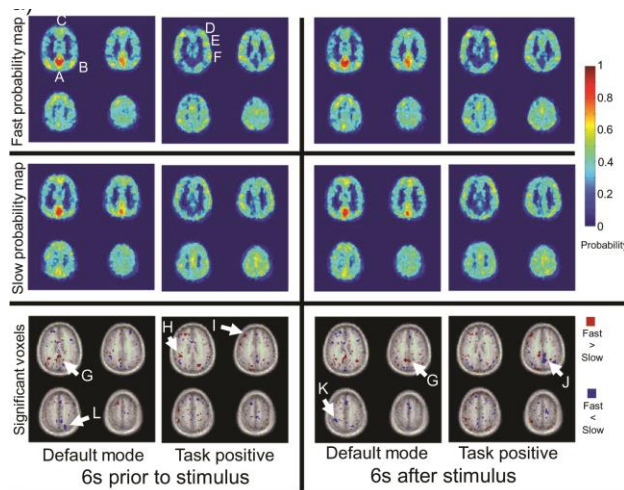


Figure #3-2.2. Top and middle) Probability maps for the default mode and task positive mode in fast and slow responders on the psychomotor vigilance task, based on 12 s windows before and after the stimulus. Bottom) areas where significant differences are observed in the probability maps between fast and slow groups. Arrows indicate areas of particular interest that are likely to be involved in task performance.

AFRL/Georgia Tech Interactions:

Key interactive research tasks for this project include:

- Design of an appropriate vigilance task (Schumacher, McKinley, Smith (AFRL))
- Identification of changes in functional connectivity in default and task-positive networks during the task as compared to quiet rest (Keilholz, Schumacher)
- Development of voxel-based morphometry to identify anatomical substrates of performance differences (Keilholz)
- Identification of dynamic network features that are tied to improved task performance (Keilholz, Schumacher)

Manpower Development/Transitions (Former BIONIC Students at AFRL):

- None.

Publications:

- G. Thompson, M. Magnuson, M. Merritt, H. Schwarb, A. McKinley, L. Tripp, W.-J. Pan, E. H. Schumacher, S. D. Keilholz, "Short Time Windows of Correlation between Large Scale Functional Brain Networks Predict Vigilance Intra-individually and Inter-individually," *Hum. Brain Mapp.*, **34** (12) 3280-98 (2013).
- M. Magnuson, G. Thompson, H. Schwarb, B. Roberts, W. Pan, A. McKinley, L. Tripp, E. H. Schumacher, S. D. Keilholz, "Functional Connectivity in Resting Brain Networks is Linearly Linked to Inherent Processing Ability on a Variety of Cognitive Tasks," *submitted to NeuroImage*.

Presentations:

- G. Thompson, M. Magnuson, M. Merritt, H. Schwarb, W.-J. Pan, A. McKinley, L. Tripp, E. H. Schumacher, S. D. Keilholz, "Resting state networks generated from twelve second segments of fMRI scans are behaviorally relevant," Organization for Human Brain Mapping, Beijing, China, June 2012.
- W.-J. Pan, M. Magnuson, G. Thompson, H. Schwarb, E. H. Schumacher, S. D. Keilholz, "Brain structures associated with working memory performance: a voxel-based morphometric study," Organization for Human Brain Mapping, Beijing, China, June 2012.

- M. Merritt, G. Thompson, M. Magnuson, H. Schwarb, W.-J. Pan, L. Tripp, A. McKinley, E. H. Schumacher, S. D. Keilholz, "BOLD Signal Changes in Resting State Networks Are Related to Performance on a Vigilance Task," BMES, Atlanta, GA, October 2012.
- M. Merritt, S. Spratt, J. Grooms, G. Thompson, W. Pan, E. H. Schumacher, S. D. Keilholz, "Correlation between individual, ICA generated, resting state fMRI networks predicts variability in reaction time on PVT," Poster presentation at BMES, Seattle, Washington, 2013.

Project IRG #3-3: fMRI and Functional Connectivity as Assessment Tools for Transcranial Stimulation (TMS/tDCS) Interventions

Project Participants: Project PIs: Prof. Eric Schumacher, Prof. Shella Keilholz; Students: Brian Roberts, Garth Thompson, Matthew Magnuson, Waqas Majeed, Mac Merritt, Hillary Schwarb

AFRL collaborators: WPAFB: Dr. Andy McKinley, Dr. Lloyd Tripp

Research Goals:

To understand the relationship between functional connectivity among regions of the human neocortex and subsequent memory and other task performance so that these processes may be improved with neural stimulation. The varying functional roles attributed to a given region of the human neocortex suggest the possibility that individual regions may have to synchronize their activity with other brain regions in order to produce different functional outputs, as required by a particular context or task. The discovery of sets of regions that display correlated activation time courses with respect to one another, along with strongly anti-correlated relationships with respect to other regions, has led to an interest in understanding the relationship between human performance on various cognitive and memory based tasks and varying patterns of network activity, both during task engagement and during participant resting states (Fox et al., 2005; Kelly et al., 2008). Further, previous investigation has revealed a role of offline replay of task induced patterns of brain activity that underlies memory consolidation in mice (Ji & Wilson, 2007; Cheng & Frank, 2008). The goal of Project #3-4 is to use emerging analysis techniques to define a network of brain regions that subserve successful memory encoding on a paired associates task and to examine the relationship between memory performance and the spatiotemporal dynamics of that network.

Additionally, transcranial direct current stimulation (tDCS) has been effectively used in several studies to safely reduce cognitive impairment or stimulate cognitive enhancement during a short time scale. The functional use of tDCS is dependent on its endurance, but few studies have attempted to understand the potential long term effects. In order to safely assess the longitudinal use of this technique, an animal model for measuring its effectiveness needs to be developed. One study has reported elevated fMRI activation in several regions of interest in the rodent brain while undergoing online stimulation (Takano 2011).

Key Achievements:

- Analyzed data and submitted manuscript of functional connectivity during memory consolidation.

- Developed follow-up experiment to apply short window correlation connectivity analysis to previously implement face-name procedure and other control tasks.
- Collected pilot data on these tasks
- Continued development and testing of protocol for investigating long-term effects of tDCS in rodent model.
- Continued development and testing design modifications to allow near-simultaneous stimulation and imaging to capture short-term effects.

Approaches and Results:

Project 3-3.1:

FMRI data from a face-name associative pair task allowed for a two-stage analysis. The first of these analyses was carried out by running a general linear model that was used to localize regions of the brain that showed task-induced activity increases. Activated regions in IIFG, IFusG, and ILG were then used to create seed regions of interest (ROIs; **Figure #3-3.1**). In the second analysis stage, connectivity contrasts were performed showing areas of the brain whose activity is significantly more temporally synchronized with these seed regions during post-task consolidation delay periods compared to pre-task baseline resting states (**Figure #3-3.2**). Results indicate that a previously uncharacterized resting state mnemonic network exists in the human brain, consisting of temporally synchronized activation within IIFG, IFusG, and IHC. Additional connectivity analyses confirmed that the three seed regions showed temporally synchronized activation during encoding as well. These data extend results from single cell recording studies in mice (e.g. Ji & Wilson, 2007; Cheng & Frank, 2008) by showing that coordinated patterns of reactivation occur in the awake human brain.

Project 3-3.2:

In order to provide tDCS, rats were first shaved and then anesthetized with isoflurane. A 25 mm² square made of conductive rubber was then placed over the right somatosensory cortex of each rodent. Conductivity was ensured using a highly conductive EEG electrode gel. The Cathode was an 8 cm² square placed on the animals back. Using a 9.4 T animal MRI scanner, the blood oxygenation level dependent (BOLD) signal was measured under a rest condition and under forepaw stimulation. After recording baseline levels, animals received tDCS at 400 micro amps for ten minutes. After transcranial stimulation, the BOLD signal was recorded again both

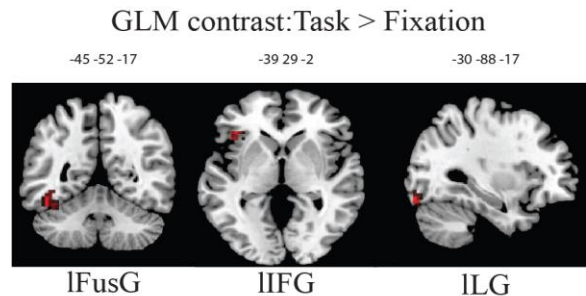


Figure #3-3.1. Regions Active at Encoding

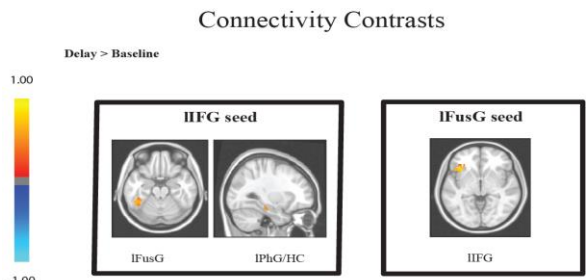


Figure #3-3.2. Synchronized Activity during Memory Consolidation

at rest and under forepaw stimulation. Subsequent analysis of fMRI data was conducted to compare the two conditions in three ways: seed based correlation, spectral density, and correlation to the forepaw stimulation time course. No significant difference between the un-stimulated and stimulated condition was found.

Although the effects of tDCS were not quantifiable with the current experimental methods, several methods have the potential to quantify its effects in the future. First, the lack of results may be due to the anesthesia used. Awake animal studies or another anesthesia that is more similar to the awake condition may provide a quantifiable difference in the stimulation condition. Second, different modalities may be useful to measure the effectiveness of tDCS. Work is currently being conducted at WPAFB to develop a model to test the effects of tDCS on behavior, cellular protein levels, and gene expression, and future studies could use electrophysiology to directly observe shifts in local field potentials. Finally, previous studies have used online stimulation and fMRI, whereas the current study used subsequent stimulation and fMRI. Using both techniques concurrently in future may allow for more effective observation of physiological changes.

AFRL/Georgia Tech Interactions:

- Design of appropriate memory task (Schumacher, Keilholz, Tripp)
- Identification of seed regions in IIFG, IFusG, and ILG for connectivity analysis (Keilholz, Schumacher)
- Seed region connectivity analysis completed (Keilholz, Schumacher)
- Development and testing of rodent tDCS model (Keilholz, McKinley)
- Develop and test new protocol with awake rodents.
- Investigate effect of tDCS on behavior, cellular protein levels, and gene expression,

Manpower Development/Transitions (Former BIONIC Students at AFRL):

- None.

Publications:

- B. M. Roberts, J. Shin, G. Thompson, A. McKinley, S. D. Keilholz, E. H. Schumacher, "Subsequent memory and post-encoding resting state connectivity: neural replay effects during offline processing," *submitted, under review*.

Presentations:

- B. M. Roberts, G. Thompson, J. Shin, H. Schwarb, S. D. Keilholz, E. H. Schumacher "Functional connectivity and subsequent memory: increased neural co-activation during post-task resting states is related to later memory performance," Poster presented at the 19th annual meeting of the Cognitive Neuroscience Society, April, 2012.

Seed Grant #1: Simultaneous Functional Neuroimaging and Low Frequency EEG of Resting State and Real Time Decision Making

Project Participants: Project PIs: Prof. Charles Epstein, Prof. Shella Keilholz, Prof. Eric Schumacher; Students: Garth Thompson, Hillary Schwarb, Josh Grooms

AFRL collaborator: WPAFB: Dr. Regina Shia

Research Goals:

To quantify the correlation between resting state and attentional networks as determined by simultaneous fMRI and low frequency EEG, both at rest and during a decision-making task. The so-called “default mode” and “task-positive” brain networks have been extensively studied using fMRI BOLD imaging as fundamental modes of brain connectivity. However, a connection between these networks and electrical potential changes in the brain has been demonstrated only indirectly by comparing signals of differing frequencies. The physiological basis of these networks will remain uncertain until matched frequencies are investigated. Direct correlation between changes in fMRI and very low frequency (< 0.1 Hz) EEG will establish with greater certainty the neural origin of the fMRI changes. In addition, use of fMRI to drive analysis of the electrical signal may lead to detection of network activity using the EEG only, allow studies of network activity outside the MRI scanner, and provide a more portable and economical tool to study attention in realistic situations.

Key Achievements:

- Previously showed that different portions of the EEG signal correlate significantly with the fMRI signal from different networks, including the default mode network
- Developed novel preprocessing algorithms that result in clearer correspondence between BOLD and low frequency EEG
- Examined the role of low frequency EEG in the global BOLD signal
- Presented findings at the Human Brain Mapping meeting in 2013 and an abstract has been accepted for the Resting State Functional Connectivity workshop in September 2014

Approaches:

EEG Recording:

Because of the substantial voltages induced by the MRI gradient at multiple frequencies, recording EEG inside an MRI scanner has been compared to making ice cream inside a blast furnace. Slow electrochemical drift at the scalp-electrode interface helps confine conventional EEG recording to frequencies above 0.5 Hz, whereas matching the frequency range of fMRI “functional connectivity” analysis requires focusing only on EEG activity below 0.08 Hz. Our 64-channel recording system has an enormous dynamic range of 24 bits, which not only allows accurate subtraction of gradient artifacts but prevents saturation of the amplifiers during DC recording. The electrodes are sintered silver/silver chloride, the most stable interface recording interface available. Even with these advantages, our expectation is that potential drift will degrade the signal from some of the recording sites, but that with 64 electrodes sufficient numbers will function to allow adequate scalp coverage.

fMRI Recording:

As previously described in Project #3-2, this study examines the so-called “spontaneous” brain activity at low frequencies rather than a traditional block or event driven design.

Vigilance Task:

As previously described in Project #3-2: A simple button press whenever a small circle changes color.

Analyses and Results:

Two approaches to data analysis were taken. In the first, the signal from all EEG electrodes was clustered into 1-5 groups (usually three). The time course from a representative electrode in each group was correlated with the BOLD fluctuations at varying time lags. The results were averaged across all scans from all subjects. The thresholded images (overlaid on a generic anatomical image) were generated by converting correlation coefficients to z-values (Fisher's r-to-z Transform), then testing for significance ($\alpha = 0.05$) and correcting for multiple comparisons using false discovery rate (FDR). Statistically significant correlations between the signal from many electrodes (FPZ and P8 are shown in **Figure #S-1.1**) and the BOLD signal from sensorimotor areas were observed during group analysis.

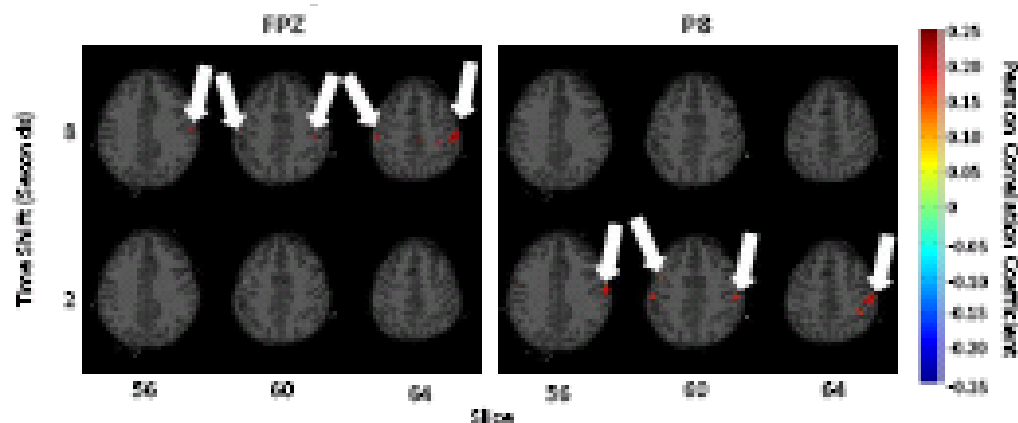


Figure #S-1.1. Correlation between the signal from FPZ (left) and P8 (right) electrodes and the BOLD MRI signal, averaged across all subjects and thresholded at a significance level of $\alpha = 0.05$. Strong correlation is found with areas that are part of the task positive network.

FDR is likely too conservative for this method because very few voxels out of large areas of high correlation are still considered significant after thresholding. Eventually, the analysis that yields these images will be replaced by one that employs bootstrapping for significance and Sequential Goodness of Fit (SGoF) to correct for multiple comparisons. This should allow more of the voxels to survive the thresholding process. However, there have been technical difficulties in coding SGoF to accept the large data sets we are trying to input. We expect this to be resolved in the near future. In the second analysis approach, spatial independent component analysis (sICA) was used on raw BOLD images to separate independent resting state networks (RSNs), which are well known to literature and were identified by visual inspection. sICA provides both the

spatial patterns and time courses of the network activity. These time courses from each RSN were then each cross-correlated with all EEG signals. Correlations with the task positive network time course yield the most interesting results. Lastly, thresholding of correlation coefficients in this analysis was performed using bootstrapping and SGoF, which was possible because this set of data is much smaller than the correlations between EEG and BOLD.

These preliminary data show that there is a relationship between low frequency EEG and the BOLD signal, and so low frequency EEG holds promise as a noninvasive marker of performance state for future studies.

AFRL/Georgia Tech Interactions:

Key interactive research tasks for this project include:

- Develop techniques for successful simultaneous recording of continuous fMRI, low-frequency EEG, and responses to the vigilance task (Epstein, Grooms, Keilholz, Thompson, Schwarb, Schmidt (AFRL))
- Develop appropriate correlation, clustering, and analysis techniques for combined EEG fMRI data (Keilholz, Thompson, Schumacher, Epstein, Schmidt (AFRL))
- Develop cluster analysis for EEG signals that will allow characterization of slow network activity from EEG alone (Keilholz, Thompson, Schumacher, Epstein, Schmidt (AFRL))

Manpower Development/Transitions (Former BIONIC Students at AFRL):

- None.

Publications:

- A manuscript has been submitted to Neuroimage and a second is in preparation.

Presentations:

- J. Grooms, G. Thompson, H. Schwarb, E. H. Schumacher, R. Schmidt, C. Epstein, S. Keilholz. "Infraslow EEG correlates of fMRI." Human Brain Mapping 2013; 1835. Poster presentation.

Seed Grant #2: Real-time Cognitive Monitoring using Biofunctionalized Field Effect Transistor Sensors

Georgia Tech Participants: Project PI: Prof. Oliver Brand; Students: Spyridon Pavlidis, Patrick Getz, Dr. Jin-Jyh Su, Dr. Luke A. Beardslee, Christopher Carron

AFRL Collaborators: WPAFB: Dr. Josh Hagen, Dr. Nancy Kelley-Loughnane, Dr. Ryan Kramer, Dr. Rajesh Naik

Research Goals:

To develop a sensor platform for real-time cognitive monitoring based on an array of thin film transistors (TFTs) that can be individually functionalized with biological recognition elements to report the presence or absence of the human performance target of interest. Suitable recognition elements can be antibodies, peptides, or aptamers, which bind and/or change conformations in the presence of a specific target.

Key Achievements:

- Developed a fabrication process and consequently fabricated staggered, bottom-gate thin film transistors based on ZnO and InGaZnO on rigid Si substrates using a design that enables individual control of each device across the wafer and provides compatibility with microfluidic structures for sample delivery.
- Optimized fabrication of staggered, bottom-gate InGaZnO thin film transistors (TFTs) deposited either with pulsed laser deposition (PLD) or radio-frequency (RF) sputtering. Tested InGaZnO TFTs with Al₂O₃ bottom gate insulator deposited by atomic layer deposition (ALD) exhibit threshold voltages $V_T \leq 2$ V, saturation mobilities $> 4 \text{ cm}^2\text{V}^{-1}\text{s}^{-1}$, on/off ratios $> 10^7$ and sub-threshold voltage swings as low as 0.18 V/dec.
- Improved the bias stress stability of the TFTs by employing a combination of post-process annealing and pulse-mode operation.
- Demonstrated the use of these TFTs for VOC sensing in the gas phase with bare, polymer-coated and pulse-operated devices.
- Shipped several sets of TFTs to AFRL and the University of Cincinnati for integration with microfluidics, biofunctionalization, and liquid-phase sensing.
- Studied and compared passivation schemes for the InGaZnO TFTs. Different thin film deposition methods were studied, such as ALD, RF Sputtering and Plasma-Enhanced Chemical Vapor Deposition (PECVD) at various temperatures. Multiple materials were also considered, including silicon nitride (SiN_x), silicon oxide (SiO₂), zirconia (ZrO₂), titania (TiO₂) and alumina (Al₂O₃).
- Low-temperature ALD TiO₂ passivated TFTs show best performance and improved bias stability in air without degrading device behavior.
- Current-voltage (IV) and bias stability measurements in liquid (both distilled water and phosphate buffered saline) were successfully demonstrated without observation of hydrolysis.
- Dual-gate TFT configuration was initially demonstrated by controlling the drain current through variation of DI water and PBS droplets on the device. This opens the door to liquid-phase pH with sensitivity beyond the Nernst Sensitivity Limit (50 mV/pH) and biosensor testing.
- 4th generation mask set undertaken which improves device dimensions (W/L ratio), adds thin film characterization structures (i.e., metal-insulator-metal capacitors, contact resistance structures), adds a new mask for patterning the passivation layer and improves integration with microfluidic structures by adjusting die size and device-to-device spacing.
- CMOS-based extended-gate FET structures were designed and fabricated using Texas Instruments CMOS technology. In addition, dedicated CMOS circuitry to read out the InGaZnO TFTs was designed and fabricated using TI CMOS technology.

Approaches and Results:

Using the microfluidic-compatible mask design developed in 2010-2011, a fabrication process was developed for thin film transistors (TFTs) made from indium gallium zinc oxide (InGaZnO) on 4" n-type silicon (Si) wafers and carried out in the Georgia Tech Institute of Electronics and Nanotechnology (IEN) cleanroom facilities. The resultant TFTs were of the staggered, bottom-gate configuration with gate lengths of 2, 5 and 10 μm . In order to isolate each device, a 1 μm thick thermal oxide layer was first grown on

the Si substrate. Bottom-gate electrodes made from electron-beam deposited aluminum or Cr/Au) were then patterned for individual control of each device across the wafer. A 50 nm aluminum oxide (Al_2O_3) layer deposited via atomic layer deposition (ALD) at 180 °C was used as the gate dielectric. Subsequently, RF sputtering from an InGaZnO (1:1:1) ceramic target was conducted at room temperature to deposit a 50 nm thick active layer. Finally, chromium/gold (Cr/Au) drain (D) and source (S) contacts were created using lift-off. **Figure #S-2.1** shows the cross-section (left) and top-view (right) of the TFT for sensing applications.

Upon completion of fabrication, the devices were tested at a wafer-level using a probe station. The transfer characteristic (I_D vs. V_{GS}) of a 5 μm TFT (**Figure #S-2.2**) shows that several performance improvements have been improved throughout the period of this research. The threshold voltage, V_{TH} , has been dramatically decreased to ~ 2 V, the on/off ratio is $>10^7$, the saturation mobility, μ_{SAT} , is $> 4 \text{ cm}^2\text{V}^{-1}\text{sec}^{-1}$ and the sub-threshold swing, S , is 0.18 V/dec. Working wafers were diced so that individual chips could be placed in ceramic dual-in-line (DIL) packages for additional electrical and sensor testing.

In an effort to address the issue of bias stress instability, which is commonly encountered in oxide semiconductors, post-process annealing and pulse-mode operation were investigated and, consequently, shown to minimize the shift in threshold voltage, ΔV_{TH} , over time. Each technique was evaluated by monitoring a TFT's ΔV_{TH} over a period of 30 min while applying $V_{GS} = V_{DS} = 6$ V. Instantaneous values for V_{TH} were extracted from I_D vs. V_{GS} sweeps that were conducted every 5 minutes throughout the stress test. To ensure repeatability, multiple devices were tested for each condition and the average values are presented below in **Figures #S-2.3 and #S-2.4** with error bars, where appropriate.

In **Figure #S-2.3**, the anneal period was maintained for 90 minutes while three different annealing temperatures were investigated: 100°C, 200°C and 300°C. A clear dependence on the annealing temperature was observed, indicating that higher

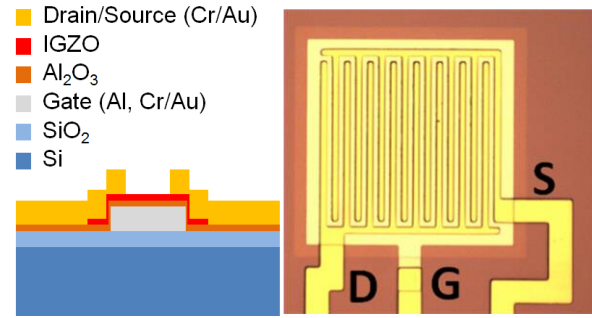


Figure #S-2.1. (left) Cross-sectional view of InGaZnO TFT. (right) Micrograph depicting the comb-type source and drain electrodes of a fabricated TFT with 5 μm channel length and a W:L ratio of 466. A via transition is used to connect to the bottom-side gate electrode.

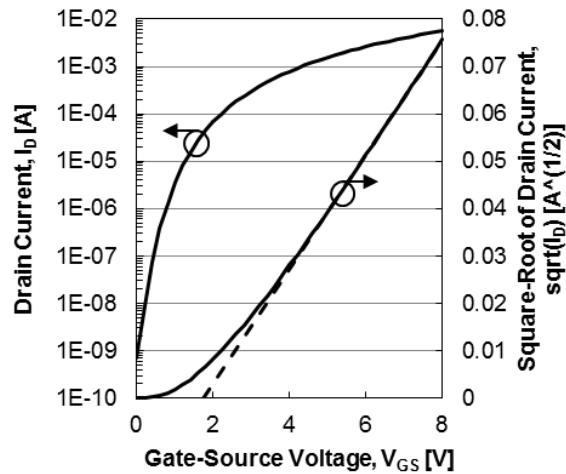


Figure #S-2.2. Transfer characteristic of a TFT with 5 μm channel length ($V_{DS} = 8$ V). I_{DS} is plotted on a log scale on the left, while the square root of I_{DS} is plotted on the right. bottom-side gate electrode.

temperatures are required to achieve better stability. Moreover, higher temperature annealing also resulted in smaller performance variability from device to device, shown by a reduction in the error bars.

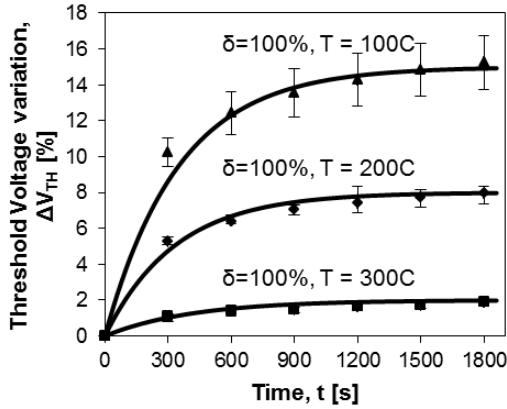


Figure #S-2.3. Relative change of the threshold voltage, ΔV_{TH} , as a function of bias time for a bias stress of $V_{GS} = V_{DS} = 6$ V. The trends for devices annealed for 90 minutes in air at the temperatures of 100 °C, 200 °C and 300 °C are shown. The duty cycle is maintained at 100%. The data are described by stretched-exponential functions.

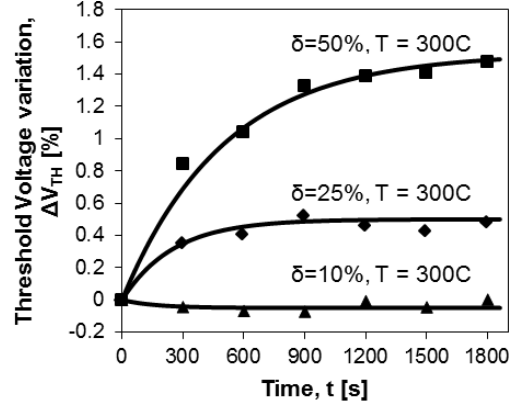


Figure #S-2.4. Relative change of the threshold voltage, ΔV_{TH} , as a function of bias time for a bias stress of $V_{GS} = V_{DS} = 6$ V. The trends for devices annealed for 90 minutes in air at a temperature of 300 °C but with varying duty cycles during bias stress are shown. The data are fitted by stretched-exponential functions.

It is believed that annealing reduces the number of subgap states as well as the number of oxygen vacancies in the active layer in order to produce a more stable device. In order to achieve even greater stability, the reduction of the duty cycle, δ , via pulsed operation of the TFT was investigated and is presented in **Figure #S-2.4** for $\delta = 50\%$, 25% and 10%. It is apparent that adjustment of the duty cycle translates into better control of ΔV_{TH} . For example, when $\delta = 25\%$, $\Delta V_{TH} \sim 0.5\%$ or $\Delta I_D < 35\%$. Moreover, it is observed that with a low enough duty cycle, e.g. $\delta = 10\%$, the trend can be reversed altogether such that ΔV_{TH} becomes negative. This behavior suggests that an optimum duty cycle can be identified for each device, with which a reference I_D can be reliably defined throughout the TFT sensor's deployment. A further favorable consequence of utilizing lower duty cycles lies in the improved power management.

To prove the viability of InGaZnO TFTs for chemical and, eventually, biochemical sensing, their response to various concentrations of ethanol in the gas-phase was recorded. Throughout the measurements, the TFTs were operated at room temperature. Mass-flow controllers (MFCs) were used to regulate the concentration of the analyte. Following

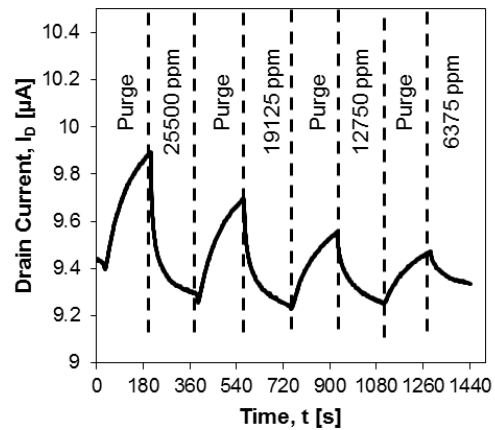


Figure #S-2.5. Drain-current vs. time under constant bias conditions ($V_{GS} = V_{DS} = 8$ V) for a bare InGaZnO TFT subjected to consecutive ethanol exposures and synthetic air purges.

each analyte exposure, a purge cycle was executed by flowing synthetic air (20% O₂ and 80% N₂) over the device. **Figure #S-2.5** depicts the typical response of a bare TFT biased in the saturation region with $V_{GS} = V_{DS} = 8$ V and $\delta = 100\%$. The sensor shows a significant decay in I_D during the windows of ethanol exposure, followed by an increase in current during the purge cycles. For example, 25500 ppm of ethanol induced a downward ΔI_D of 0.5-0.6 μ A or 5-6 %. Measurements were also conducted using non-conducting organic polymers, such as polyepichlorohydrin (PECH), to boost the sensor's response by increasing the rate of ethanol adsorption. In this case, two main differences were seen: (1) the polarity of the response was inverted such that the presence of ethanol now caused a rise in I_D and (2) the amplitude of the response increased by a factor of 3-4.

In collaboration with the group of Prof. Ian Papautsky at the University of Cincinnati (UC), who is responsible for the microfluidic interface bonded to the sensor surface, we explored the use of the TFTs as liquid-phase sensors. Efforts have been made towards the integration of the microfluidic structure (developed by Xiao Wang at UC) made from either PDMS or PMMA. Mounting schemes based on O-Zone plasma treatment or bonding glues were investigated both in terms of their ability to reliably adhere the MF structure to the TFT die as well as their impact on the TFT's performance. **Figure #S-2.6** depicts the mounted MF structure on a die. During initial experiments electrolysis was observed when small droplets of DI water (5 μ L) were placed on the TFT. Thus, successful operation in water-based liquids requires either operation at reduced voltages or an improved passivation scheme.

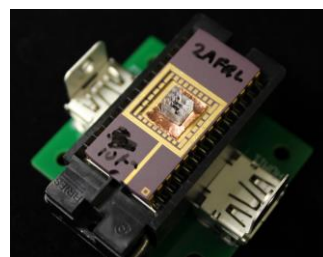


Figure #S-2.6. Wire-bonded TFT sensor in a DIL package. The microfluidic structure developed at UC has been mounted above the TFT die.

To improve device stability in liquid, the use of passivation layers has been investigated. It was found that passivating the sensor chip surface with inorganic thin-film materials, such as ALD-deposited alumina or zirconia as well as plasma-enhanced chemical vapor deposition (PECVD)-deposited silicon dioxide (SiO₂) or silicon nitride (SiN_x), significantly degrades the TFT performance. Most notably, the on/off ratio was reduced by several orders of magnitude and V_{TH} experienced a significant shift in the negative direction.

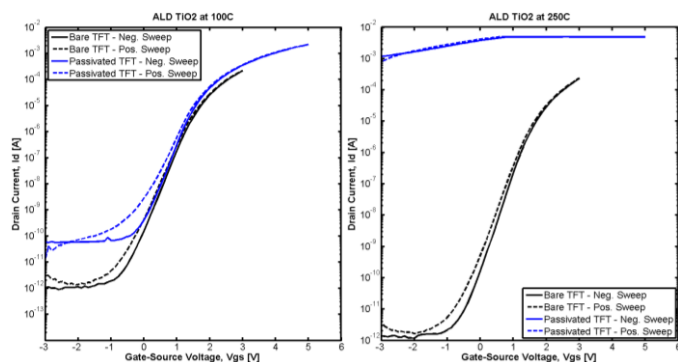


Figure #S-2.7. Comparison of bare and TiO₂-passivated TFT at 100°C. (left) or at 250°C (right).

ALD Titania (TiO₂) presented the best results, particularly when deposited at low temperature. A comparison of the effect of low temperature (100°C) versus high temperature (250°C) passivation is shown in **Figure #S-2.7**. Though there was a slight degradation of the on/off ratio, V_{TH} did not shift, and μ_{SAT} increased to 5.8 cm²V⁻¹sec⁻¹. **Figure #S-2.8** also demonstrates how the bias stress stability of the TFTs also improved as a result of

successful passivation. Bare devices showed a typical stretched exponential in I_D over time. The passivated devices showed a linear change in I_D that, most importantly, was significantly less in magnitude than their bare versions.

With the issue of passivation addressed, tests were then conducted in liquid using a dual-gate configuration, as shown in **Figure #S-2.9**. From the literature, pH

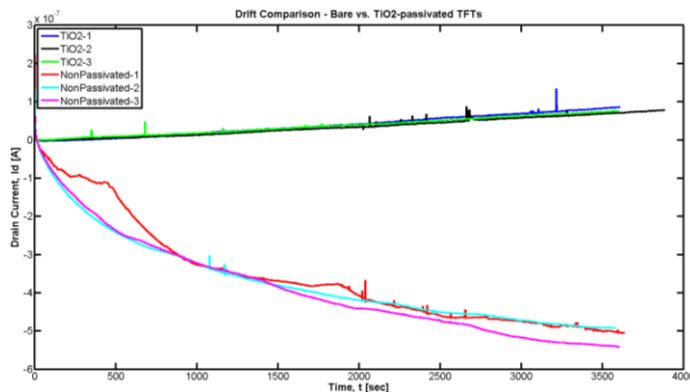


Figure #S-2.8. Bias stress measurement of three TFTs, comparing their performance before and after TiO_2 -passivation.

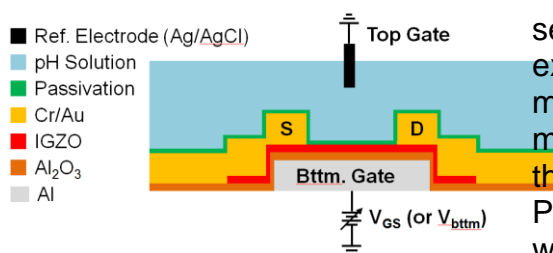


Figure #S-2.9. Cross-sectional view of dual-gate thin film transistor (DG-TFT). The device is biased from the bottom, while the top gate provides a reference potential for the fluid.

sensors using this approach have successfully exceeded the Nernst Limit of sensitivity (59 mV/pH). For our initial tests, the ability to modulate the TFT's I_D by varying the potential at the reference electrode through either DI water or PBS was investigated (**Figure #S-2.10**). The DI water-based tests demonstrate both the stability of the TiO_2 -passivated TFTs in liquid, as well as the possibility of charge-based liquid sensing, a result that was unobtainable previously using bare TFTs. The PBS-based measurement shows slightly increased drift during certain changes in potential but nonetheless follows the expected response. Moreover, I_G remained highly stable

throughout the measurement series.

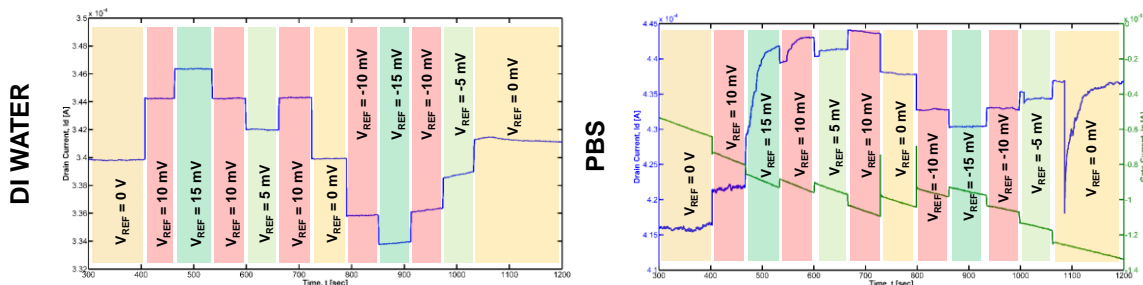


Figure #S-2.10. Transient measurement (I_D vs. time) in either DI water (left) or PBS (right). The device is first biased using the bottom gate (V_{GS}), then I_D is modulated by changing the reference electrode's potential (V_{REF}).

Finally, low-power, low voltage front-end circuitry to operate the TFT sensors has been explored. One of the challenges is the relatively large operating voltage used for the TFTs (see **Figure #S-2.2**). Thus, a measurement circuit using a charge pump to provide V_{GS} and an inductor-based boost converter to provide V_{DS} was designed (**Figure #S-2.11**). In **Figure #S-2.12**, it can be seen that the circuit's measurement of a TFT's IV characteristics compares favorably to measurements obtained with a benchtop

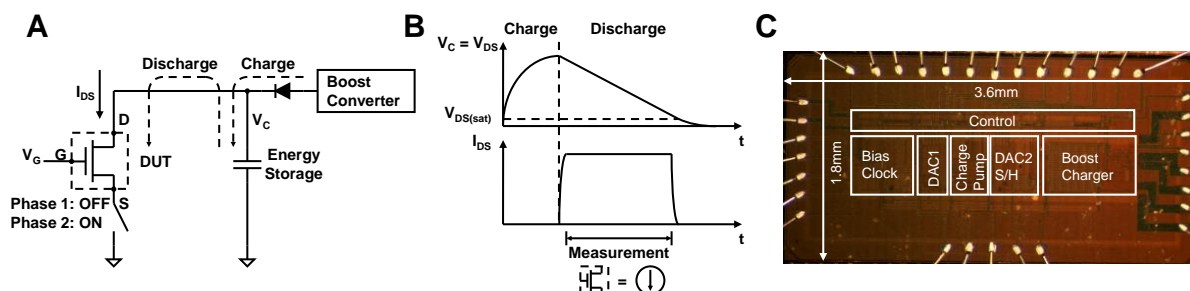


Figure #S-2.11. a) Schematic representation of the TFT measurement interface IC. b) Transient response during a typical measurement cycle. c) Photograph of the fabricated die and its major functional blocks.

system from Keithley. Moreover, the chip inherently operates in a pulse-mode, and is thus compatible with the abovementioned methods for bias stress stability improvement. Most importantly, it consumes very little power ($<2.02 \mu\text{W}$) and is therefore directly suitable for portable, or battery-powered applications.

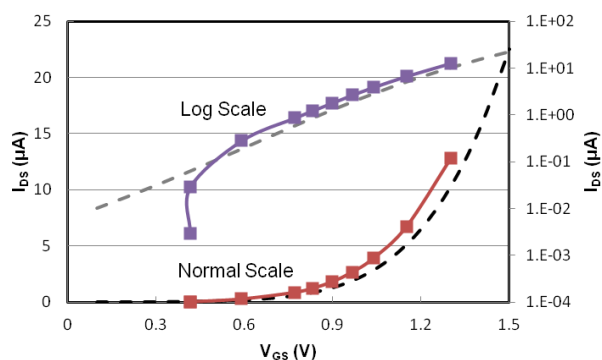


Figure #S-2.12. Measurement of TFT's IV curves obtained by the interface IC (color) compared to measurements by a benchtop Keithley system (dashed).

AFRL/Georgia Tech Interactions:

- Devices were shipped to AFRL (J. Hagen) for further electrical characterization, biofunctionalization and initial liquid-phase sensing.
- In conjunction with J. Hagen at AFRL and I. Papautsky at UC, mounting schemes for the microfluidic structure onto the TFT die were investigated. Testing was also conducted to determine the current design's capability to operate in the liquid phase.
- S. Pavlidis spent 5 weeks at Wright-Patterson Air Force Base working with J. Hagen and his team in 2011. He was responsible for the assembly of electrical characterization test benches and liquid-phase testing. J. Hagen and S. Pavlidis worked closely to learn more about the biofunctionalization process. These activities facilitate the transfer of knowledge between the research groups. Moreover, S. Pavlidis made several trips to UC to collaborate with I. Papautsky's and J. Heikenfeld's students on microfluidic structure mounting, liquid-phase testing, electrical characterization and organic passivation films.

- O. Brand and S. Pavlidis met with J. Hagen, I. Papautsky, X. Wang and J. Heikenfeld at UC in September 2012 to discuss the project strategy going forward.
- AFRL staff visits to GT: Feb. 2, 2013 (N. Kelley Loughnane)
- Regular teleconferences were held between GT and Josh Hagen at AFRL to discuss results and agree on upcoming research objectives.
- Based on the positive results achieved with TiO₂ passivation films on InGaZnO TFTs, Josh Hagen ordered protein receptors specific for TiO₂ binding.

Manpower Development/Transitions (Former BIONIC Students at AFRL):

- None.

Publications:

- S. Pavlidis, J.-J. Su, L. A. Beardslee, P. Leclaire, J. Hagen, N. Kelley-Loughnane, O. Brand, "Pulsed Operation of InGaZnO TFTs for VOC Sensing Applications," in *2012 IEEE Sensors*, Taipei, Taiwan, 2012.
- S. Pavlidis, P. Getz, J. Hagen, N. Kelley-Loughnane, B. Bayraktaroglou, O. Brand, "Investigating Thin film Passivations for IGZO Dual Gate pH Sensors Fabricated at Low Temperature" submitted to the 18th International Conference on Solid-State Sensors, Actuators and Microsystems ("IEEE Transducers") in Anchorage, Alaska, June 2015.
- S. Pavlidis, P. Getz, J. Hagen, N. Kelley-Loughnane, O. Brand, "Impact of Passivation Material and Deposition Temperature on InGaZnO TFT Performance" (*in preparation*)

Presentations:

- S. Pavlidis, "Pulsed Operation of InGaZnO TFTs for VOC Sensing Applications," IEEE Sensors 2012 Conference in Taipei, Taiwan, October, 2012.
- O. Brand, S. Pavlidis, "Pulsed Operation of InGaZnO TFTs for VOC Sensing Applications," Industrial Technology Research Institute (ITRI) in Hsinchu, Taiwan, October, 2012.
- S. Pavlidis, "Pulsed operation of InGaZnO TFTs for VOC sensing applications," at IEN USER Day, Georgia Institute of Technology, Atlanta, GA, USA, April, 2013.